# Local Atomic Effects in the Phase Transition of $TiSe_{2-x}Te_x$ and NaMnBi Semiconductors

Aaron Wegner

Des Moines, Iowa

B.S., University of Oklahoma (2014)

A Dissertation Presented to the Graduate Faculty

of the University of Virginia in Candidacy for the Degree of

Doctor of Philosophy

Department of Physics

University of Virginia

Dec., 2019

# Abstract

Studies of the effects of disorder in semiconducting systems has been central to the search for materials with novel properties. By introducing atomic inhomogeneities through doping or by controlling the growth conditions, the ground state of the system can change significantly even when the average symmetry of the system does not. Intimately connected with this are the local interactions involving the charge, lattice, and spin degrees of freedom that are crucial to understanding the physical properties of materials. Two systems were investigated in this work to explore the effects of the lattice disorder on the properties. One is $TiSe_2$, the other is NaMnBi.

Two exemplary systems have been explored in this thesis: the transition metal dichalcogenides (TMD) and the I-Mn-V semiconductors. The TMDs are a widely studied class of materials. Due to their quasi-two dimensional nature, they offer a window into the physics of low dimensional systems. At the same time, TMDs are promising for use in lightweight, flexible thin film applications. Many TMDs exhibit what is commonly referred to as a charge density wave (CDW) instability in which charge modulations bring about a periodic lattice distortion. The CDW typically occurs in competition with other phases, such as superconductivity. $TiSe_2$ is such a TMD with a $2 \times 2 \times 2$ CDW order that sets in below 200 K. Upon further cooling it becomes superconducting under pressure and with Cu intercallation. Many mechanisms have been proposed to explain the CDW transition that include Fermi surface nesting, exciton condensation, and Jahn-Teller distortions. In this work, we show that a pseudo Jahn-Teller mechanism is most likely responsible for the CDW transition. The intrinsic distortions that arise from the local symmetry breaking due to Jahn-Teller serve as a signature of the charge modulation.

A second system investigated is NaMnBi. This is a semiconductor belonging to the I-Mn-V class of antiferromagnets. The I-Mn-V class is promising for spintronics applications due to their high Néel transition temperatures, their compatibility with existing substrates, and high anisotropy that could lead to spin-orbit torque, crucial

to spintronic devices. Moreover, NaMnBi exhibits extreme magnetoresistance never observed before in this class. Such a property can be of tremendous importance in GMR devices. Therefore, this work has opened up a venue where the physics of antiferromagnetic semiconductors can be explored.

Key to this work are the effects from the lattice distortions on phase transitions in these two classes of materials. Neutron scattering has been used to study the magnetic and atomic structures. In the case of $TiSe_2$, doping with Te s in $TiSe_{2-x}Te_x$ leads to suppression of the CDW transition between x = 0.2 and 0.25. The local distortions in the CDW phase are found to be inconsistent with the existing models, and a local model with breathing distortions that significantly shorten a fraction of the Ti-Se nearest neighbor bonds is found. This indicates that a pseudo Jahn-Teller effect that lowers the Se p bands can explain the CDW formation. In NaMnBi, with a Néel temperature of 340 K, a positive magnetoresistance of up to 10000% at 2 K and 9 T when vacancies are introduced to the lattice, the highest reported for this class of material. In addition to the high magnetoresistance, a structural phase transition is observed leading to a superlattice with a polaron formation and a change in the coordination geometry of the Mn atoms. The temperature of the superlattice transition is suppressed upon reducing the Bi vacancy content. The structural phase transition leads to a broken inversion symmetry, which is useful for spin transfer torques. The large magnetoresistance and broken inversion symmetry make NaMnBi a promising candidate material for spintronic applications.

# Acknowledgments

Throughout my studies I have received invaluable support from my mentors, colleagues, family and friends. I would like to thank my research advisor, Prof. Despina Louca, whose guidance and vision transformed me from a student to a scientist as I transitioned from the classroom to the laboratory. I would also like to thank the other members of my research committee, Prof. Marija Vucelja, Prof. Utpal Chatterjee, and Prof. Keivan Esfarjani.

The neutron scattering experiments in this work would not have been possible without the help and guidance of the instrument scientists and support staff at the neutron facilities. This includes Dr. Craig Brown at the NIST Center for Neutron Research, Dr. Jeorg Neuefeind, Dr. Matt Tucker, Dr. Christina Hoffman, Dr. Michelle Everett, and Helen He at the Spallation Neutron Source at Oak Ridge National Laboratory (ORNL), and Dr. Clarina Dela Cruz, Dr. Keith Taddei, and Malcolm Cochran at the High Flux Isotope Reactor at ORNL.

I would like to acknowledge my labmates. Dr. Junjie Yang taught me everything I know about sample synthesis, and Dr. John Schneeloch, Dr. Chunruo Duan, Dr. Anushika Athauda, Yu Tao, Sharon Phillip, Zhengyang Xu, Martine Lokken, and Ian Nakayama have made my time in the lab enjoyable with their suggestions and company.

I would like to thank my friends who have made stressful and busy times more bearable: Sina Tafti, Zack Carson, Ben Godek, Sanjay Khatri, Rajveer Nehra, Gen Schmitt, and Kacey Price.

I would like to thank my parents, Mike and Sandy Wegner, for their support throughout my life. Their love and support has enabled me to pursue my dreams.

Finally, I would like to thank my wife, Allie Kallmann Wegner. She has been the best supporter and confidant I could have asked for and I look forward to all of the adventures our life together will bring.

# Contents

# List of Figures

# List of Tables

# Chapter 1

# Introduction

Layered materials are excellent candidates for new technological applications. Due to the weak interlayer bonding, layered materials are often easily cleaved or exfoliated and can be machined into useful geometries and heterostructures. The weak bonding between layers also leads to the opportunity to study lower dimensional physics. In the years since graphene was first isolated with scotch tape, interest in lower dimensional materials has been reignited, as atomically thin materials can be used for flexible, lightweight applications.

Among the phenomena that is commonly observed in lower dimensional materials is a charge density wave instability (CDW). CDW occurs when charges form a standing wave pattern in a material that leads to a periodic lattice distortion. The simplest explanation for the CDW is Fermi surface nesting. While Fermi surface nesting satisfactorily explains the distortion in one dimensional chains, electron-phonon coupling is necessary to explain the transition. CDWs are notable because the are often found in competition with other phases such as superconductivity. Examples of systems with coexisting and competeing CDW and superconductivity include the transition metal dichalcogenides, transition metal trichalcogenides such as $NbSe_3$[1], cuprates such as $YBa_2Cu_3O_{6+\delta}$[2] and $Bi_2Sr_2CaCu_2O_{8+\delta}$[3], and the $BiS_2$ superconductors such as $LaO_{1\text{-}x}Fe_xBiS_2$[4]. While all these materials are low dimensional materials with a superconducting phase, the origin of the CDW is different. Electron-phonon coupling is crucial to explaining the CDW instabilities, but the mechanism is different system

to system[5].

The most studied class of two-dimensional materials is the transition metal dichalcogenides (TMDs.) TMDs are a diverse class of materials that exhibit a wide variety of physical phenomena. The materials have chemical formula $MX_2$ where M is a transition metal and X is a chalcogen from group VI of the periodic table. TMDs most commonly crystallize into a hexagonal structure. TMDs are made up of X-M-X structures that stack to form monolayers. Intralayer bonds between chalcogens are much weaker than bond between atoms within the same layer. As can be seen in Fig. 1-1, the distance between chalcogen atoms in adjacent layers is greater than the closely bound $MX_6$ clusters of one transition metal bonded to six chalcogens in either an octahedral or trigonal prismatic geometry. The crystals can be easily cleaved, and tend to grow in small platelike forms. The small plates easily slide past each other, and the first uses for TMDs took advantage of this mechanical property. $MoTe_2$, as well as the other Mo and W TMDs were used as solid state lubricants in high vacuum applications since the 1940s[6]. TMDs host a wide variety of electronic phenomena and phase transitions. The class includes semiconductors like the Mo[7, 8], W[9], Sn[10], Hf[11], Zr[12], and some of the Ti compounds[13], semimetals such as $TaS_2$[14], half-metals[15] such as $CoS_2$, metallic materials, and superconductors[16] such as $MoS_2$. For example, monolayer $MoS_2$ has a field effect carrier mobility significantly lower than graphene, and can be used as a monolayer field effect transistor (FET)[17]. Other recent TMD developments include the discovery of nonsaturating magnetoresistance in $WTe_2$[18]. With the rich physics found in TMDs, proposed applications include a wide range of devices including solar cells[19], LEDs[20], fuel cells[21], photocatalysts[22], and sensors[23]. The property that will be focused on in this thesis is the charge denisty wave (CDW) transition of $TiSe_2$. Due to the low dimensional nature of TMDS, it should come as no surprise that CDW transitions occur in several TMD systems. The $4d^1$ and $5d^1$ TMDs containing Ta, Nb, and Ti form CDWs coexisting with superconductor phases.

This thesis focuses on one TMD that has received extensive attention yet remains controversial. Understanding the CDW phase that coexists with superconductivity

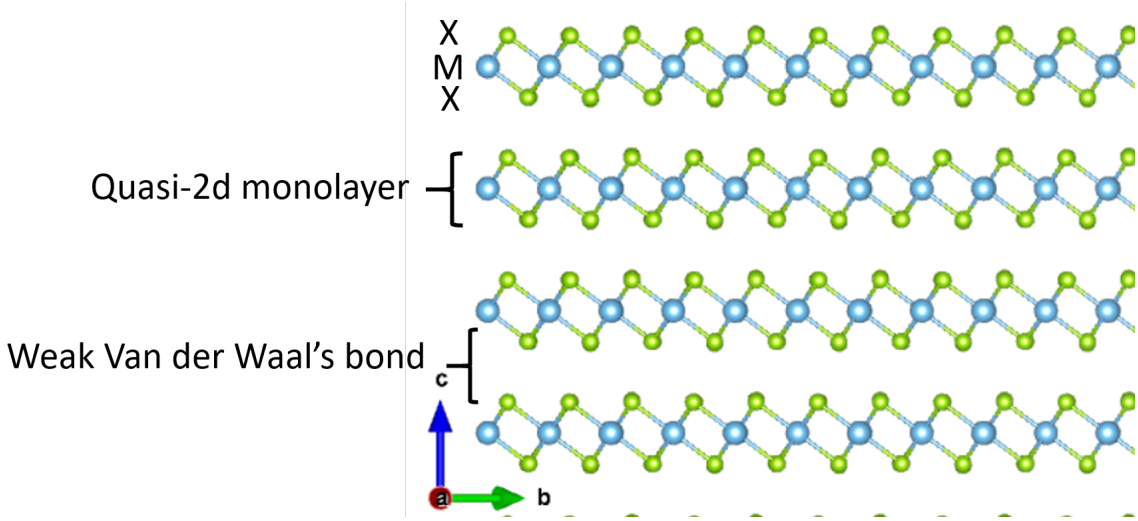


**Figure 1-1:** TMDs crystallize into layers that are weakly held together by Van der Waal's interactions.

can advance understanding of the relationship between the competing phases. Superconductivity in $TiSe_2$ was first seen in Cu intercalated $TiSe_2$. With Cu intercalated, a superconducting dome appears with the suppression of the CDW state. The dome is centered about a concentration of 0.08 Cu with transition temperature of 4K[24]. Cu saturates in $TiSe_2$ with a concentration of around 0.1. In addition to Cu intercalation, high pressure can induce superconductivity in $TiSe_2$. The superconducting dome occurs from 2 to 4 GPa with a maximum $T_C$ of around 2 K[25]. There are multiple proposed mechanisms behind the CDW in $TiSe_2$. These range from an excitonic insulator transition to a purely structural Jahn-Teller-like transition. Theoretical calculations indicate that the mechanism behind the CDW phase is highly dependent on the local interactions between atoms. These interactions can be studied by looking at the local structure, and in this thesis, isovalent doping was used to look at how the local environment changes and how it influences the CDW order.

Spintronic devices leverage the spin degree of freedom to store or transmit information in addition to the charge degree of freedom that store information in conventional electronics. To date, all commercially available spintronic devices are made using ferromagnetic (FM) heterostructures. An important property that is used in spintronic devices is magnetoresistance (MR.) Spintronics devices take advantage of

different scattering of majority spins compared to minority spins in a ferromagnetic material using giant magnetoresistance (GMR). This allows a layered device in which two FM layers are aligned with each other and separated by a nonmagnetic layer to have a lower resistance than when they are antialigned. As the material can have a high resistance state and a low resistance state, these states can be used as bits in a magnetic random access memory device (MRAM.)

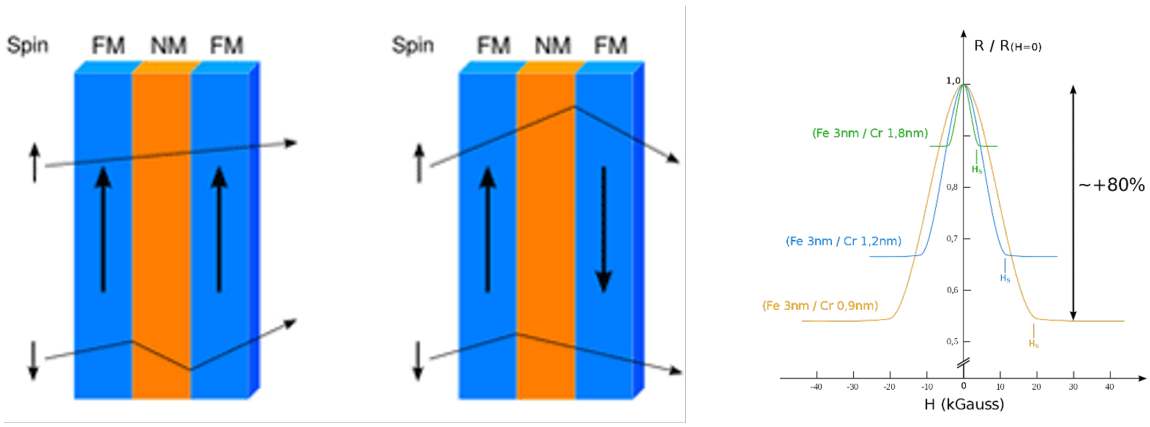


**Figure 1-2:** The two spin states of an unpinned GMR device are shown on the left. With no magnetic field, the FM layers have opposite spins and high resistance. When a magnetic field is applied, the layers align and resistivity decreases[26].

The I-Mn-V class of antiferromagnetic (AFM) semiconductors is a promising class of materials. Materials in this class have a high Néel temperature. They can also be easily exfoliated. Members of the class have been demonstrated to have interesting and useful properties. For example, LiMnAs has been epitaxially grown on existing substrates, which is useful for compatibility with technology and CuMnAs has been demonstrated to be able to control spin through spin orbit torque in order to make a simple AFM memory device. A material of this class that has not been thoroughly studied is NaMnBi. In this thesis, NaMnBi is studied and an extreme magnetoresistance (MR) that is much higher than any other in the class is reported. This MR is only observed when vacancies are introduced to the system and depends strongly on the structure.

As AFMs have no external magnetic field and control of their magnetic moment is difficult, it was initially believed that there were no practical uses for AFM ma-

terials. There are several different types of three dimensional AFM, depending on the direction of the magnetic moments and the direction of the propagation vector. For an A-type AFM, the spins in the plane perpendicular to the moment are all the same, and the AFM is interlayer. For C-type AFM, adjacent moments in a given plane point in opposite directions but the out of plane interactions are ferromagnetic. In a G-type AFM, both the in-plane and interlayer interactions are AFM. Fig. 1-3 shows the different types of AFM along with FM spin orientation.

Spintronics are promising new technologies for replacing electronic devices because when spins store information instead of charge, less energy is wasted moving charges around in a spintronic device. Additionally, charge leaks away from capacitors used to store electronic bits, so electronic devices need a power source to avoid degradation. Spintronics also promise faster switching and are less likely to be perturbed by an external magnetic field, or a cosmic ray in the case of space-based applications. Specific applications that can easily benefit from spintronics are machines with short periods of activity divided by long periods of latency and sensors that must perform in extreme environments, such as in space or under the hood of a high performance vehicle[27].

AFMs are good candidates to replace FM heterostructures in spintronic devices. First and foremost, the intrinsic field of a FM device can interfere with nearby components, which means the FM-based device requires more space on the chip, whereas AFM materials are invisible to nearby components. Besides improvements in miniaturization, ultrafast dynamics in AFM materials leads to switching that can exceed the speed of FM devices. Materials research into AFMs that are compatible with existing technologies and have properties conducive to spintronics applications is crucial for developing the next generation of devices. AFM spintronics can be written at THz frequencies and read using anisotropic magnetoresistance[28].

Both $TiSe_2$ and NaMnBi host interesting physical phenomena which depend strongly on the local structure and lattice defects. In this thesis, neutron scattering is used to study the changes in the structure when Te (in $TiSe_2$) or vacancies (in NaMnBi) are introduced to the system. In $TiSe_{2\text{-}x}Te_x$, it is found that a pseudo-Jahn Teller

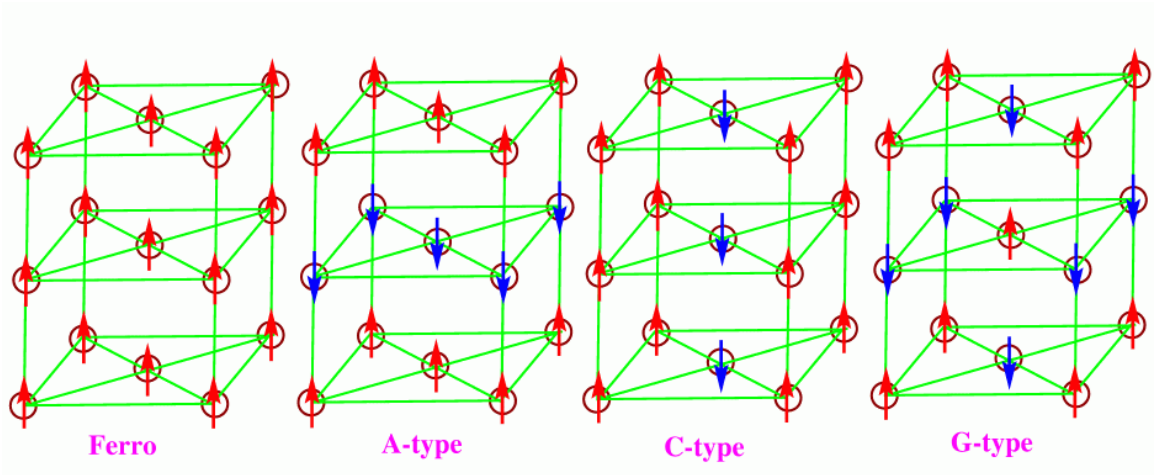


**Figure 1-3:** The spin orientation of FM, and A, C and G-type AFM[29].

mechanism controls the CDW order while in NaMnBi vacancy ordering occurs that changes the coordination environment of Mn in the sample with high MR.

### 1.0.1 Layout of the Dissertation

The following chapters are organized as follows. In Chapter 2, the background of the physical properties studied, such as CDW, MR, and AFM are discussed. Chapter 3 will be a brief review of the TMDs and their structures. Chapter 4 will discuss the AFM semiconductors and AFM spintronics. Chapter 5 details the experimental methods used in this study. Chapter 6 discusses the neutron scattering study on $TiSe_{2-x}Te_x$ and the implications on the CDW mechanism. Chapter 7 discusses the characterization and neutron scattering studies of NaMnBi. Chapter 8 is a brief conclusion summarizing the finding in this thesis.

# Chapter 2

# Background

## 2.1 Charge Density Waves

A CDW is a phenomenon in which the electrons in a crystal form a standing wave pattern that is typically accompanied by a periodic lattice distortion of the atoms in the crystal. CDWs are common in lower dimensional materials, such as transition metal dichalcogenides (TMDs). The simplest CDW is called a Peierls distortion, and occurs in the one dimensional metal chain at half filling.

### 2.1.1 One Dimensional Chain

The simplest version of a CDW was described theoretically by Peierls in a one dimensional chain of atoms, each separated by a distance $a$ [30]. The chain is considered to be metallic, therefore the electrons are noninteracting and experience a periodic potential V(x+a) = V(x) and a single particle Hamiltonian can be considered. The Hamiltonian for this chain is:

$$H = \frac{p^2}{2m} + V(x) \tag{2.1}$$

Solving the Schroedinger equation for the system gives a quadratic dispersion. The correction to this dispersion using a periodic potential can be done using the Kronig-

Penney model [31]. in which we take the periodic lattice potential to be:

$$V(x) = \sum_n U_0 a \delta(x + na) \tag{2.2}$$

In order to solve the energy dispersion as a function of momentum, the potential must be written as V(q), the sum of the Fourier components of V(x):

$$E(q)\psi(x) = [-\frac{h^2}{2m}\frac{\partial}{\partial x} + V(q)]\psi(x) = [E^0 + \frac{U_0}{a}\int_{-\frac{a}{2}}^{\frac{a}{2}} dx \sum_{n=-\infty}^{\infty} \delta(x+na)e^{-ikx}]\psi(x) \tag{2.3}$$

$$E(q)\psi(x) = [-\frac{h^2}{2m}\frac{\partial}{\partial x} + \frac{U_0}{a}]\psi(x) \tag{2.4}$$

In order to solve Schroedinger's equation, the wavefunction must be written in terms of Fourier components.

$$\psi(x) = \sum_K u(q)e^{-i(q+K)x} \tag{2.5}$$

$$E(q)\sum_K u(K)e^{-i(q+K)x} = \left(\frac{h^2(q+K)^2}{2m} + \frac{U_0}{a}\right)\sum_K u(q)e^{-i(q+K)x} \tag{2.6}$$

$$[E(q) - \frac{h^2(q+K)^2}{2m}]u(K) = \frac{U_0}{a}u(0) \tag{2.7}$$

By solving to eliminate u(K) and u(0), the result is:

$$\sum_K \frac{\frac{2mU_0}{h^2 a}}{\frac{2mE(q)}{h^2} - (q+K)^2} = 1 \tag{2.8}$$

This is impossible to solve analytically, but an iterative solution shows that at low q the solution is identical to the first order solution and the dispersion is quadratic. Close to the edge of the Brillouin zone a gap opens and the band flattens, as seen in Fig. 2-2. The energy states that are occupied are lowered in energy, while the unoccupied states above the Fermi surface are raised in energy. As only occupied states

matter when considering the total energy of the system, the distortion is energetically favorable.

### Peierls Distortion

Consider a periodic lattice distortion that changes the periodicity of the metal chain such that now $V(x) = V(x+2a)$. This periodicity is chosen because by doubling the lattice the Fermi surface is now located at the zone edge. In this case, the reciprocal lattice vectors also change, and the Brillouin zone (BZ) is halved in size. Following the calculations from above, this periodic lattice distortion also leads to a gap opening, now at $k = \frac{\pi}{2a}$. This gap is different from an ordinary gap because thermal fluctuations with energy larger than the gap destroy the gap and prevent a distortion from occuring. Would this distortion be energetically favorable? If the gap opens at the Fermi level, the answer is yes, provided the energy gained is more than the cost to deform the lattice. Fig. 2-1 shows the distortion that occurs in a 1D chain of atoms. Fig. 2-2 shows the change in the dispersion when the gap opens.

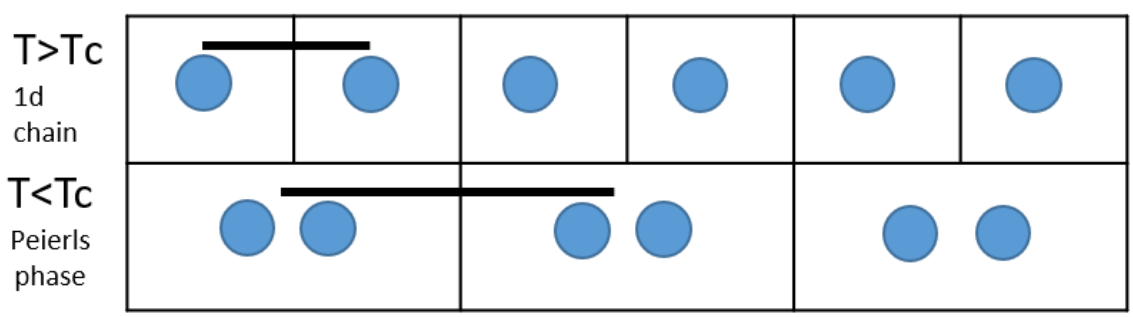


**Figure 2-1:** The 1d chain of atoms at half filling is shown above the Peierls transition and below. The unit cell doubles as the atomic position is modulated in a wave distortion.

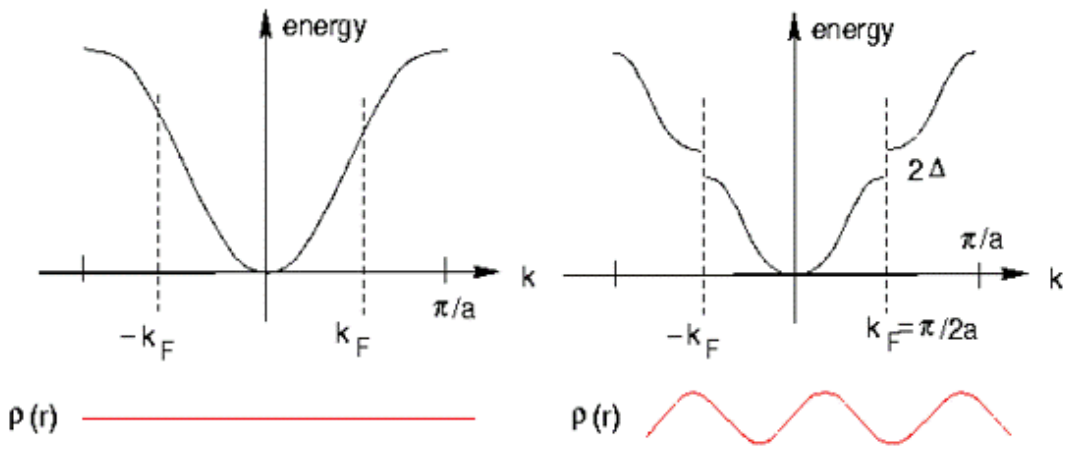


**Figure 2-2:** The band structure of the first BZ is shown above the transition temperature on the left and below the transition temperature on the right. The band gap opens at the Fermi momentum.

### 2.1.2 2D Peierls Distortions

In higher dimensions, the Peierls distortion becomes more complicated[32]. In 1D, there are only two states on the Fermi surface which can be easily connected by a line, the wave vector. In two dimensions, the Fermi surface that satisfies this condition is a constant energy line, and in three dimensions it is a constant energy surface. Generally speaking, it becomes challenging to find a line that maps a part of the surface onto another and sufficiently lowers the energy to overcome the lattice energy. In order for Fermi surface nesting to occur, there must be large parallel lines in the Fermi surface. When this occurs, a single nesting vector can connect the lines of the Fermi surface, leading to a CDW. Fig. 2-3 shows the simplest model for Fermi surface nesting, a square lattice with a square Fermi surface. In this model, the Q-vector is $(\frac{\pi}{2}, \frac{\pi}{2})$ and allows the band folding to occur. While Fermi surface nesting can occur in 1D, most 2D materials do not have a simple Fermi surface, and the nesting vectors can be more hidden and there can be multiple Q-vectors. When CDW materials do not have Fermi surfaces conducive to Fermi surface nesting then other explanations are needed to describe the transition.

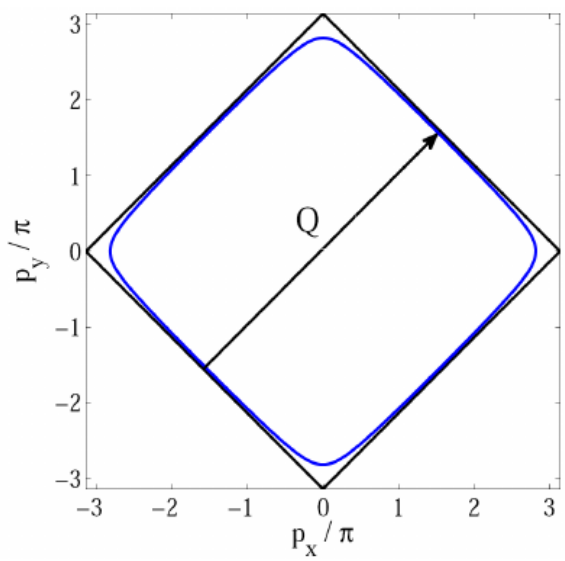


**Figure 2-3:** The band structure of the first BZ for a theoretical system that leads to Fermi surface nesting is shown above the transition temperature on the left and below the transition temperature on the right. The band gap opens at the Fermi momentum.

## 2.2 Magnetoresistance

### 2.2.1 Giant Magnetoresistance

For electrons moving in a material with no magnetic field, the carrier mobility $\mu$ is defined as the quotient of the electric field and velocity.

$$\vec{v} = \mu\vec{E} \tag{2.9}$$

Applying a magnetic field to most materials changes the resistance slightly due to the Lorentz force. With the application of the magnetic field, the velocity becomes proportional to the Lorentz force, which depends on the velocity of the electron.

$$\vec{v} = \mu(\vec{E} + \vec{v}x\vec{B}) \tag{2.10}$$

$\vec{v}$ can be isolated to give a velocity proportional to $1+(\mu\mathrm{B})^2$. For most materials this leads to a resistance that decreases by around 5% in a magnetic field, although semiconductors with high mobility can change by orders of magnitude. This is due to electrons becoming slower in the transport direction in the applied field field as

the field causes the electrons to turn, leading to a lower electric current.

Not all materials have magnetoresistive behavior that is based on simple Lorentz force calculations. Giant Magnetoresistance (GMR), discovered independently by Fert[26] and Grünberg[33], occurs in layered ferromagnetic heterostructures. To observe GMR, two ferromagnetic layers are separated by a thin nonmagnetic material. The thickness of the spacer layer is set such that the two FM layers have an AFM interaction in the ground state[33]. When a magnetic field is applied, the FM layers align in the same direction. The direction of the magnetic moment of a FM can easily be controlled by applying an external magnetic field, but the direction of the field can also be pinned by an AFM layer. GMR was first demonstrated in Fe/Cr layers. GMR is based on the fact that electrons with spin antialigned with the magnetic moments of a ferromagnet scatter more strongly than electrons aligned with the magnetic field, leading to a higher resistance for those electrons. The most common GMR heterostructures in use are created by pinning a FM so that its magnetization will not reorient in an applied field. A nonmagnetic spacer layer is added on top of the pinned FM layer to tune the interaction between the FM layers, and the unpinned FM is deposited on top of the spacer. When a voltage is applied across the layers, separate conduction channels occur for spin up and spin down electrons. When a magnetic field is applied, the FM layers become aligned and one channel has a much lower resistance than the other. As these channels are in parallel, the total resistance of the devices decreases.

These MR properties can be tuned by changing the details of the sample, such as the materials used and the thickness of the layers. The resistance as a function of field for Fe/Cr layers with different thincknesses and number of bilayers is shown in Fig. 2-4. There are two common geometries used in GMR devices. These are the current in plane (CIP) and current perpendicular to plane (CPP) geometries. In the CIP geometry, both electrodes are attached to the same side of the device and current flows along the layers. In the CPP geometry the electrodes are placed on opposite sides of the superlattice and current flows through the layers. MR is largest in the CPP geometry but CIP is easier to fabricate for device applications.

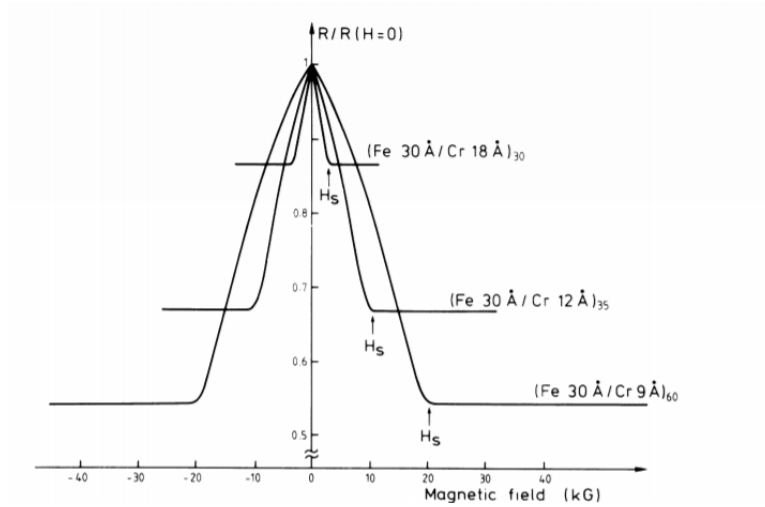


**Figure 2-4:** Magnetoresistance of three Fe/Cr superlattices at 4.2 K[26]

## 2.3 Tunnel Magnetoresistance

Tunnel magnetoresistance (TMR) occurs in heterostructures that are very similar to the GMR heterostructures. The difference between the two is that instead of metallic, the nonmagnetic layer between the FM layers is insulating. Devices exhibiting TMR are known as magnetic tunnel junctions (MTJ). Because of the insulating layer, the MTJ has a larger overall resistance than the GMR devices. Classically, the MTJ should have a resistance greater than that of the insulating layer. If the layer is thin enough, electrons can tunnel from one FM layer to the other. As such, this is a purely quantum mechanical phenomenon. The explanation for TMR is similar to that of GMR. In tunneling, the spin of the electron is conserved. Because FM have spin-dependent densities of state, the rate of tunneling depends on the spin. When the FM layers have parallel spins, the conductance is significantly higher. When first observed in Fe/Ge-O/Co junctions[34], the change in MR was only 14%. Now, MTJ can be easily made with Fe FM layers and a MgO tunnel layer that reach MR of 200% at room temperature[35], and a maximum TMR of 604% at room temperature has been observed in CoFeB/MgO/CoFeB junctions[36]. As this is higher than the MR accessible with GMR, MTJs have gained more use in devices that rely on MR such as MRAM.

## 2.4 Colossal Magnetoresistance

The disadvantage of GMR is that it is not a single phase and each layer must be deposited carefully using molecular beam epitaxy (MBE). Single phase, homogeneous materials have advantages over the superlattice heterogeneous materials, as they are easier to synthesize. Transition metal oxides, such as the manganites, are a single phase material that can exhibit a large MR at room temperature, depending on the composition. The phenomena observed in these materials is called colossal magnetoresistance (CMR) to differentiate it from GMR.

The CMR materials have a chemical composition of $Ln_{1\text{-}x}B_xMnO_3$, where Ln is a lanthanide, commonly La, and B is an alkaline earth metal[37]. $LaMnO_3$ and $CaMnO_3$ are both AFM perovskites. When x is between 0.2 and 0.4 in $La_{1\text{-}x}Ca_xMnO_3$, the ground state becomes FM[38]. In the doped samples, the resistivity drops sharply at the paramagnetic to FM transition. La is trivalent, while the alkaline earth metals are divalent. In replacing the La in the system, holes are doped into the material and the Mn ions can be 3+ or 4+.

In mixed valence materials the double exchange interaction is used to characterize the transport. The double exchange interaction occurs when atoms of different oxidation states exchange electrons through a different atom that both are bonded to. The consequence of the double exchange interaction is it is easier for an electron to move through a material if it does not have to change the direction of its spin. When the divalent atoms are doped into the system and create $Mn^{4+}$ ions, there is an opening in the Mn $e_g$ band for electrons to hop to. The hopping of electrons in the doped materials is suggested as the reason for the insulator to metal transition in the perovskites. The double exchange interaction, however, is not strong enough to satisfactorily describe the observed transport[39], and electron phonon interactions are necessary to understand the transport behavior.

### 2.4.1 FM Spintronic Devices

The simplest spintronic devices that can be made using GMR is a spin-valve. The spin valve is simply made with a pinned ferromagnet and unpinned ferromagnet separated by a nonmagnetic material, as described above. When spins are aligned, the resistance is much lower than when they are antialigned and the current is spin-polarized. Spin valves are the basic building blocks for spintronics made using GMR. Spin valves are used as magnetic sensors for disk read heads. These sensors read information that is stored as a magnetic bit. As the spin valve passes closely over a bit, the small magnetic field is enough to change the orientation of the unpinned FM. A voltage is applied and the change in resistance allows the bit to be read[40].

Many additional spintronic devices have been proposed. Some of these have been created, while others await material advances and design advances. The Spin Field Effect Transistor (SpinFET) is a device proposed by Datta and Das[41] that can improve on classical transistors because they theoretically do not require amplifiers or electric currents to detect the signal. This allows for smaller, more energy efficient devices to be built. In a SpinFET, a semiconductor layer is sandwiched by two FM layers, the drain and the analyzer. The schematic for the Datta-Das transistor is shown in Fig. 2-5. Like the spin valve, the transistor takes advantage of the half-metallicity of the ferromagnets. The current travelling through the semiconductor is spin polarized when it leaves the drain. While moving through the semiconductor, the spin precesses, and the resistivity depends on how well the precessed spin aligns with spins of the analyzer. The precession of the spin relies on spin-orbit coupling in the semiconductor. The spin-orbit coupling is strong in materials with broken inversion symmetry. For heterostructures in which inversion symmetry is broken, the Rashba effect dominates the spin orbit interaction. The Rashba effect[42] takes advantage of the field that naturally occurs at the interface of the ferromagnet and the semiconductor and can be tuned by applying a gate voltage. The Rashba effect is strongest in small gap semiconductors, such as InAs and GaAs. For materials in which inversion symmetry is not broken, such as zincblende semiconductors, the

Dresselhaus effect allows the spins to be manipulated without the aid of a magnetic field[43]. A working spin transistor has not yet been realized.

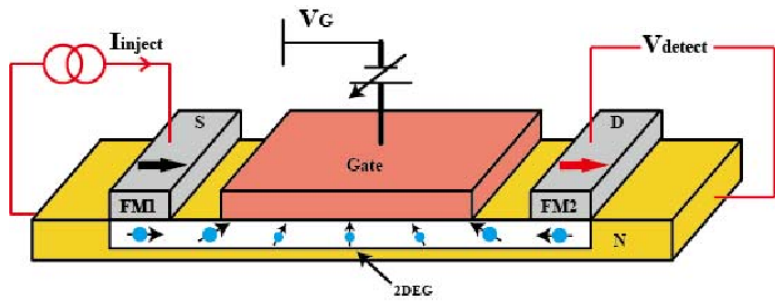


**Figure 2-5:** Schematic for a Datta-Das Spin transistor[44].

The most useful FM spintronic device available commercially is magnetic random access memory (MRAM). A working RAM needs three components. It must be able to store information for long periods of time, there must be a way to read the information without changing the state, and there must be a way to write information to the drive. There are two industry standards for RAM, which are dynamic and static random access memory (DRAM and SRAM). In DRAM, the information is stored in capacitors that are either charged or uncharged. The charged capacitor has a state 1, while no charge is a 0 bit[45]. The advantage of DRAM is the scalability, as capacitors in integrated circuits can be made very small and only one capacitor and one transistor is needed per bit. DRAM is used for applications in which a large amount of memory is required, such as graphics applications. The downside of DRAM is charge leakage from the capacitor. Because of this leakage, a constant power source, the memory refresh circuit, is necessary to keep the information and the power consumption is greater in DRAM. SRAM, while still a volatile memory source that needs a power supply, is much less volatile than DRAM. SRAM is made up of four or more transistors, with two stable states to serve as bits[46]. SRAM is faster than DRAM, but the space required for the bits makes it much more expensive. SRAM is typically used for the CPU cache.

MRAM seeks to replace DRAM and SRAM as a universal memory. It can accomplish this by being faster, more efficient, and less volatile than DRAM and smaller

than SRAM. The first MRAM devices used spin valves as the bit for information storage. The GMR spin valves have a small read signal and have since been replaced by magnetic tunnel junctions (MTJ). A MTJ is similar to a GMR spin valve, except the metallic space layer is replaced by an insulator and has a high MRcitedurlam2000nonvolatile. The reason a high MR is necessary for a spintronic device is that in order to reliably read a magnetic bit the voltage difference between 0 and 1 must be at least 0.2 V.In GMR devices, the highest practical MR at room temperature is only about 10-20%, while the MTJ can reach up to 200%, which is sufficient to reliably read[47]. The first MRAM was written using the application of magnetic field through an applied current. The field needed to switch the direction of the free layer of the FM is inversely proportional to the area of the layer. This is prohibitive when trying to increase the density of RAM, as the fields quickly become too large to be practical. This is improved by using spin transfer torque (STT) for switching. With STT switching, a current is passed from the pinned layer to the free layer. As only the majority electrons are able to pass through to the free layer, the spin polarized current applies a torque that aligns the magnetic field with the pinned layer. In order to switch back, a current is applied in the opposite direction. Recently, spin-orbit torque (SOT) has been studies as a potential method of writing MRAM. SOT has potential for a faster write time and smaller write current, but the physics behind the mechanism are still a topic of research[47].

# Chapter 3

# Transition Metal Dichalcogenides

## 3.1 Two dimensional semiconductors

Advances in thin film materials such as graphene have led to a boom in the study of lower dimensional materials. The research in these materials is driven by the need for further miniaturization of semiconductor devices, which can be achieved by using thin films. While graphene, perhaps the most famous of the two dimensional materials, has many interesting and useful properties, the lack of a bandgap makes it unsuitable for most electronic applications[48].

Boron nitride (BN) is another two-dimensional material that has been studied. The crystal structure of BN is very similar to graphene, with a honeycomb lattice with a two atom basis that can be exfoliated from the bulk. Unlike graphene, the two atoms in the unit cell are of different species. These differences break inversion symmetry and open a gap in the band structure. With a bandgap of 5.9 eV, BN can be used as an insulating filler in electronics applications[49].

Many bulk materials with layered structures are made up of individual layers that are bound by weak Van der Waal interactions. Van der Waal materials are easily exfoliated and exhibit two-dimensional physics. It is easy to see from the above examples that a rich variety of physics becomes accessible in Van der Waal materials. The most studied of these materials is the transition metal dichalcogenides. In this class of materials there are over forty structures that qualify as hexagonal Van der

Waal layered materials[50]. These materials host a wide array of physical phenomena that have promising technological applications. This chapter will give a review of the physics of TMDs in order to place our study of $TiSe_{2-x}Te_x$ in proper context.

## 3.2 Introduction to Transition Metal Dichalcogenides (TMDs)

Transition metal dichalcogenides are a diverse class of materials that exhibit rich physics. The materials have chemical formula $MX_2$ where M is Ti, V, Cr, Zr, Nb, Mo, Tc, Pd, Hf, Ta, W, Re, or Pt and X is S, Se or Te[51].

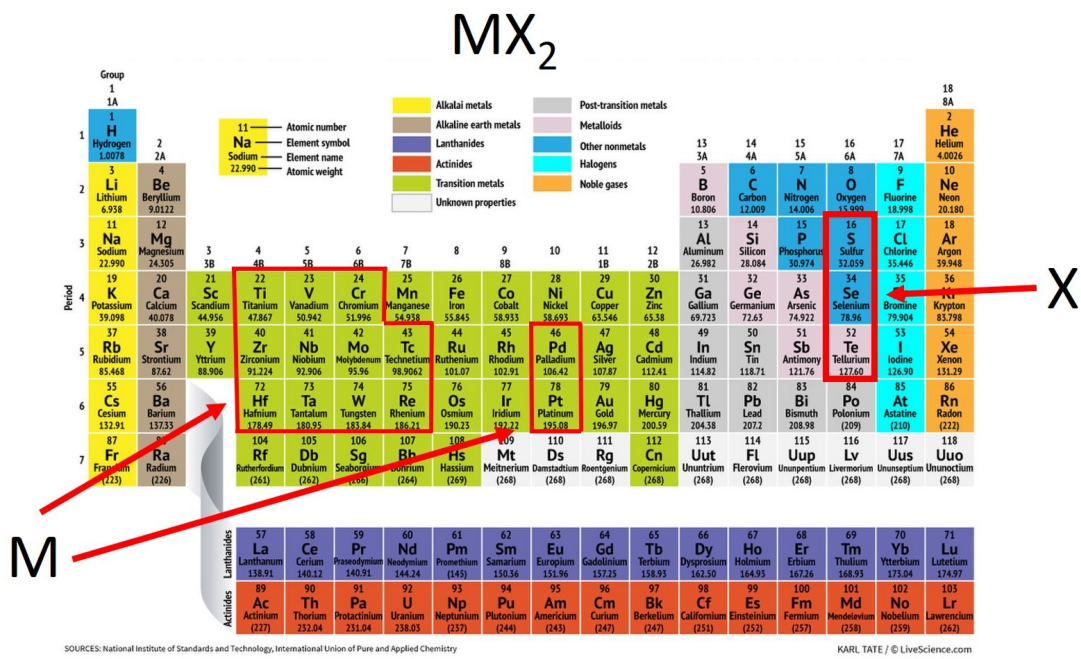


**Figure 3-1:** Red boxes in the periodic table of elements[52] show which elements make up the TMD class of materials.

TMDs most commonly crystallize into a layered structure which has many polytypes. Polytypism refers to a phenomenon where a chemical compound can form multiple different unit cells. The monolayers of TMD compounds crystallize in hexagonal

lattices. The different polytypes differ in whether the transition metal is surrounded by the chalcogen ligand in an octahedral or trigonal prismatic coordination and by the number of layers that must be stacked before the pattern repeats. A monolayer is made up of a X-T-X sandwich and with a thickness of around 6-7 Å, depending on the material. An individual monolayer can have two different point group symmetries, octahedral ($D_{3d}$) or trigonal prismatic ($D_{3h}$) The most common polytypes are 1T, 2H, and 3R. 1T materials are octahedrally coordinated, and there is no displacement between layers. 2H has trigonal prismatic coordination, and the orientation of odd layers differs from that of even layers, requiring two monolayers before repeating the unit. 3R is also trigonal prismatic, but requires three layers for a repeating unit. Fig. 3-2 shows the unit cell of these three phases such that the layers are visible and looking down in the direction perpendicular to the layers.

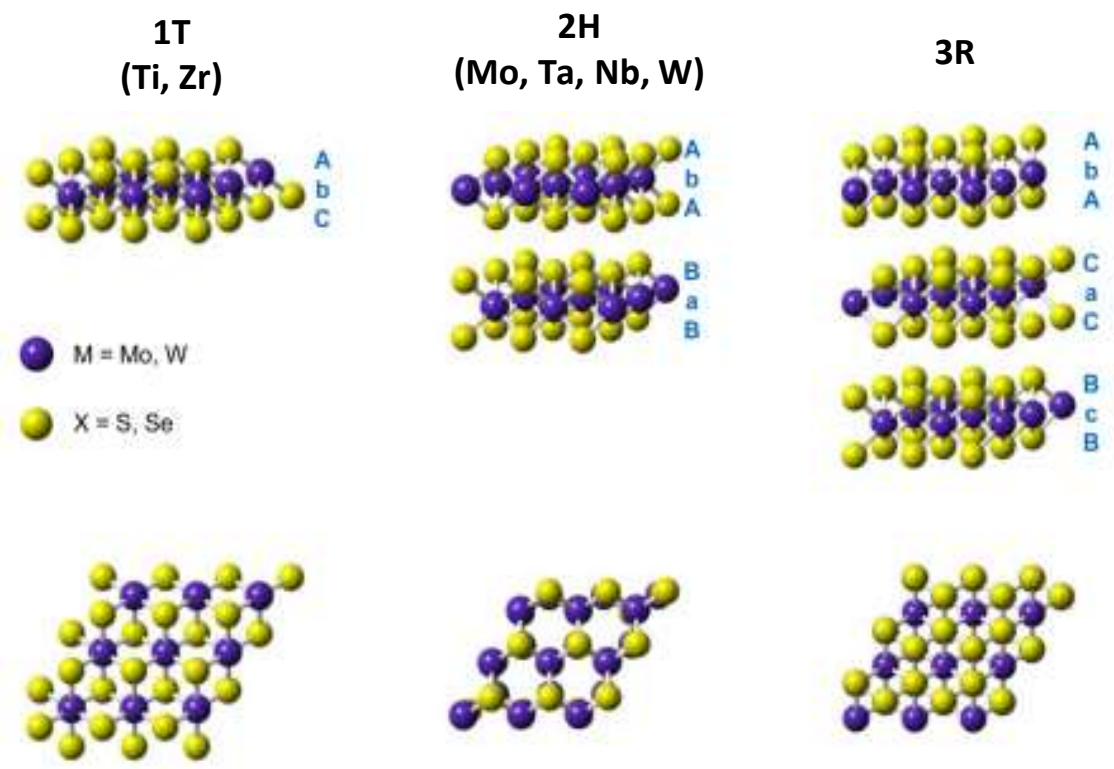


**Figure 3-2:** The most common polytypes of TMDs are the octahedral 1T, and trigonal prismatic 2H and 3R phases.

Intralayer bonds between chalcogens are much weaker than bond between atoms of the same layer. The chalcogen and transition metals are covalently bonded, with a

bond length on the order of 3 Å. The transition metal is in a 4+ oxidation state, while the chalcogen is in a state of 2-. Each transition metal atom has six nearest neighbor chalcogens, while the chalcogens are bonded to three nearest neighbor transition metals. The crystals can be easily cleaved, and they tend to grow in small platelike crystals. The small platelike crystallites easily slide past each other, and the first uses for TMDs took adVantage of this mechanical property. $MoTe_2$, as well as the other Mo and W TMDs were used as a solid state lubricant in high vacuum applications since the 1940s[6].

Besides their useful mechanical properties, TMDs host a wide variety of electronic phenomena and phase transitions. The class includes semiconductors like the $MoX_2$[7, 8], $WX_2$[9], $SnX_2$[10], $HfX_2$[11], $ZrX_2$[12], and $TiX_2$[13], semimetals such as $TaS_2$[14], half-metals[15] such as $CoS_2$, metallic materials, and superconductors[16] such as $MoS_2$. The ground state structure of a compound depends on the occupancy of the d-electrons in the transition metals. For The transition metals in group VIB (Cr, Mo, W), the 4+ oxidation state leaves a partially filled d-band. These compounds tend to be 2H with a semiconducting gap that increases when going from S to Se to Te, although other polytypes can be achieved through annealing or chemical treatment[53]. For the metals with an empty d-shell in the 4+ oxidation state the TMDs tend to form with a 1T ground state[54, 55].

## 3.3 Properties of TMDs

The various TMDs host a wide range of physical processes. The most studied TMDs are compounds that contain Mo and W, though the Nb, Ta, and Ti compounds have also received considerable attention. TMDs are noted to contain excitons, topological edge states in Weyl semimetals, charge density waves, and nonsaturating magnetoresistance, among other properties. The technological possibilities of these materials are vast, as they have been studied for use in optoelectronic devices, battery technology, field effect transistors, and sensors in the search for light, flexible thin film technologies. In following sections the physical phenomena found in TMDs

will be discussed and some of the technological applications will be explained to illustrate the motivation for TMD research. This will put the research into the CDW of $TiSe_{2-x}Te_x$ in later chapters of this work into proper context.

### 3.3.1 Exciton Physics in TMDs

In semiconductors, the conduction band is made up of electrons while the valence band is made up of holes with a small band gap. The energy scale of the bandgap for a semiconductor is typically on the order of 1 eV[56]. The energy scale of less than 1.7 eV are in the IR range, while 3.4 eV is the high end of the visible light spectrum. In a typical semiconductor, optical transitions occur from interband transitions in which a photon of sufficient energy excites electrons from the valence band to the conduction band. When an electron is excited it can interact with the hole and form a bound state. The bound state is known as an exciton. The binding energy of the exciton is typically slightly less than the bandgap. In the case of $MoS_2$, the bandgap is 1.2 eV in the bulk and 1.9 eV in the monolayer while the exciton binding energy is between 0.5-0.9 eV in a monolayer and 0.4 eV in a bilayer[57].

Excitons can be observed as resonances in the absorption spectrum or photoluminescence of a material. In many of the TMDs, there are two distinct exciton binding energies, one corresponding to the exciton and the other to a trion, which is a charged quasiparticle that is made up of an exciton with either an extra hole or electron[58]. These exciton states have been observed in $WS_2$[59], $WSe_2$[60], $MoS_2$[61], and $MoSe_2$[62].

The binding energy of excitons in TMDs can be controlled by electrostatic effects or strain. Strain in $MoS_2$ changes it from a direct to indirect bandgap material[63]. When this occurs, the intensity of the exciton peaks change and there is a shift in the optical spectrum[64]. When excitons recombine, they emit light, called electroluminescence (EL). The change in EL brought about by strain makes TMDs good materials for strain sensing applications[65], and $MoS_2$ has been used to design sensors that can be used for electronic skin with very high sensitivity[66] or for atomically thin touchscreens. The change in the optical spectrum of $MoS_2$ is shown in Fig. 3-3.

Excitons can also act as carriers and lead to a photocurrent with a strong dependence on the p-n doping of a semicondutor. The photocurrent occurs when the exciton in a singlet state reaches a heterostructure junction. At this point, if the energy of the interface is less than the exciton binding energy the exciton dissociates and the electron is used as a carrier in the semiconductor[67]. In a standard semiconductor, an electron excited into the conduction band will quickly thermally relax to the band edge, leading to a quantum efficiency with a theoretical maximum of 31%. With excitons a photon with energy of an integer multiple of the binding energy can produce multiple excitons. If these excitons can be harvested more quickly than they can recombine, then the quantum efficiency of the solar cell can be maximized[68]. This is promising for atomically thin film photovoltaic applications using TMD heterostructures[69].

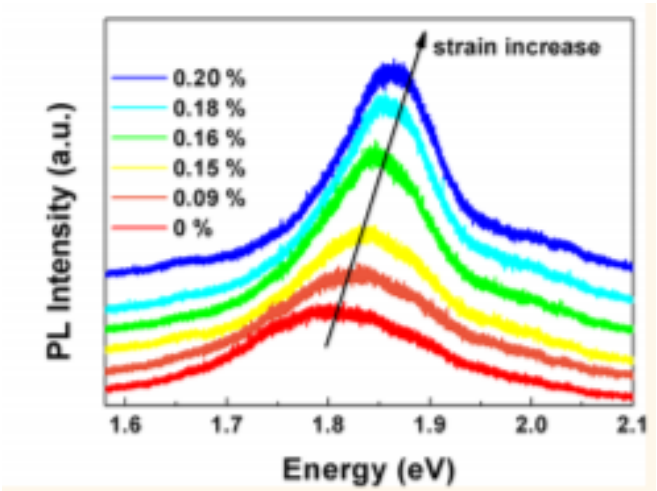


**Figure 3-3:** The exciton binding energy increases and the intesnity of photoluminescence increases when strain is applied to $MoS_2$. This can be used for strain sensing technologies[65].

## 3.4 Raman Spectroscopy of TMDs

The TMDs have two Raman active modes. The active modes are similar in both the octahedral and trigonal prismatic modes. With the $A_{1g}$ mode, the transition metal sublattice is stationary while the chalcogen layers move in plane in opposite directions.

The $E_{2g}$ mode is an in-plane phonon mode in which the metal sublattice moves in the opposite direction of the chalcogen sublattice[70]. Raman active modes are shown in Fig. 3-4 Like the excitons, the Raman modes are strongly dependent on the number of layers and strain. In bulk materials, the $A_{1g}$ mode is more energetic than in the monolayer, as additional layers stiffen the out of plane vibrations. Conversely, the $E_{2g}$ modes become less energetic as the the in plane bonds are more relaxed[71]. The $A_{1g}$ mode is sensitive to doping but not strain, while the $E_{2g}$ mode is not changed significantly with doping, but the degeneracy of the mode is lifted when strain is applied along one axis[72].

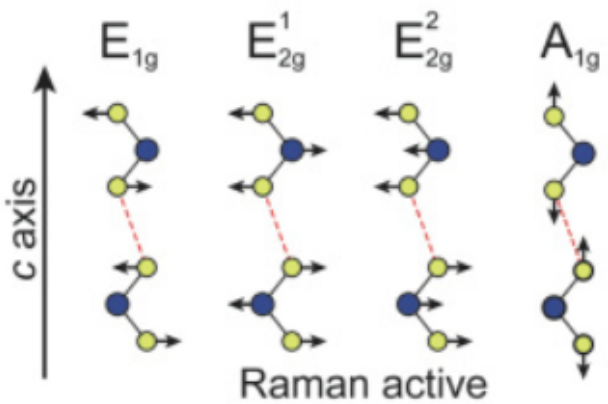


**Figure 3-4:** The Raman active modes of TMDs are shown[73].

## 3.5 Topological Weyl Semimetals

Insulators and semimetals have been classified based only on their band gap and dispersion. Recently, it has been shown that materials can be further classified by the existence of topologically protected edge states. These metallic surface states that occur in the gap of an insulator are caused by band inversions due to strong spin-orbit coupling which results in nontrivial band topology[74].

In systems with this band inversion, massless Dirac fermions can be created with linear dispersion, where the dispersion meets at a point, called the Weyl point. Weyl points occur in pairs with opposite chirality. The opposite chirality Weyl points are

antiparticles of each other and annihilate when they coincide in momentum space.

There are two types of Weyl semimetals. In Type-I Weyl semimetals, the points come together such that the Fermi surface collapses to a single point. For Type-II semimetals, the Weyl point occurs where an electron pocket and a hole pocket touch in momentum space. The TMDs $MoTe_2$[75] and $WTe_2$ are proposed to be Type-II Weyl semimetals. In these materials, two to four pairs of Weyl semimetals connected by Fermi arcs. Experimental evidence of the Weyl nature of these materials is inconclusive, as the Weyl point occurs above the Fermi level, though Fermi arcs have been seen in $MoTe_2$[76].

## 3.6 Magnetoresistance

Another recent TMD development includes the discovery of nonsaturating magnetoresistance in $WTe_2$[18], seen in Fig. 3-5. As explained in Chapter 2, large magnetoresistance is a very uncommon property in materials. Large MR is especially uncommon in nonmagnetic materials. In $WTe_2$ the MR reaches 2,500,000 % at 45 T and 4.5 K and does not saturate. The nonsaturating MR only occurs at temperature below 150 K but is not observed to coincide with a structural phase transition. The MR is also highly anisotropic, and occurs with a magnetic field applied along the W chain, but reduces by at least 90% in other directions. The anisotropic MR of $MoTe_2$ is also very large, reaching up to 32000% at 9 T. The mechanism behind the MR is not yet well understood.

## 3.7 CDW in TMDs

As quasi-2D materials, the TMDs are good candidates for low dimensional physics. As discussed in Chapter 2, CDWs are common in two dimensional materials. It comes as no surprise that several of the TMDs exhibit CDW physics. Additionally, CDW order frequently occurs in proximity to superconducting order and superconductivity has been observed in all TMDs that host CDWs. The most studied TMDs with CDW

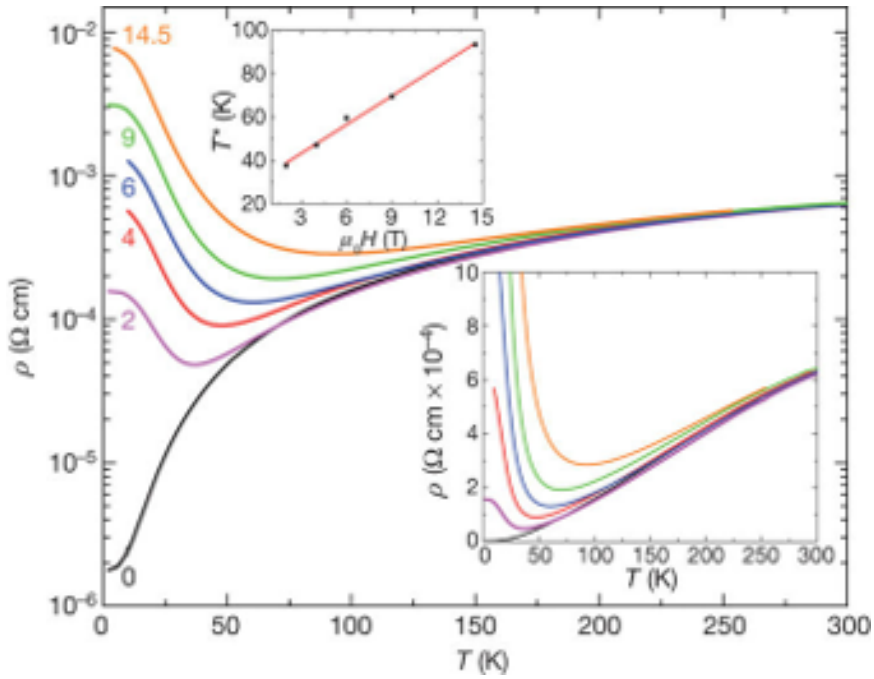


**Figure 3-5:** The large, nonsaturating magnetoresistance in $WTe_2$ is a recent development in the rich field of TMD physics.[18]

order are the Nb, Ta, and Ti compounds.

CDWs can be detected either using transport measurements or diffraction. With transport measurements, most of the TMDs with CDWs are metallic at low temperature with a sharp peak in the resistivity at the transition temperature. The CDW is seen in the diffraction pattern as superstructure peaks corresponding to the reciprocal lattice of the expanded cell.

$TaTe_2$ and $NbTe_2$ have a 3 x 1 CDW superstructure. The materials have a deformed 1T phase, in which octahedrally coordinated Ta and Nb atoms form zigzag chains due to a monoclinic distortion[77]. The CDW structure is shown in Fig. 3-6. It has been shown that Fermi surface nesting can be used to describe the origin of these CDWs[78]. Due to the distortions, this is a one-dimensional phenomenon, although there are three degenerate distortion directions.

$TaSe_2$ forms a CDW in its 1T, 2H, and 4Hb polytypes[79]. The CDW first goes into an incommensurate CDW phase before entering the commensurate phase. The commensurate phase has a $\sqrt{13} \times \sqrt{13}$ superlattice expansion that follows a star-of-David ordering motif, shown in Fig. 3-7. 2H-$NbSe_2$ has a CDW transition at 33 K and

is a superconductor below 7.8 K[80]. Unlike the one dimensional CDWs, the Fermi surface of these materials are not conducive to Fermi surface nesting. Studies have shown that phonon softening by electron-phonon interactions is needed to explain the CDW [81].

$NbS_2$ is superconductor below 6 K[82]. It is unusual among the TMDs as it is the only superconducting TMD that does not also have a CDW phase. Studies of the Fermi surface show no likely nesting vectors. There are, however, phonon softening and changes in the density of states that normally accompany a CDW. This indicates a latent CDW brought about by electron-phonon interactions and that the electron-phonon interactions drive the CDW[83].

While it is clear that the two dimensional CDWs in the TMDs are more complicated than the simple Fermi surface nesting picture described in Chapter 2, the mechanism for the CDW for most of the compounds is a matter of debate and is the motivation for the study of $TiSe_{2-x}Te_x$ in Chapter 6. The CDW in $TiSe_2$ is a commensurate 2 x 2 x 2 superlattice with many theories about its origin. This work seeks to understand the interactions that can lead to CDW formation in TMDs.

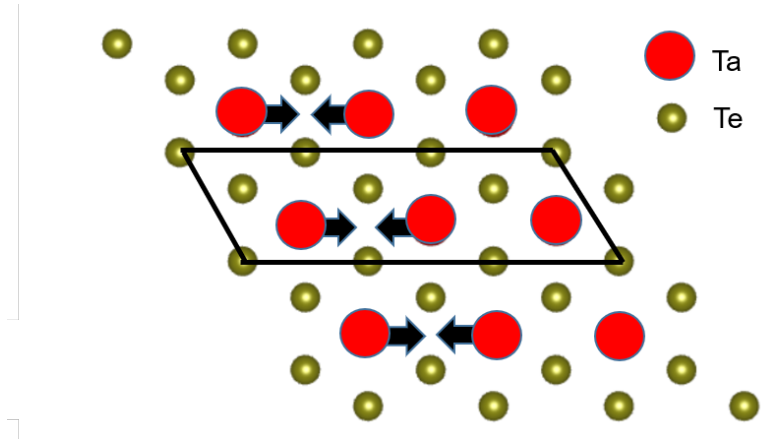


**Figure 3-6:** The CDW order of $TaTe_2$ is shown with red Ta atoms and brown Te atoms. The 3 x 1 superlattice ordering is similar to the superlattice on $NbTe_2$.

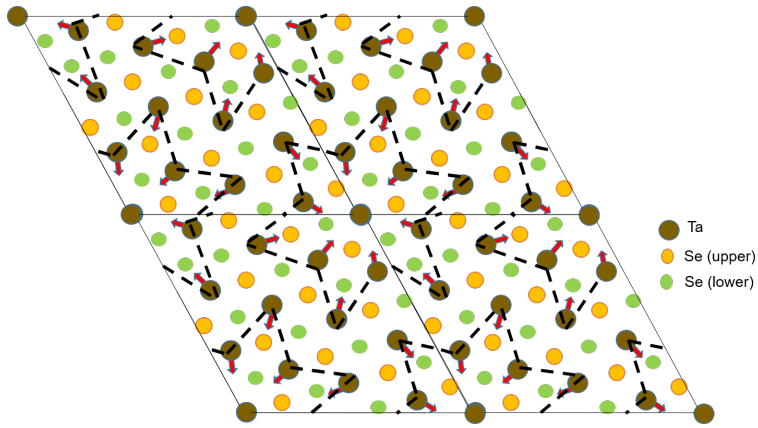


**Figure 3-7:** $TaSe_2$ forms a star-of-David CDW with 13 Ta and 26 Se in the unit cell.

## 3.8 TMD Device Applications

With a wide variety of phenomena present in TMD systems, it is possible to design a number of diverse devices. TMDs can be used as field effect transistors, solar cells, strain sensors, fuel cells, catalysts, light emitting diodes[20], optoelectronic devices, and photosensors[23], among other things. The following section will give brief descriptions of a few of these applications to give a sample of the motivations behind TMD research.

### Field Effect Transistors

One of the most promising applications to ultrathin semiconductors is their use in field effect transistors (FET). Metal oxide semiconductor field effect transistors (MOSFET) are the basic building blocks of digital electronic circuits. In order to create a logic gate, it is necessary for a material to have two distinct conductance states, typically separated by at least 1 eV. Graphene, with its gapless dispersion, does not satisfy this criterion and other atomically thin materials are more favorable.

Among the TMDs, monolayer $MoS_2$ has a field effect carrier mobility significantly lower than graphene[17]. The carrier mobilities[84], band gap, and on/off ratios are good for gate control in electronic devices at room temperature. Although significant work in optimization would be needed to replace Si and other well studied semiconductors, TMDs are ideal for flexible, thin film electronic device applications in the

near future.

### Solar Cells

Semiconductors with a bandgap in the solar spectrum are valuable for photovoltaic applications. The sun is a blackbody source with a temperature of 5800 K. The solar spectrum peaks in the visible range with a long tail in the IR. To date, Si and GaAs are the most used semicondcutors for photovoltaic devices. Many promising materials, such as black phosphorous and As allows have issues with cost and scalability. Thin TMDs are promising as they are nonreactive, cheap to produce, and have band gaps ranging from 1-2 eV[19].

In thin semiconductors such as TMDs, an issue that prevents widespread adoption for use as solar cells is low absorption. As light trapping techniques are developed, these materials will become more tenable. Strategies for light trapping include reflectors to capture light that passes through the active layer, and resonators that increase absorption.

### Fuel cells

The oxygen reduction reaction (ORR) is the most important chemical reaction for energy conversion in fuel cells. The ORR occurs at the cathode of a proton exchange membrane (PEM) fuel cell. PEM fuel cells are designed to convert hydrogen to electronic energy. The conversion of hydrogen and oxygen to water is an exothermic reaction. $H_2$ is incident on the anode, which dissociates into a dielectric when it percolates accross the membrane. The cathode has an air intake that brings oxygen into contact with the hydrogen ions. The ORR is a slow kinetic reaction. In order to increase the rate of the reaction to generate more energy, a catalysis must occur at the cathode.

The most commonly used cathodes are Pt based. As Pt is very expensive, cheap materials for fuel cells are under development. The TMDs have been studied for this process so that precious metals will not be needed[21]. For a layer of TMD, the chalcogen atoms at the edge are unbonded and free to bind to other molecules. The

TMD catalysts can bind to $O_2$ molecules and fix them in place, allowing for improved kinematics that speed up the interaction. The Ta and Nb TMDs have been shown to have the best catalytic properties of the class of materials[85].

### Photocatalysts

Not only are TMDs promising materials for fuel cells, they can be used as a photocatalyst to generate hydrogen fuel from water[22]. A photocatalyst is a material that aides in a chemical reaction without being consumed and are aided by photons. In aqueous solutions, H+ ions dissociate and are free to bind with negative carriers. When a photon excites an electron in $MoS_2$ nanosheets, the electron can move to the surface of the S plane. When the H binds to the free electron, it can bond with another H atom and form $H_2$ gas. Cheap, efficient ways of hydrogen fuel generation are important in the development of clean energy technologies.

# Chapter 4

# Antiferromagnetic Materials

## 4.1 Introduction to Antiferromagnets

The utility of ferromagnetic (FM) materials, with spins aligned in the same direction, has been understood for millenia, since the ancient Greeks noticed that magnetite, also called lodestone, attracts itself and iron. The first thorough scientific studies of magnetism began in the $16^{th}$ century, which lead to William Gilbert discovering that the Earth itself is a FM. Research into FM as it pertains to solid state physics began in the $19^{th}$ century, primarily by Pierre Curie and Pierre Weiss. Curie studied the statistical mechanics of the materials and found that magnetic ordering breaks down spontaneously at high temperature[86, 87], with the transition temperature known as the Curie temperature. Weiss explained the atomic and molecular reasons for the magnetic field in terms of the magnetic moments of individual unpaired electrons in atoms[88]. Based on their work, the Curie-Weiss law describes the change in susceptibility of the paramagnetic phase of a FM material with the formula:

$$\chi = \frac{C}{T - T_C}, \tag{4.1}$$

C is the Curie constant for a material, T is the temperature, and $T_C$ is the Curie temperature. Weiss' theory describing the energy of a magnetic material assumed that the energy of the system was only due to the sum of the magnetization of all

atoms in the material. With the quantum mechanical description of magnetism by Heisenberg, it became clear that this was insufficient, as it was important to look at local magnetic fields rather than the general magnetic field. Néel improved upon by taking the local magnetic fields and thermal fluctuations into account. Néel found that it was possible for negative interactions between adjacent atoms, forming two distinct sublattices with opposite orientation. If the magnetic moments of the two sublattices cancel each other out, the material is an AFM. For an AFM, the susceptibility follows a modified Curie-Weiss law, except that since there is no $T_C$ and instead the temperature at which $\frac{1}{\chi}$ approaches zero is negative and at the Néel temperature the susceptibility is discontinuous. A common explanation for AFM is the superexchange interaction, described by Hendrik Kramers and Phillip Anderson[89]. The superexchange interaction occurs when two magnetic atoms interact indirectly by sharing atoms with the same donor ligand, such as O in MnO, leading to a AFM structure. The Goodenough-Kanamori rules were developed to describe when AFM is likely to occur, and states that if the exchange occurs between two half filled orbitals the interaction will be AFM, but if one is half filled and the other is filled or empty it will be FM[90].

## 4.2 Exchange Bias

As discussed in Chapter 2, AFMs are currently used in FM devices to pin FM layers. The process by which the FM layers are pinned is called exchange bias. Exchange bias occurs because of interactions at the interface of the AFM and FM films. An exchange bias device is created by heating a FM and AFM heterostructure above the Curie and Néel temperature and cooling under a magnetic field. At the interface, the local field from the AFM is FM, despite the AFM global field. This leads to a domain wall with significant energy beyond the energy contained in the FM field. To flip direction of the FM order, the energy of the domain wall must be overcome, which means that the field required to flip the spins is greater. This leads to a shift in the hysteresis curve, as seen in Fig. 4-1.

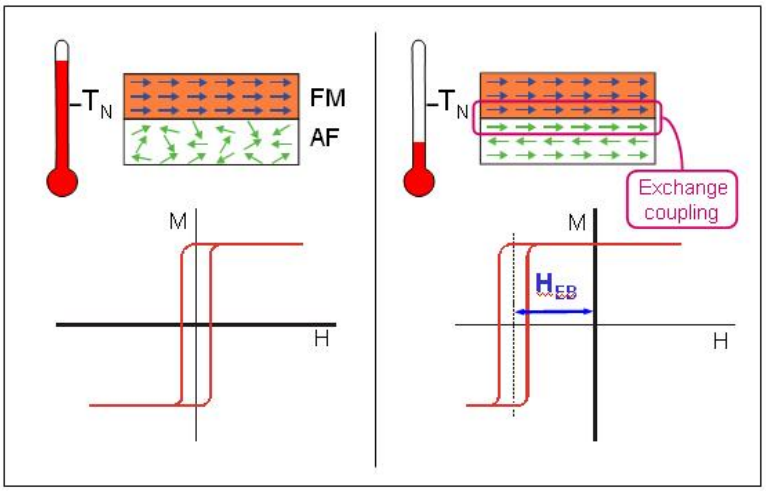


**Figure 4-1:** The exchange bias effect leads to a shift in the hysteresis loop of FM thin films in proximity to AFM films.[91]

## 4.3 Overview of Antiferromagnetic Materials

The most commonly used AFMs for industrial applications are the metallic AFMs. These materials are typically alloys of Mn, such as FeMn, IrMn, and PtMn. Other metallic AFMs with potential for technological applications include $Mn_2Au$, TiAu, $CrB_2$, FeRh, GdSi, GdGe, $GdAu_2$. They are commonly used for exchange bias applications in read heads and magnetic hard drives. The AFM semiconductors have recieved much less attention than their metallic and insulating counterparts. Nevertheless, AFM semiconductors have interesting properties that will make them a subject of increased study in the future. $SrIr0_4$, CuMnAs, and MnTe are some of the semiconducting AFMs to recieve the most attention.

AFMs have a diverse set of crystal structures. FeMn is a face centered cubic system with a Néel temperature of 490 K[92]. $IrMn_3$ has a similar face centered cubic structure as FeMn, but with two crystallographic phases. In the $\gamma$-$IrMn_3$ phase, the Ir and Mn atoms are distributed randomly, while the other phase has the Mn on the cubic faces. The magnetic order of the chemically ordered phase is a triangular AFM, where the three moments of the triangle point to a common center. The chemically disordered phase has a more complex magnetic structure, and forms a spin density wave. The Néel temperatures are 730 K for the chemically disordered phase and

1000 K for the chemically ordered phase. The exchange bias in the ordered phase is much stronger than the disordered phase[93]. The FeMn and $IrMn_3$ systems are interesting among the class of materials because their magnetic structure has broken time reversal symmetry, leading to a large spin Hall effect.The spin Hall effect is a phenomenon in which electrons of opposite spins accumulate on opposite sides of a material, leading to a spin current. The spin Hall angle is a measure of the strength of the spin orbit torque in the spin hall effect. $IrMn_3$ has been used to show that the spin orbit torque is strongly dependent on the facet of the crystal at the interface. In $IrMn_3$, the (001) spin hall angle is much larger than the (111) or polcrystalline spin hall angle[94]. From this it is clear that the exchange bias and spin hall effects depend on the specific face of the material.

The physical properties of the AFMs are very dependent on the size of the atoms. Heavier atoms lead to stronger spin-orbit effects. Many metallic AFMs combine the high magnetic moment of the Mn 3d orbitals and the strong spin orbit coupling of the 5d orbitals of heavy metals. The exploitation of these properties can lead to tuning for spintronic devices with different spin penetration depths[95], changes to magnetic order with spin transfer[96], and spin pumping [97].

## 4.4 AFM Spintronics

### 4.4.1 Anisotropic Magnetoresistance

Anisotropic magnetoresistance (AMR) is an important property of AFM spintronic materials. AMR is the dependence of resistance on the direction in which the field is applied. AMR allows the spin state of the device to be read. While AMR is weaker than GMR and CMR, it is easier to detect because it is a bulk property of a single phase and does not depend on complicated thin film heterostructures. Crucially for AFM spintronics, AMR does not depend on the magnetization and therefore is present in AFM in addition to FM materials.

Measuring AMR in AFMs is challenging because, unlike in FM, there is no sim-

ple way of controlling the spin direction in an AFM. The metallic AFM FeRh was among the first AFM shown to exhibit AMR. FeRh has a high temperature FM phase that transitions to AFM around room temperature. The AFM has a bi-stability in which the moments can align along either the a- or b- axis. By applying a magnetic field through the FM to AFM transition, the direction of the spins of FeRh can be controlled in the AFM phase[98]. The resistance along the axis of the perpendicular to the spins is around 2% higher than the resistance in the direction aligned or antialigned with the spins. This device is known as a memory resistor and is a building block for AFM spintronics.

In FeRh, which has two stable spin configurations, AMR was only measured along the (100) and (010) crystallographic axes. MnTe, a semiconducting AFM, is a material in which AMR can be measured with a full angular range of magnetic field configurations. In MnTe with the direction of rotation kept fixed, the magnetic field was rotated. This results in a sinusoidal AMR with the AMR ranging between 0.5 and -0.5%. This occurs because MnTe has a hexagonal crystal structure with three stable AFM phases. When a field is applied, AFM domains form so that the average direction of the spins aligns with the field[99, 100].

While AMR makes reading a AFM spintronic memory simple, the small magnitude of MR makes miniaturization difficult[101]. The tunneling AMR (TAMR) effect occurs when the electrons are allowed to tunnel through an insulator into a non-magnetic metal[102]. In these AFM/insulator/metal heterostructures, changing the alignment of the spins can change the resistance by up to 160%. The design challenges with these heterostructures involve finding ways to control the AFM ordering. This has been accomplished by exchange coupling the AFM to an FM, and has been demonstrated using a NiFe/IrMn junction with a MgO insulator and Pt metal for the tunnel junction[103]. This leads to a strong TAMR at low temperature that is not robust at room temperature. Small room temperature TAMR has been shown to be possible[104], but has not yet been seen with a large enough effect to be useful and more work is needed to optimize these structures.

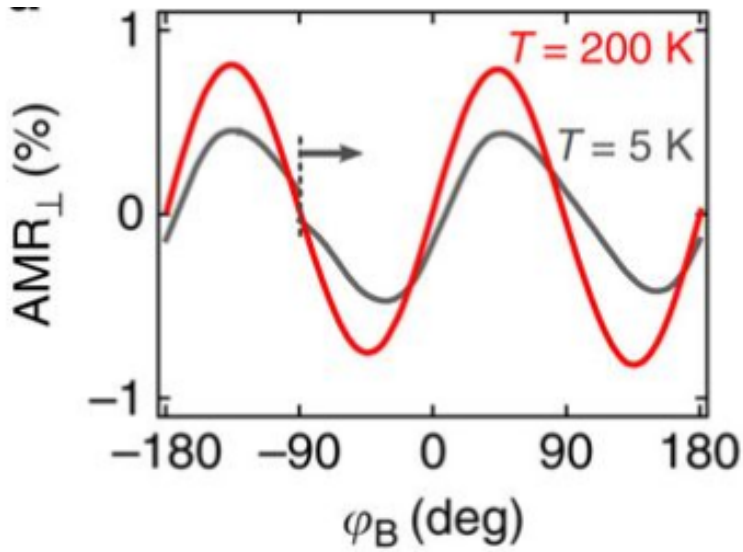


**Figure 4-2:** The transverse AMR of MnTe is shown at 200 K and 5 K[100].

### 4.4.2 Spin-orbit Torque

Spin-orbit torque (SOT) can be used as a strategy for switching AFM order. With SOT, no external magnetic field is needed to switch the ordering. Instead, this can be accomplished using a current. The process is called the Edelstein effect, or the inverse spin-galvanic effect. The Edelstein effect only occurs in systems with broekn inversion symmetry. It is an effect of the spin Hall effect, in which a current leads to a spin polarized splitting in the transverse direction. The spin current interacts with the local magnetic fields and leads to a torque on the magnetic atoms. The Elestein effect differs from the current switching described in Chapter 2 in that the effect does not depend on spin injection from a polarizer and is an effect that occurs in a single phase. The Edelstein effect was first achieved in semiconducting FMs with broken inversion symmetry, GaMnAs and NiMnSb.

While FMs can be easily switched without SOT, the use of SOT as a switching mechnism for AFMs would greatly increase their utility in spintronic devices. SOT works well for AFM with the correct symmetry because the spin-galvanic effect is a completely local interaction. This also means that it is robust to disorder. An example of a AFM in which switching has been achieved using SOT is $Mn_2Au$. For this material, the nonmagentic phase is inversion symmetric. In the magnetic phase,

the two magnetic sublattices have locally broken inversion symmetry. This symmetry breaking allows for spin polarization and switching even without a globally broken inversion symmetry.

### 4.4.3 Memory Devices

Using AFMs instead of FM materials has several important advantages. Among the most important is the way they interact with external magnetic fields. AFMs do not reorient easily in a magnetic field, making them less volatile than FM. Without a net magnetic field, AFMs are invisible to other devices and can be more densely packed into valuable chip real estate, allowing for higher total memory devices. Reorientation of AFMs also occurs in the terahertz frequency time scale, making them ideal for ultrafast dynamics.

Several proof of concept devices have been created using AMR and spin-orbit torque physics. The first is FeRh memory. A FeRh bit can be created by making two FeRh wires that are connected at the center[105]. When the wires are joule-heated above the Néel transition of 380 K in a magnetic field, the moment can be reoriented such that one of the wires runs collinear to the moments and the other runs perpendicular. This leads to a difference in resistance between the two wires that can be easily switched. The state of the bit is read with AMR. The setup for the FeRh bit is shown in Fig. 4-3

CuMnAs has been used to make a simple memory device using SOT as the write mechansim and AMR for the read mechanism. CuMnAs is a material with broken inversion symmetry in the magnetic phase[106]. It was further demonstrated in CuMnAs that the material can hold more than just two states, by using short pulses to partially reorient the material in a way that the resistance reliably and predictably changes. CuMnAs is further intriguing because it is compatible with existing technology and can be deposited onto Si wafers. Switching has also been demonstrated using picosecond pulses, allowing for switching without mechanical contact. Switching of this nature is important for making THz reading and writing possible. In contrast, for FM memory devices, 5 GHz is the approximate theoretical maximum for writing[107].

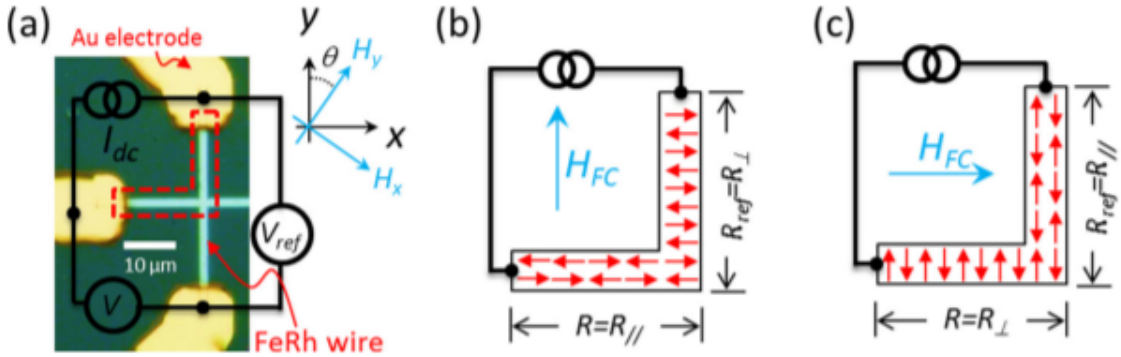


**Figure 4-3:** (a) The setup for the FeRh bit measurement with FeRh wires attached to gold leads, a primitive AFM spintronic memory device. (b) The first state, when the magnetic field during cooling is in the y direction. (c) The second state, when the magnetic field upon cooling is in the x direction.[105]

# Chapter 5

# Experimental Techniques

## 5.1 Neutron and X-ray Scattering

### 5.1.1 Introduction

### 5.1.2 Neutrons

In 1932, James Chadwick discovered the neutron[108]. Neutrons are neutral particles with mass of 1.67 $\times 10^{-27}$ kg and spin $\frac{1}{2}$. From the de Broglie relations, the energy of the neutron corresponds to the wavelength with the equation:

$$E = \frac{h^2}{2m\lambda^2} \tag{5.1}$$

Where $h$ is the Planck number, $m$ is the mass of the neutron, and $\lambda$ is the wavelength of the neutron. When neutrons are produced at a neutron source, their energy can be controlled when they pass through a material that acts as a moderator. While traveling through the moderator, the neutron is slowed by collisions with the H atoms of the moderator and the kinetic energy spectrum of the neutrons is that of the Maxwell-Boltzmann distribution, shown in Fig. 5-1, centered at the moderator temperature. The neutrons are slowed by elastic collisions in the moderator. Therefore, the ideal moderator is made up of small atoms, and water is a common moderator. Thermal and cold neutrons, created by passing through a moderator at room temperature or

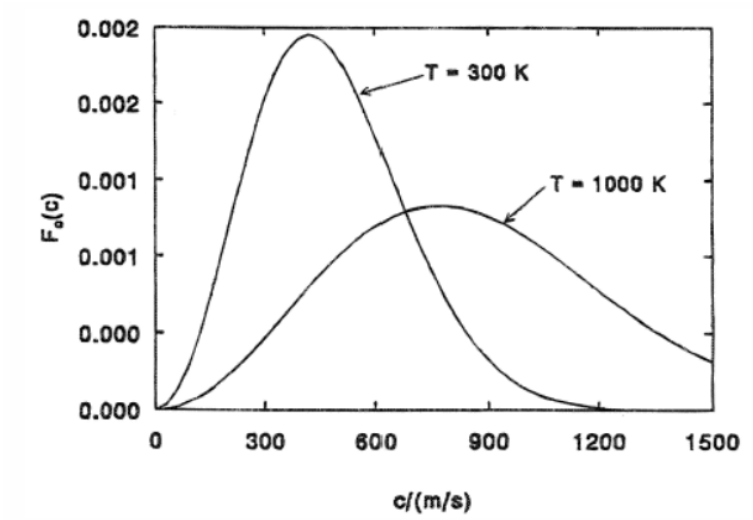


**Figure 5-1:** The Maxwell-Boltzmann distribution centered at 300 K and 100 K[109].

colder, have a wavelength on the order of 1 to 10 Å and an energy on the order of meV, which makes them ideal for studying the structure of materials and dynamics. Neutrons have several disadvantages over X-rays. X-rays are easy to produce, while neutrons must be created in a large facility. Additionally neutron sources have a lower luminosity than X-ray sources. Neutrons also interact more weakly with matter than X-rays. Despite these issues, many properties of neutrons make them ideal for investigating condensed matter physics. The reason that neutrons scatter more weakly from matter than X-rays is that X-rays, as photons, interact through electromagnetic interactions and scatter strongly off of the electron cloud. Neutrons, on the other hand, are neutral particles that do not interact with the electron charge and scatter off of the nuclei, which on the length scale of the interactions are point particles. While this has some drawbacks, as mentioned above, it has two large advantages. First, neutrons have a greater contrast between different species of atoms, as seen in Fig. 5-2. For X-rays, the scattering length increases with atomic numbers, as X-rays scatter more strongly from atoms with a larger number of electrons, and large atoms have very similar scattering lengths, as seen in Fig. 5-3. Neutrons, on the other hand, have more contrast in the cross sections of atoms with similar mass and are even sensitive to different isotopes of the same atom. The other advantage of neutrons weakly interacting with electrons is that neutrons penetrate fully into the

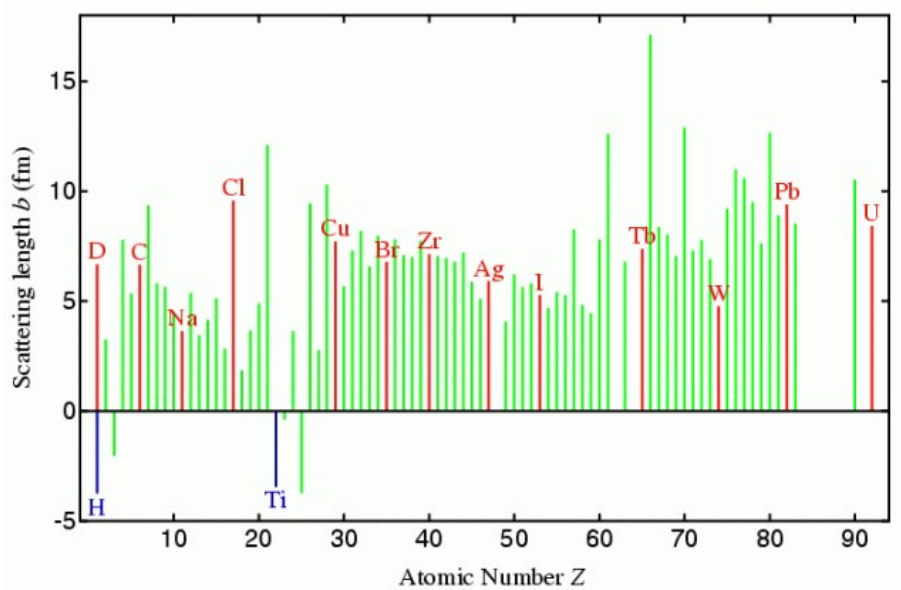


**Figure 5-2:** Neutron scattering length of atoms as a function of atomic number[110].

crystal and are good for probing bulk properties in crystals. Finally the spin of the neutron is important as it allows the neutron to scatter off of unpaired electrons in a material. Because of this, neutrons can be used to study spin-spin correlations, and neutrons are ideal for solving magnetic structures.

### 5.1.3 Neutron Sources

Neutron experiments can be carried out at large user facilities where a variety of instruments are set up for specialized experiments. There are many ways that neutrons can be produced, and two are used at these facilities. These two kinds of sources are reactor sources and spallation sources. At reactor sources, neutrons are a byproduct of fission reactions of heavy isotopes such as $U^{235}$. When a slow neutron collides with $U^{235}$ it joins with the nucleus to form an $U^{236}$ isotope. The process for the fission of uranium is shown in Fig. 5-4. About 18% of the time, this isotope will be a stable waste product of the reactor, but for 82% of collisions, nuclear fission will produce smaller elements and an average of 2.4 neutrons. Some of these neutrons are used to sustain the chain reaction, but many are released and can be harnessed by scientists for diffraction experiments.

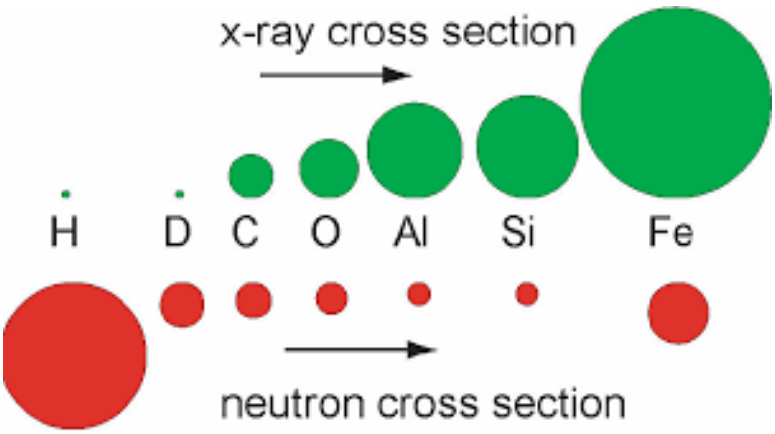


**Figure 5-3:** The scattering cross section of X-rays compared to neutrons. For X-rays the cross section increases with atomic number, but neutrons do not have a consistent trend[111].

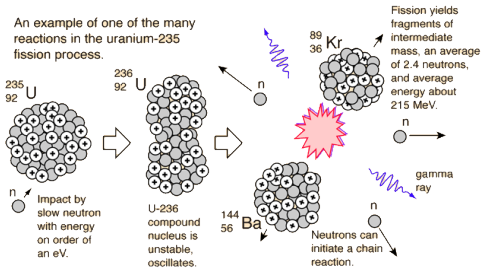


**Figure 5-4:** The process for nuclear fission of Uranium-235 is shown. It is an important way of generating neutrons for scattering experiments[112].

In the United States, there are two active user facilities that produce neutrons with a reactor source that were used for this thesis. These are located at the NIST Center for Neutron Research (NCNR) in Gaithersburg, Maryland, and at the High Flux Isotope Reactor (HFIR) at Oak Ridge National Laboratory (ORNL.) The NCNR has been operating since 1975. It has 17 instruments and generates a power of up to 20 MW with a flux reaching $10^{15}$ n cm$^{-2}$ s$^{-1}$[113]. HFIR was designed to produce transuranic isotopes for medical and research purposes. All californium-252 used for medical purposes in the United States is produced at HFIR. As isotope production produces many cold and thermal neutrons, 15 neutron diffraction instruments are housed at HFIR, which operates at 85 MW with a higher flux than the NCNR reactor[114].

The other method of neutron production is spallation. At a spallation source, protons are accelerated using some combination of a linac, cyclotron, or synchrotron.

After the protons are accelerated to a very high energy, they are collided with a target creating high energy pulsed neutrons. Targets can be made of a variety of materials, such as lead, tungsten, or mercury. Spallation has an advantage over fission in that the number of neutrons produced per heat generated is much higher in spallation that fission. The pulsed nature of spallation also gives additional information during scattering experiments. The Spallation Neutron Source (SNS) at ORNL is the spallation source used in this work. SNS uses a liquid mercury source with a 60 Hz pulse and is currently home to 20 instruments.

## 5.2 Neutron Instruments

### 5.2.1 Constant Wavelength Diffractometers

At a neutron source, specialized instruments are built to carry out a wide variety of experiments. Instruments can be specialized for elastic or inelastic measurements, and be set up to measure a range of wavelengths or physical parameters to study the structure and dynamics of a material. In this thesis, data was collected at two kinds of instruments. The first of these is a constant wavelength diffractometer. The constant wavelength diffractometers used for this work are BT-1 at NIST center for Neutron Research and HB2-a (POWDER) at the High Flux Isotope Reactor. Constant wavelength diffractometer give high quality Bragg diffraction profiles that can be used to find the crystal structure of a material.

When neutrons are produced by a reactor source, they first pass through the moderator to slow them down. After the moderator, neutrons are passed through a collimator to focus the beam. The benefit of a greater distance betweeen the collimator and the monochromator is that the intensity of the neutrons on the sample is much greater, however the resolution is much worse for large angles when the beam must travel larger distances after leaving the collimator. After the collimator the beam passes through a monochromator to select a wavelength. The monochromators at BT-1 are Ge and Cu monochromators with a choice of three wavelengths. These

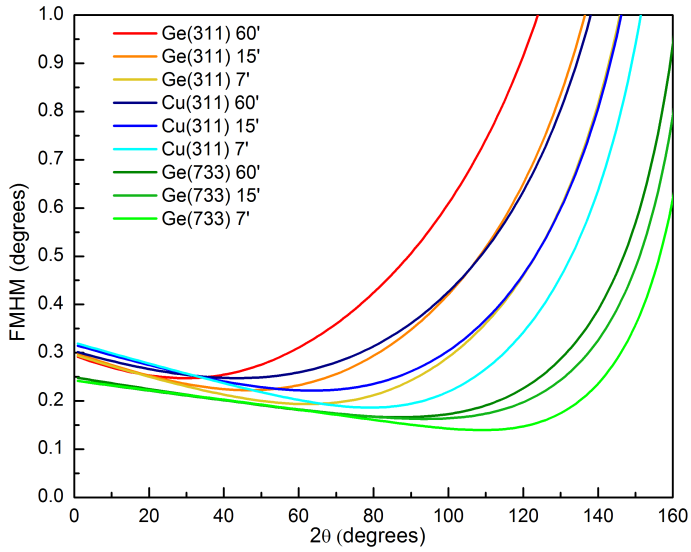


**Figure 5-5:** The resolution of BT-1 monochromator setups as a function of full width at half maximum vs. $2\theta$[115].

are 2.079 Å (Ge 311), 1.540 Å (Cu 311) and 1.197 Å (Ge 733). The resolution for the nine different configurations at BT-1 are shown in Fig. 5-5.

The Ge (311) monochromator has the highest neutron flux but has poor resolution at high angles. It is good for measuring magnetic materials and phase changes that have peak changes at low angles, as the length of a scan is less than the other monochromators. When many measurements are needed but high resolution is not needed, this is the best option. The Ge (733) monochromator is best for measurements where high angle reflections are needed, as it is possible to see more reflections. Unfortunately, the intensity of the neutron flux is much lower than the other monochromators and scans take a long time. Finally, the Cu (311) monochromator is optimal for most samples, as it has sufficient resolution and angular coverage for most measurements.

After leaving the monochromator, the neutron beam arrives at the sample. The samples are packed into vanadium (V) cans because vanadium does not scatter neutrons coherently. For temperature dependent measurements, the V can is attached to a closed cycle refrigerator (CCR) that uses helium to cool to temperatures as low

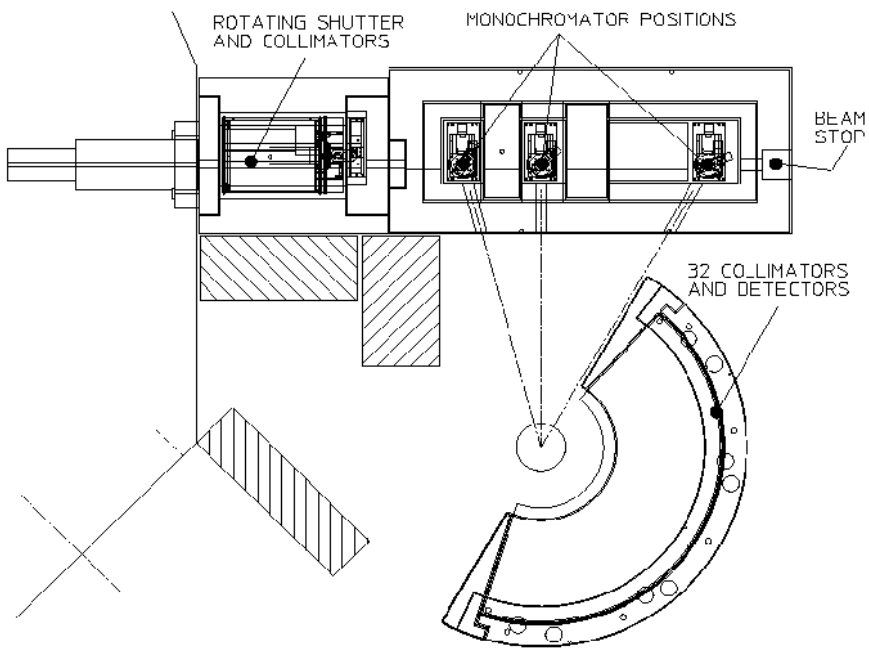


**Figure 5-6:** Schematic for the BT-1 instrument.

as 3 K. The detector at BT-1 consists of 32 $He^3$ detectors spaced 5° apart. $He^3$ detectors work because unlike most isotopes, $He^3$ interacts strongly with neutrons. The $He^3$ in the detector absorbs the neutron and decays to $H^1$ and $H^3$ ions, which can be measured. During an experiment, the detector bank rotates by 13° to give full angular coverage. As the detectors all lie in the same plane, the measurement is one-dimensional and can only be used for powders, not single crystals. The data from all of the banks can then be summed for the analysis. Fig. 5-6 shows the schematics for the full instrument as described above. The beamline HB2-a, also known as POWDER, at HFIR has a very similar setup but better neutron flux than BT-1.

### 5.2.2 Time-of-Flight Neutron Diffraction

In contrast to the constant wavelength diffraction method at reactor sources, pulsed neutron sources use the time-of-flight (TOF) method. Rather than a single wavelength selected by a monochromator, TOF instruments provide a neutron pulse with a distribution of wavelengths. As the wavelength uniquely defines the momentum and the pulses begin at discrete time intervals, the length of time between

the pulse and the detection, the TOF, can be mapped on to momentum transfer and d-space. TOF diffractometers have good resolution at high angles, and resolution can be improved by increasing the distance traveled and allowing the neutron wavepacket to disperse more. TOF diffractometers are also more efficient than constant wavelength diffractometers, as with no monochromator screening out most wavelengths all neutrons in the beam are used.

With a large bandwidth of momentum transfer, Q, the diffraction can be used to analyze the local structure of crystals. The nanoscale ordered materials diffractometer (NOMAD) is a TOF instrument that is tuned to have a large bandwidth of neutron energies and six detectors spaced at a wide range of angles. The resolution of NOMAD is not as good as HB2-a and BT-1, so structural determination is not as precise. The advantage that the large bandwidth gives is that the structure function can be Fourier transformed to investigate the local structure, which will be discussed in the next section.

## 5.3 Data Analysis

There is a wide range of methods that can be used to analyze data collected at a neutron source. The advent of computers has made crystallography research much more efficient. No longer do scientists need to spend their time indexing reflections by hand, and least squares refinement has made it much easier to find a precise model. The following subsections will describe the two main methods used to analyze the data in this thesis, Rietveld refinement, and Pair Distribution Function (PDF) analysis.

### 5.3.1 Powder Data Rietveld Refinement

Powder diffraction is sufficient to get a good Bragg profile. When a powder is well mixed, the crystallites are randomly oriented. The random orientation of the crystals leads to rings that average over all points in a given angle $2\theta$ or time of flight, which can then be converted to d-spacing or momentum transfer, Q, which do not depend on the instrument set up. The Bragg peaks occur at momentum transfers equal to a

reciprocal lattice vector with the relative intensities of the peaks determined by the atom positions. The Bragg profile can be used to find the average crystal symmetry of the material.

In the early days of crystallography, the most studied crystals were primarily simple, high symmetry crystals with clearly defined peaks and intensities. As structures become more complex, it becomes more likely that peaks overlap and that subtle differences in the intensity profile are important to the final structure. Although attempts were made to fit overlapping peaks with multiple Gaussians, the fact that peak shapes are not truly Gaussian made sufficiently complex profile refinements impossible. With the availability of computers, Hugo Rietveld worked to create a method that allows patterns to be fit by adjusting parameters to find a least-squares fit. The Rietveld method was revolutionary because instead of calculating the integrated intensity, it became possible to look at intensities at individual angles to carry out the refinement.

The General Structure Analysis System (GSAS) and its acommpanying graphical user interface, EXPgui, is a Rietveld refinement software that can be used to solve structure from a diffraction pattern. In order to get a good refinement it is important to have a reasonable guess at the final structure. The input parameters for the structure are the lattice parameters, which determine the peak positions, atomic locations, which determine the relative intensities, occupancy, and thermal factors. The profile pattern is also influenced by the instrument, and the profile shapes and constants are imported in the parameter file for the instrument. The lattice parameter is the first parameter refined and is refined during every round of the least squared routine. The occupancy and thermal parameters cannot be refined together, as they are coupled and affect the same parts of the profile. The goodness of fit can be measured with the R factor and $\chi^2$, defined as:

$$R_{wp}^2 = \sum w(I_c - I_{ob})^2 / \sum w(I_o b)^2 \tag{5.2}$$

$$\chi^2 = \frac{1}{N} \sum w(I_c - I_{ob})^2, \tag{5.3}$$

where $I_c$ is the calculated intensity, $I_{ob}$ is the observed intensity, w is the inverse of the uncertainty, and N is the number of data points. The R factor is weighted so that peaks have more weight than the background. For both goodness of fit measures, a lower number corresponds to a better fit.

### 5.3.2 Pair Distribution Function Analysis

Refinement of the diffraction pattern can be used to find the average structure of the crystal. This refinement only takes into account the Bragg peaks, however, and information in the diffuse scattering is lost. The diffuse scattering holds information about the local correlations and disorder away from the average structure. PDF analysis is a technique that can be used to look at the local structure of a material by finding a distribution of atomic pair correlations.

During a diffraction experiment, the quantity measured is the structure function, S(Q). For PDF analysis, it is important to know the exact background and the contributions from the instrument and can. For this, extra measurements of the empty instrument, empty vanadium can, and a vanadium rod are measured. These are used to correct the S(Q) data using the equation[116]:

$$I = \frac{(S - B) - \alpha(C - B)}{V - B}, \tag{5.4}$$

where S is the scattering from the sample, B is the background pattern, $\alpha$ is the absorption correction for the container, C is the empty can profile, and V is the vanadium rod profile. S(Q) is measured with multiple detector banks at a range of angles to maximize resolution in Q. The parameters of the experiment such as the geometry and the sample composition are entered, which allows for multiple scattering corrections and normalization. For samples with high inelastic scattering, the Placzek correction can be applied. This is typically only necessary for materials that contain

hydrogen.

After the corrections are accounted for, the different banks are combined to give S(Q) and the Q range is selected. The PDF is calculated by Fourier transforming the structure function S(Q)[117]:

$$G(r)_{\text{exp}} = \frac{2}{\pi} \int_0^\infty Q[S(Q) - 1] sin(Qr) dQ \tag{5.5}$$

In real space, peaks in G(r) correspond to atomic correlations. A PDF model can be calculated from the crystal model with:

$$G(r)_{\text{mod}} = \frac{1}{r} \sum_i \sum_j \frac{b_i b_j}{\langle b \rangle^2} \delta(r - r_{ij}) - 4\pi\rho_0 \tag{5.6}$$

where $b_i$ is the scattering length for atom $i$ and $\rho_o$ is the atomic density of the crystal.

Other similar functions are g(r) and $\rho(r)$. They can be derived from G(r) with the formula:

$$\rho(r) = \frac{1}{4\pi r} G(r) + \rho_0 \tag{5.7}$$

$$g(r) = \frac{\rho(r)}{\rho_0} \tag{5.8}$$

$\rho(r)$ is the pair density function, and when integrated gives the total number of bonds that an atom has at a given length. For g(r), the function is the probability of finding a bond at that length. These two functions have the advantage over G(r) that the error decreases as $\frac{1}{r}$, while G(r) has constant error.

As described by Warren, PDF is ideal for imperfect materials, as deviations from crystal structure can change the diffraction profile in ways that are difficult to analyze in Q space[118]. PDF analysis was originally used for amorphous structures and liquids. Without a crystalline structure, these materials have no sharp Bragg peaks. Despite a lack of long range order in liquids and amorphous structures, there is still short range order as the atoms tend to pack closely together. PDF analysis can be

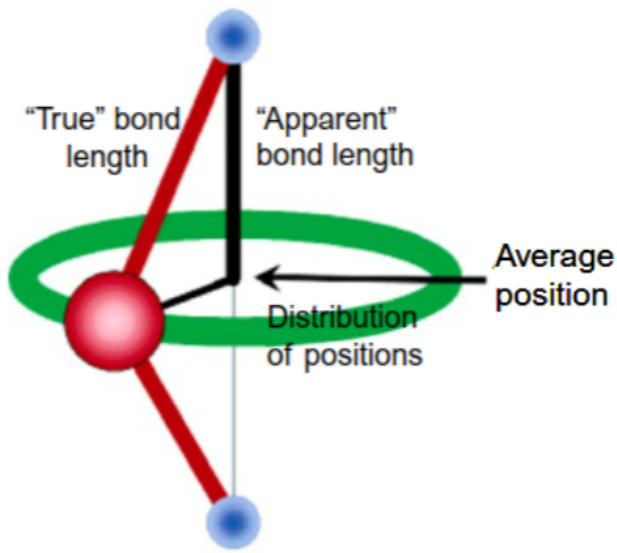


**Figure 5-7:** The shaded annulus shows the possible location for the atom, shown at random. All locations in the ring have the same bond length with the other atoms. As the distribution is random, the diffraction pattern shows an apparent bond length shorter than the actual bond length.[117].

used to find the nearest neighbor bond lengths and see the length scales at which the short range order breaks down. The method was extended to crystalline systems in order to investigate short range disorder that does not change the Bragg peaks but leads to diffuse scattering. Crystals in which distortions are random and disordered can have actual bond lengths that differ from the apparent bond length that is derived from the average long range order, as seen in Fig. 5-7. As an example, the transition between $\alpha$ and $\beta$ quartz have very similar structures that give identical Bragg profiles. PDF analysis, however, shows that as $\alpha$-quartz is heated to $\beta$-quartz, the bond length shortens.

Knowing how local disorder affects the crystal is very important to understanding the physical properties of a material and how electrons interact with the lattice. In this work, both crystal systems studied exhibit physical phenomena that cannot be understood from the average structure alone, and PDF analysis is used to gain insight into the physics of the systems.

## 5.4 Sample Preparation

There are a number of techniques used to prepare samples for diffraction experiments. The method chosen depends on which kind of system is being studied and what experiments are needed. For powder experiments, it is not always necessary to grow a large crystal and a polycrystalline sample will suffice, but for many experiments a larger crystal is necessary. The following sections detail the method for preparing samples for the experiments in this thesis.

### 5.4.1 Solid State Reaction of $TiSe_{2-x}Te_x$

For powder experiments with $TiSe_{2-x}Te_x$, it is fairly easy to grow the polycrystalline samples that will be crushed to a powder. The samples were prepared using the solid state reaction. Powders of Ti, Se, and Te were weighed in stoichiometric quantities. In order to achieve a homogeneos sample, the powders were ground with a mortar and pestle for 30 minutes. The well mixed powder was then pressed into a pellet. If the pellet was heated in air, oxygen would react with the elements and the correct phase would not be produced. Therefore, the pellet was sealed into a fused quartz ampoule and placed into a furnace. The furnace was heated to 800° C for 48 hours and allowed to cool to room temperature over the course of a day. The resulting pellet was shiny purple as seen in Fig. 5-8 and smelled like sulfur when the ampoule was cracked open. In order to achieve homogeneity in the crystal, the samples were ground and pelletized a second time. The new pellets were sintered in an inert atmosphere in an ampoule for and additional 48 hours and the phase was checked with X-ray diffraction.

### 5.4.2 Flux Growth of NaMnBi

NaMnBi is somewhat challenging to grow. The primary challenge of crystal growth for this compound is that Na, an alkali metal, is very sensitive to oxygen and moisture so all steps must take place in an inert atmosphere. Na also reacts with fused quartz, and care must be taken so that the Na does not touch the glass ampoule during the

**Figure 5-8:** A photo of the $TiSe_2$ puck after second sintering before it is ground into a powder.

growth process.

The method used to grow NaMnBi is flux growth. With flux growth, all constituent elements of the crystal are dissolved in a liquid[119]. The first step of flux growth is to heat all elements to above the liquidus temperature of the system. The liquidus temperature is the temperature at which the elements are fully soluble in the flux. After reaching a temperature about 50° above the liquidus temperature, the ingredients are allowed to equilibrate and form a uniform solution for several hours before the slow cooling process begins. As the temperature slowly cools, the amount of solute that can be held by the flux decreases, and the solution becomes supersaturated. At the supersaturation point, tiny crystals begin to form and become nucleation points for the crystal growth. As the temperature continues to decrease, additional atoms adhere to the forming crystals, leading to crystal that are large enough for scientific study. When the solution reaches a temperature that is just above the melting point of the flux, the furnace is either turned off or the flux is decanted. This step depends on the best way to remove the flux. If the crystal is not reactive or is harder than the flux, the flux material can be removed by chemical etching or mechanically. If the flux is not too viscous or the crystal is reactive, the flux can either be poured away or separated with a centrifuge.

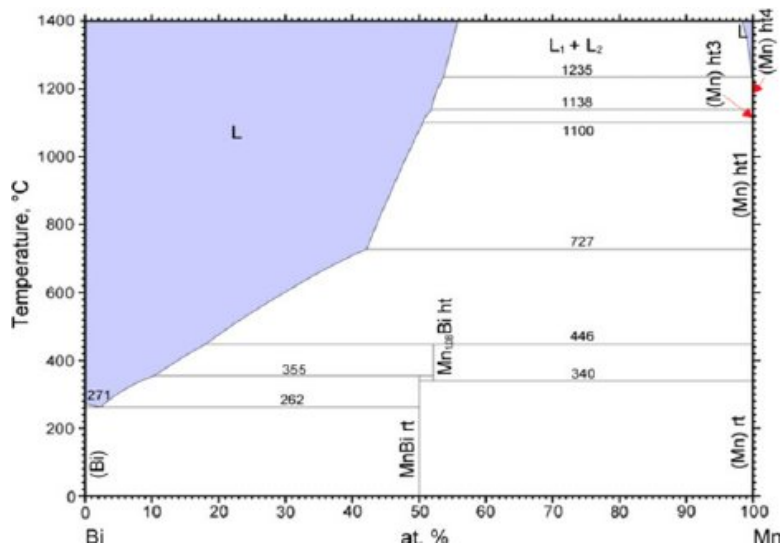


**Figure 5-9:** The Mn-Bi binary phase diagram[120] is used to find the liquidus temperature and decide on temperature for crystal growth.

The ideal flux for a given crystal system has a low melting point, is not too viscous, and either does not replace any of the atoms in the crystal or is one of the constituent elements of the crystal. In the case of NaMnBi, Bi is used as a self-flux. Bi is good for the flux of this system because it has a low melting point of 271° C, it is not viscous so can be poured off of the crystal, and has a fairly low liquidus temperature, as see in Fig. 5-9. The low liquidus temperature is important because at high temperatures the vapor pressure of Na will increase and interact with the silica ampoule. The molar ratio of the elements used was 1:1:6 for Na:Mn:Bi, using solid Na metal, polycrystalline Bi chunks, and Mn powder. The elements were placed in an alumina crucible to prevent the Na from interacting with the fused quartz. Mn powder was put in the crucible first, because it does not melt and gravity aids in keeping it in contact with the liquid. Na is next, as it has a melting point of 98° C and melts before the Bi. Finally, the Bi was used to fill the rest of the crucible. Quartz wool is placed on top of the filled crucible to allow Bi to flow past in the decanting step. The crucible is filled in an Ar atmosphere and sealed into a fused quartz ampoule. The liquidus temperature of the Mn-Bi binary, seen in the phase diagram in Fig. 5-9 is around 550 C for a 1:6 ratio, so the sample is heated to 600° C and held at that temperature for 12 hours. The ampoule is lowered in temperature

**Figure 5-10:** The Mn-Bi binary phase diagram[120] is used to find the liquidus temperature and decide on temperature for crystal growth.

to 300° C over 150 hours, when the crystal growth occurs. At 300° C, the ampoule is turned upside down to drain the excess Bi, and the ampoule is left at 300° C for 12 hours. After 12 hours the furnace cooled samples are allowed to cool as the furnace cools to room temperature, while some samples are quenched in liquid nitrogen. The resulting single crystals are between 0.1 and 0.5 cm and are shiny silver, as seen in Fig. 5-10. The crystals oxidize quickly and turn brown before disintegrating if left in the air.

# Chapter 6

# The CDW Transition in $TiSe_{2-x}Te_x$

In this chapter, the results of the neutron diffraction experiments are discussed in the context of the CDW transition in $TiSe_2$. For these experiments, Te is substitutionally doped into $TiSe_2$ to investigate the effect of doping on the CDW instability. $TiSe_2$ is a TMD that has been studied for its CDW order since the 1970s. Despite decades of research, the mechanism driving the CDW remains controversial. $TiSe_2$ is a semiconductor with a very small bandgap. $TiTe_2$, on the other hand, does not exhibit a CDW phase. Isovalent substitutional doping of $TiSe_2$ with Te can be used to shed light on the mechanism of the CDW. By doping with Te, the charge transfer from chalcogen to Ti is increased, inhomogeneity is introduced, and the lattice volume expands. By studying the local structure and CDW ordering of $TiSe_{2-x}Te_x$ as a function of temperature, the proposed processes driving the transition can be distinguished.

## 6.1 Evidence of CDW in $TiSe_2$

The CDW order in 1T-$TiSe_2$ was first reported in 1976 by Di Salvo[121]. Di Salvo noted an anomaly in the resistivity of $TiSe_2$ by measuring single crystals grown with chemical vapor transport at a range of temperatures. At around 200 K, the resistivity reaches a maximum before dropping sharply. Crystals grown with a lower growth temperature have a sharper peak in resistivity, while larger crystals can be

grown with a higher growth temperature.

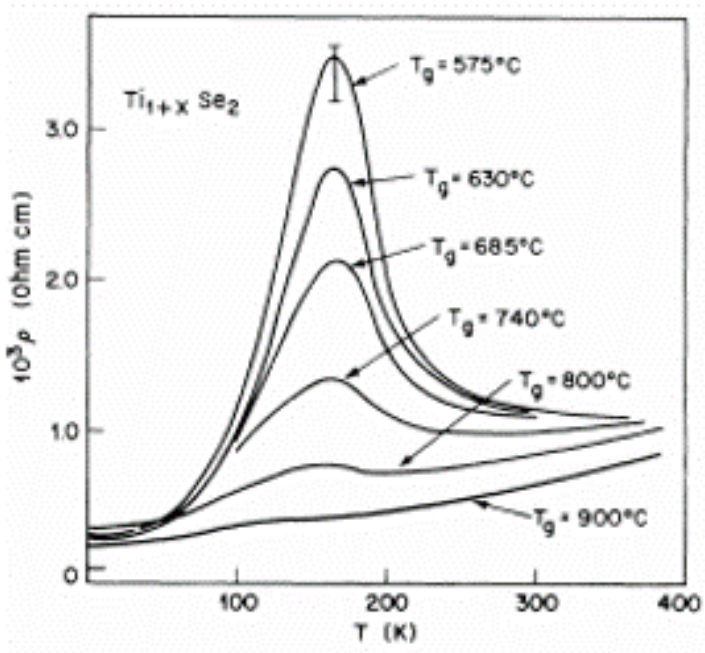


**Figure 6-1:** The resistivity anomaly in $TiSe_2$ is a sign of the CDW.[121]

To further investigate the resistivity anomaly, Di Salvo carried out neutron scattering experiments. The experiments revealed superlattice peaks with intensity on the order of 1% of the high temperature Bragg peaks that appear below 200 K, the same temperature as the resistivity anomaly. The superlattice peaks are indexed by a 2 x 2 x 2 periodic lattice distortion described by space group $P\overline{3}c1$. The charge density wave propagates with three q-vectors each with an associated displacement. The $\vec{q}$-vectors and their displacements are $\vec{q_1} = (0, \frac{1}{2}, \frac{1}{2})$ with displacement $\vec{d_1} = \epsilon_1(2, 1, z_1)$, $\vec{q_2} = (-\frac{1}{2}, \frac{1}{2}, 0)$ with $\vec{d_2} = \epsilon_2(1, 1, z_2)$ and $\vec{q_3} = (\frac{1}{2}, 0, \frac{1}{2})$ with $\vec{d_3} = \epsilon_3(-1, -2, z_3)$. The direction of the displacements associated with each vector is shown in Fig. 6-2. The total displacement for an atom located at $\vec{x_i}$ is given by:

$$\Sigma_i \vec{d_i} cos(\vec{q_i} \cdot \vec{x_i}) \tag{6.1}$$

The total displacement for the Di Salvo model is 0.042 ± 0.007 Å for Ti atoms and 0.014 ± 0.003 Å for Se atoms. The atomic coordinates for this model are listed

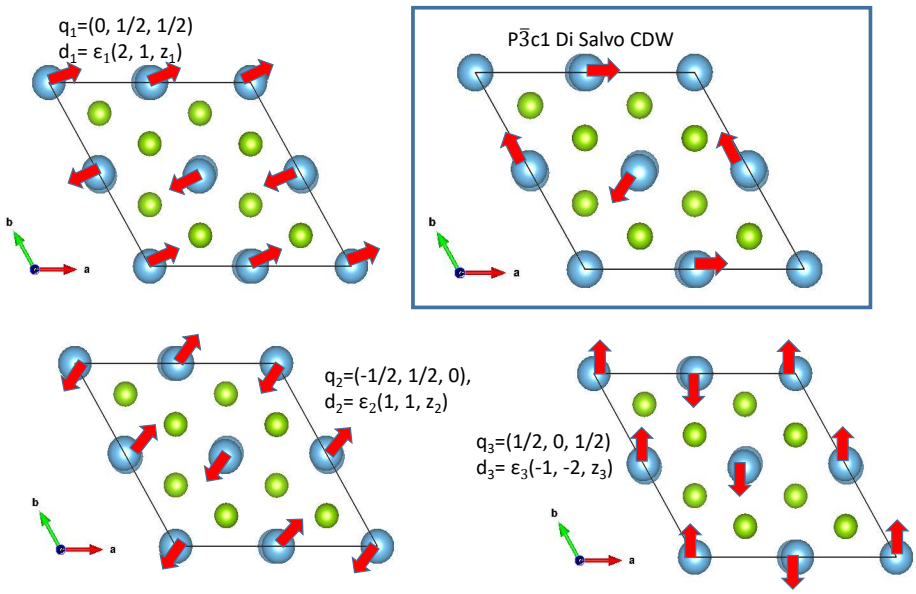


**Figure 6-2:** Each of the displacements associated with the three wavevectors are shown. The three displacements are added together to give the total periodic lattice distortion shown in the top right.

in the table below.

The Fermi surface of $TiSe_2$ consists of hole pockets of the Se 4p band at the $\Gamma$ point and electron pockets from the Ti 3d band at the $M$ point. When the charge density wave forms and the unit cell doubles, the reciprocal lattice vectors are reduced in half. As a result, the first Brilllouin Zone (BZ) is reduced and the $M$ points are mapped onto the $\Gamma$ points[122]. This causes a band folding that can be observed with angle resolved photoemission spectroscopy (ARPES) technique.

Table 6.1: The atom coordinates in the Di Salvo CDW model. The model has $P\overline{3}c1$ symmetry, a = b = 7.06 Å, and c = 11.99 Å.

| | x | y | z | Mult |
|---|---|---|---|---|
| Ti1 | 0 | 0 | 0 | 2 |
| Ti2 | 0 | 0.5012 | 0 | 4 |
| Se1 | $\frac{1}{3}$ | $\frac{2}{3}$ | 0.6298 | 4 |
| Se2 | 0.334 | 0.165 | 0.628 | 12 |

## 6.2 Reported Structure of $TiTe_2$

$TiTe_2$ is on the opposite end of the $TiSe_{2-x}Te_2$ doping spectrum from $TiSe_2$. Like $TiSe_2$, $TiTe_2$ crystallizes in the 1T polytype with space group $P\overline{3}m1$. Tellurium atoms are significantly larger than selenium atoms. As a result, the unit cell of $TiTe_2$ lattice has a significantly larger volume than that of $TiSe_2$. Despite the similarities, the physics of the two materials are different. $TiTe_2$ is a semimetal with a bandgap of 0.6 eV[123] and there is no observed periodic lattice distortion. It is not known why $TiTe_2$ does not have CDW phase. Possible explanations are the size of the cell inhibits the CDW formation or the larger bandgap prevents the periodic lattice distortion from forming due to increased d orbital occupation. For TiSeTe, the reported structure is the same as the 1T structure, with lattice parameters halfway between $TiSe_2$ and $TiTe_2$ and the Te and Se sharing a site. The study of the solid solution will show when the CDW goes away and how the Te affects the lattice with low concentrations.

Table 6.2: The lattice parameters and Se/Te z coordinate for $TiTe_2$ and TiSeTe.[124].

| | $TiTe_2$ | TiSeTe |
|---|---|---|
| a | 3.777 | 3.651 |
| c | 6.498 | 6.317 |
| z | 0.2628 | 0.2605 |

### 6.2.1 Proposed mechanism for the CDW in $TiSe_2$

The first proposed mechanism for the CDW was Fermi surface nesting, as it is the most common explanation for a 2D CDW. Studies of the Fermi surface show that the theory of Fermi surface nesting in $TiSe_2$[125] is irrelevant.

Excitons are bound states of electrons and holes. Excitons form in semiconductors with a gap that is small enough for thermal fluctuations to partially populate the conduction band, leading to an electron pocket and a hole pocket. If the binding energy for the excitons is larger than the gap, an exciton condensate[126] can form. In order for this to happen, the electrons and holes must coincide in momentum space, which requires a CDW modulation. An analysis of the ARPES spectrum of $TiSe_2$ demonstrated that the spectral weight of the backfolded bands was too large to be due to the lattice distortions but can be explained by a BCS-like exciton model[122].

Despite the observation of excitons in $TiSe_2$, they alone cannot account for the transition. The excitonic excitations can be suppresed using infrared femtosecond pulses. It has been demonstrated that even when the excitons are destroyed the periodic lattice distortion and CDW energy gap remains in the system[127]. Although electron-hole interactions may play some role in the CDW formation, electron-phonon interactions in the form of a JT-like mechanism are also necessary to account for the CDW.

### Jahn-Teller Effect

The classic JT effect is a phenomenon that occurs in compounds that consist of partially occupied degenerate d-bands. In the JT-effect, ligands in high symmetry positions about the transition metal distort in order to lower the Coulomb potential between the electrons and the ligands. For example, the d-orbitals in an octahedrally coordinated system separate into two-fold degenerate $e_g$ and three-fold degenerate $t_{2g}$ bands. In this symmetry, if the $t_{2g}$ orbitals were unevenly filled, there would be a degeneracy in which of the three orbitals would be occupied. If, on the other hand, the bond length along the z-axis increases due to Coulomb repulsion, the $d_{xz}$ and $d_{yz}$ orbitals are lowered in energy. This is the cause of spontaneous symmetry breaking in JT systems.

There have been two JT mechanisms proposed for $TiSe_2$, by Hughes[128] and Whangbo[129]. Unlike the JT distortion described above, the two mechanisms do not lead to splitting of the d-orbitals, as the octahedrons surrounding the Ti atoms are

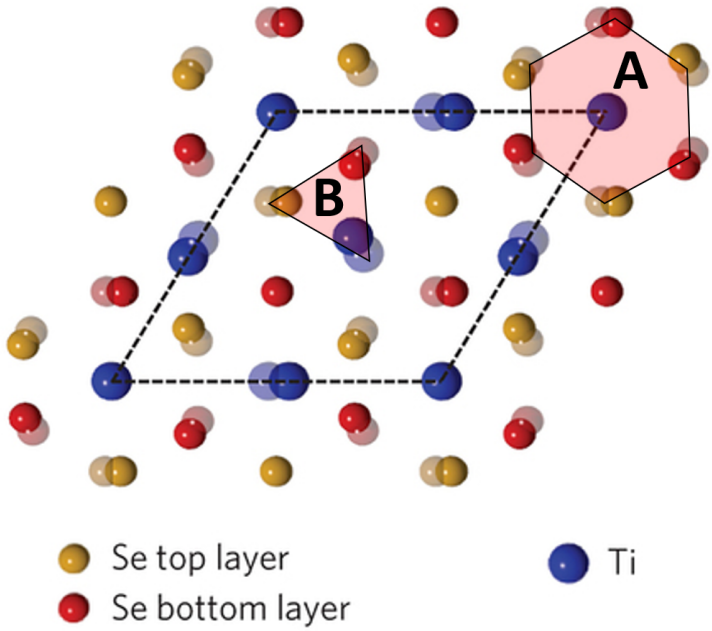


**Figure 6-3:** The two Ti sites are the A site at (0,0,0) and B site at (0.5 0.5 0).

already compressed in the high temperature phase. The mechansims are called JT-like because the distortions change the energy of the bands relative to each other based on Coulomb interactions. The two JT mechanisms differ in which $TiSe_6$ octahedrons are driving the periodic lattice distortion. As shown in Fig. 6-3, the Di Salvo model leads to two distinct Ti sites in the unit cell. The A site, located at (0,0,0), is surrounded by Se that rotate about the c-axis. The bond lengths of these Ti-Se pairs remains constant and the only difference is the relative orientation of the upper and lower Se triangle. At the B site, the Ti and Se atoms move slightly toward a shared center. This lowers the bond lengths in this $TiSe_2$ trimer by 0.05 Å.

### Hughes Pseudo Jahn-Teller

The first JT model, called the pseudo Jahn-Teller effect (PJT) was proposed by Hughes and is related to the A site of Ti[128]. In both the 1T and 2H configuration, the $t_{2g}$ band is split into an $e_g$ and $A_1$ band. In the octahedral coordination, these bands lie very close to each other, however in the trigonal prismatic coordination the lowest d band is lowered significantly, as seen in Fig. 6-4. The rotational distortions

at the Ti-A site give a structure that is close to the 1T phase but rotated to a structure intermediate between the 1T and 2H, which could lead to a slight lowering of the Ti d-band. In order for the PJT explanation to be true, it follows that the d-band must be at least partially occupied.

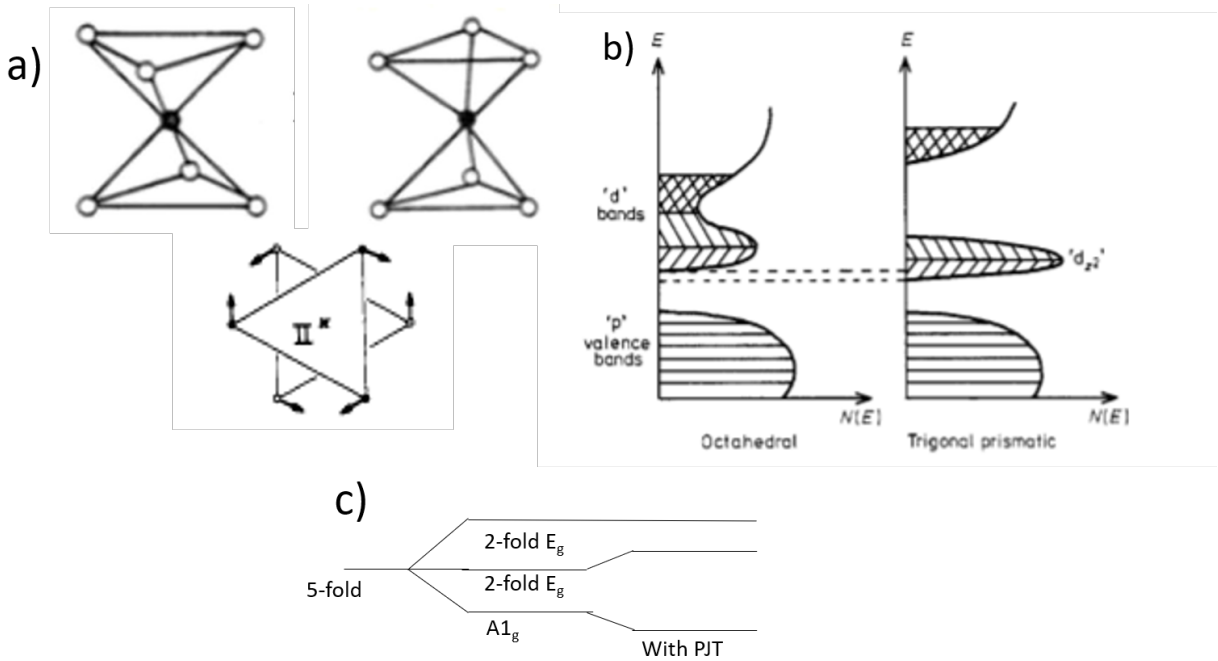


**Figure 6-4:** (a) In the Hughes model, the Ti coordination is intermediate between the 1T and 2H polytypes. (b) This would lower the d band of Ti, causing the CDW. [128](c) The d-band of $TiSe_2$ as it goes from spherical symmetry to non-CDW to CDW phase.

### Whangbo Band Jahn-Teller

The other JT model is the band Jahn-Teller model (BJT). This model, introduced by Whangbo and Canadell, relies on the B site Ti and the p-band of the Se[129]. In this mechanism, shortening of the bonds between Ti-Se atoms leads to a hybridization of the Se p and Ti d orbitals, as seen in Fig. 6-5. This has the effect of lowering the p-band and raising the d-band. In order for this to be energetically favorable, a significant bond shortening must occur and there may not be occupancy of the d-orbital. To distinguish between the two JT explanations, it is important to investigate the bond shortening of the TI-Se bonds by looking at the local structure and to see the effects of increasing charge transfer to the d-orbital by doping Te to the system.

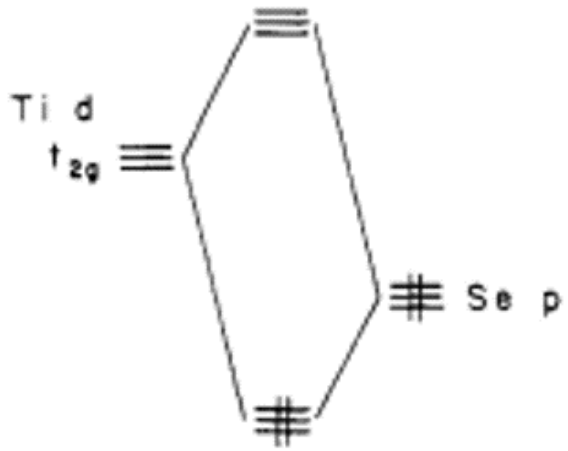


**Figure 6-5:** In Whangbo and Canadell's Jahn-Teller model, hybridization between the Ti d and Se p lowers the p band and causes the CDW.[129]

## 6.3 Average Structure of $TiSe_2$

In order to study the mechanism driving the CDW transition in $TiSe_2$, the solid solution of TiSeTe is measured with constant wavelength neutron scattering. The constant wavelength diffraction can be used to create a phase diagram for the doping series. $TiSe_2$ was measured at BT-1 at 4 K, 100 K, and 300 K. Fig. 6-6 shows the neutron diffraction pattern of $TiSe_2$ at 7 K fit with the $P\bar{3}c1$ CDW symmetry. The $\chi^2$ for this fit is 3.57. The periodic lattice distortion that accompanies the CDW is very subtle and the large peaks are indexed by the high temperature undistorted phase with lattice constants a = b = 3.537 ± 0.003 Å and c = 6.00 ± 0.030 Å [130] and the only temperature dependence of these peaks is due to lattice thermal expansion of the lattice. Small Bragg peaks with half-integer indices are observed below 200 K, a signature of the superlattice formation. Fig. 6-7 shows the diffraction pattern zoomed in to the proximity of the (1/2, 0, 4) superlattice peak to show the temperature dependence of the peak in the undoped system. This particular peak is chosen because the superlattice peaks are similar in intensity to the peaks from unreacted Ti, Se, and Te and the (1/2, 0, 4) peak does not overlap in d-spacing with any of the peaks from those phases. The peak has an intensity on the order of 1% of the peaks in the high temperature phase, which agrees with previous single crystal

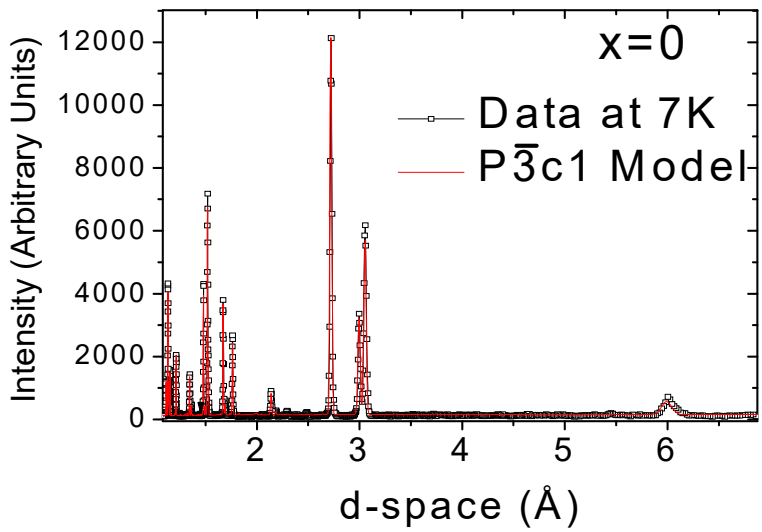


**Figure 6-6:** The main Bragg peaks are fit well by the published $P\bar{3}c1$ symmetry.

diffraction experiments[121]. The $\chi^2$ for the 100 K data fit with the $P\bar{3}c1$ model and the 300 K data fit with the undistorted $P\bar{3}m1$ model are 3.49, and 4.43, respectively. The temperature dependence of the peak confirms the existence of the 2 x 2 x 2 superlattice and can be compared to the doping series.

Although the $P\bar{3}c1$ superlattice fits the data well, this symmetry is does not uniquely index the superlattice peaks and another space group with the same 2 x 2 x 2 lattice expansion but different periodic lattice distortion can equally successfully reproduce the peaks. For the Di Salvo structure described above, the periodic lattice distortion consists of a rotational distortion and displacements of $0.014 \pm 0.003$ Å and $0.042 \pm 0.007$ Å of the Se and Ti atoms, respectively, around the Star of David motif. The result of the distortion is the creation of $TiSe_2$ trimers with slightly shortened bonds [121] at the Ti-A site, while creating a coordination intermediate between the 1T and 2H phases at the Ti-B site. A superlattice with symmetry from space group $P\bar{3}m1$ fits the diffraction pattern equally well. Fig. 6-8 shows a comparison of the two Ti distortion patterns with the fits of the data. The $P\bar{3}m1$ periodic lattice distortion consists of a breathing mode distortion. Fig. 6-9 shows that the

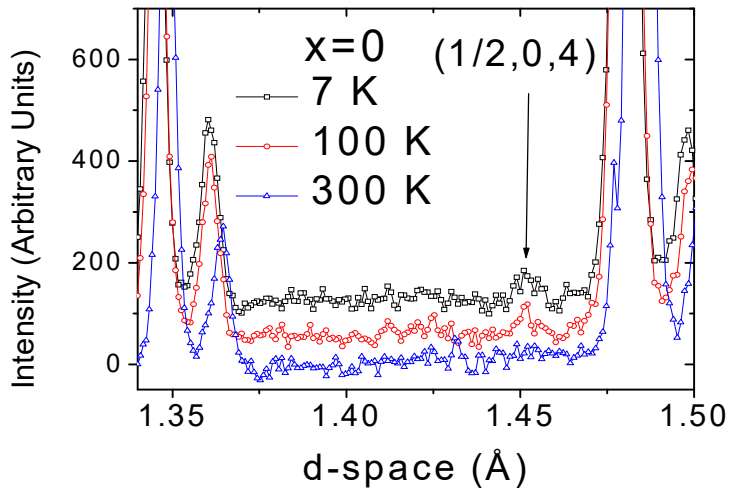


**Figure 6-7:** The temperature dependent neutron scattering shows the formation of the CDW in $TiSe_2$.

$\vec{q}$-vectors of this periodic lattice distortion are the same as the $\vec{q}$-vectors in the Di Salvo model. Fig. 6-10 shows the distortion pattern of all atoms with four unit cells plotted. As both periodic lattice distortion motifs have the same dimensions and the distortions are very small, the symmetry cannot be determined through the average structure analysis alone. We next use local structure analysis to further investigate the structure.

## 6.4 Local Structure of $TiSe_2$

With identical unit cell volume, CDW propagation vectors, and atomic positions within 0.1 Å of each other, the differences between the two CDW models is subtle, but is important for understanding the mechanism of the phase transition. Experiments investigating the local structure of $TiSe_{2-x}Te_x$ were carried out at NOMAD. Samples with x = 0, 0.025, 0.05, 0.1, 1, and 2 were measured at temperatures 7 K, 50K, 100 K, 150 K, 165-210 K in steps of 5 K, 220 K, 240 K, 260 K, 280 K, and 300 K. The temperature range was chosen in order to see the full CDW transition. Based on the

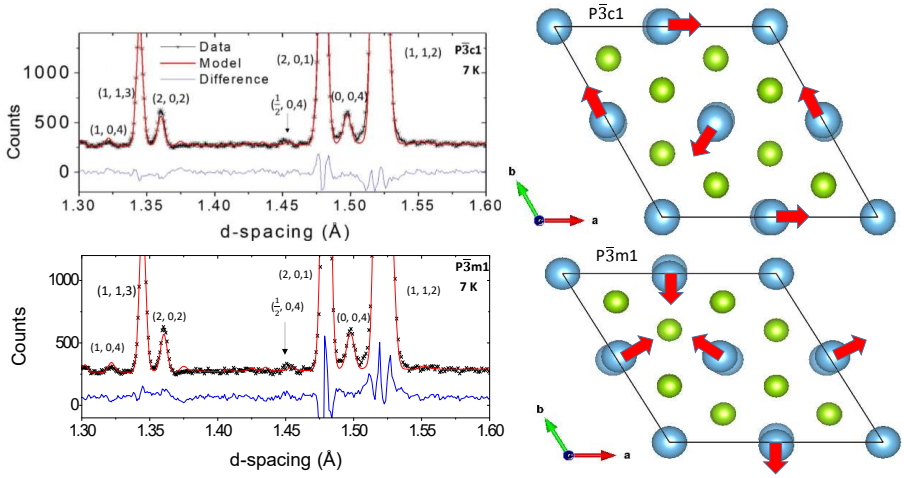


**Figure 6-8:** Two different structural models are able to fit the average structure equally well.

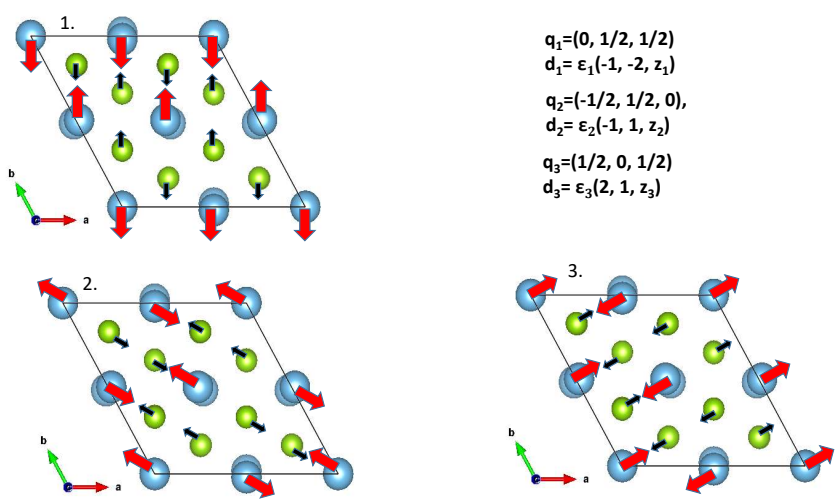


**Figure 6-9:** The vectors in the $P\bar{3}m1$ model are the same as those of the Di Salvo model, but the associated distortions are different.

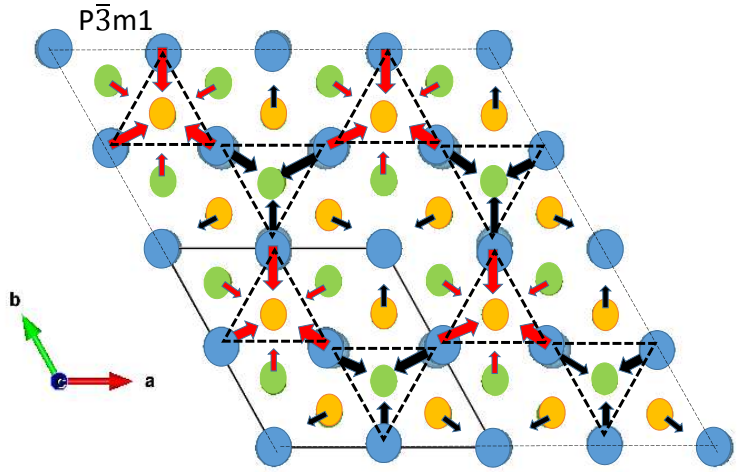


**Figure 6-10:** The full distortion pattern of the $P\bar{3}m1$ CDW model. Ti atoms are in blue, lower layer Se atoms are in green, and upper layer Se atoms are in yellow. The Ti distortions form a breathing pattern about the Se atoms.

Di Salvo model, it is expected that all of the nearest neighbor Ti-Se peaks are the same length above the CDW transition and that there is a slight asymmetry to the peaks as some of the peaks become slightly shorter below the CDW transition. Fig. 6-11 shows the PDF of $TiSe^2$ at (b) 2 K and (b) 300 K. The G(r) at 2 K is fit with the breathing model in red and the Di Salvo model in blue. After the fist peak, both models fit the data equally well. For the first peak, there is a clear splitting of the Ti-Se bond. The negative Ti-Se correlation peak at 2.55 Å has a shoulder to the left at 2.41 Å. The magnitude of the split is much larger than the shortened bond of 2.49 Å predicted by the Di Salvo model. The breathing model fits the distortion well, as seen in the inset. This is because when the symmetry constraints are relaxed to $P\bar{3}m1$, the constraints of the atom displacements are lifted and the Ti atoms are no longer constrained to move along the **a** or **b** axis toward another Ti atom as in the $P\bar{3}c1$ symmetry, where **a** and **b** are the lattice vectors of the primitive hexagonal unit cell. With $P\bar{3}m1$ symmetry, Ti atoms move toward Se atoms This breathing distortion shortens the bonds of $\frac{1}{8}$ Ti-Se nearest neighbor bonds as six of the eight Ti

atoms in the unit cell move toward one of their six neighbors.

At 300 K, the splitting of the first peak persists despite no CDW being observed. Additionally, the long range correlations of the PDF cannot be fit with the hexagonal symmetry $P\bar{3}m1$ despite the good fit of the average structure using this symmetry. A local monoclinic model improves the fit as shown in Fig. 6-11(b). At long distances of r > 9 Å above $T_{CDW}$, peaks corresponding to correlations two unit cells away split into separate distinct peaks (see inset of Fig. 6-11(b) and Fig. 6-12. The space group of the monoclinic model is P2/m. As Se has a much larger scattering length than Ti, the peak at 9.34 Å is primarily composed of Se-Se correlations. The correlations are made up of Se atoms that are separated by a translation of $2\mathbf{a} - \mathbf{b}$ and all symmetry equivalents. Fig. 4(d) shows two of the correlations that split due to the high temperature monoclinic distortion that breaks the a = b symmetry. The monoclinic distorion is slight and is on average the same as the 1-T phase.

## 6.5 Average Structure of $TiSe_{2-x}Te_x$

The effects of doping with Te on the CDW transition were investigated using neutron scattering. Samples with x = 0.025, 0.05, 0.1, 0.15, 0.2, 0.25, 0.3, 1, and 2 were measured at BT-1, HB2-a, or NOMAD. The samples were measured at a wide range of temperatures.

$TiTe_2$ is on the other end of the doping spectrum and is not reported to undergo a CDW transition. Fig. 6-13 confirms that no CDW transition occurs between T = 7 K and T = 300 K. Scans for the solid solution series can be used to find the concentration a which the CDW is suppressed. The highest concentration of Te for which the CDW transition is observed is x = 0.2, with no transition occuring in x = 0.25, as seen in Fig. 6-14. For the sample with nominal doping of x = 1, the CDW does not appear, as expected. However, with the high inhomogeneity introduced in TiSeTe, the hexagonal model with $P\bar{3}m1$ symmetry no longer fits. At low d-spacing, the peaks gain a shoulder that is indicative of a monoclinic distortion. Although these peaks are doubled, it is clear that the sample is a single phase and not a combination

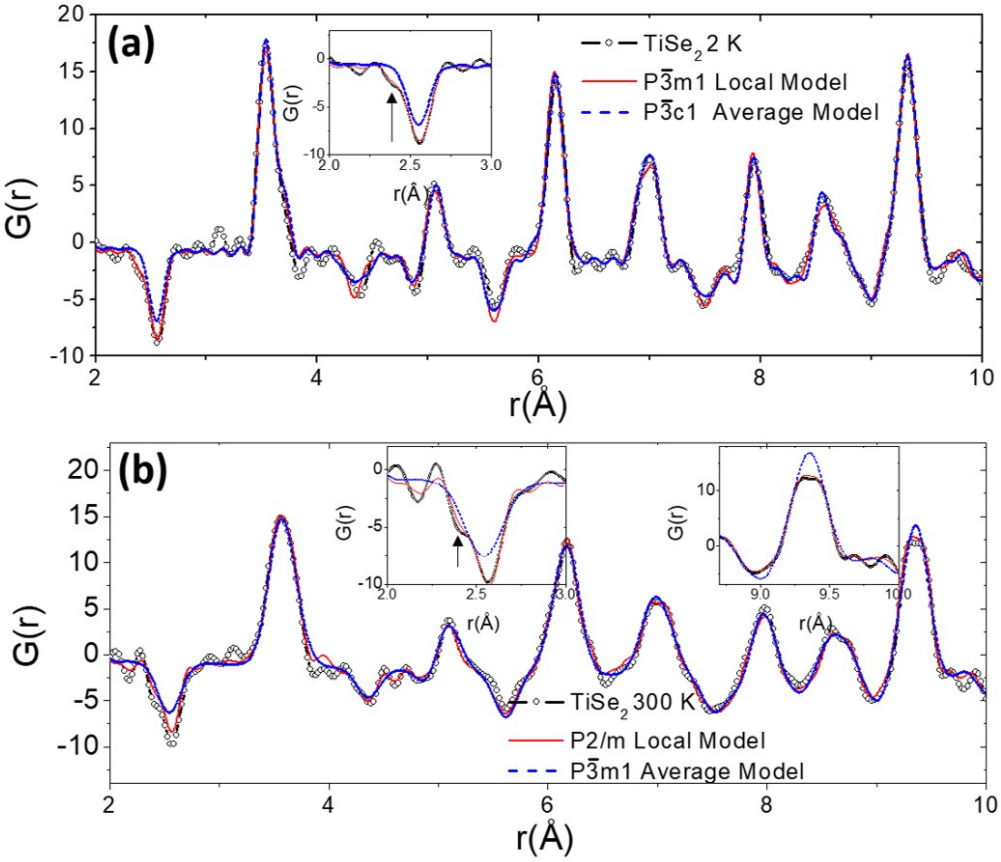


**Figure 6-11:** (a) The local structure of $TiSe_2$ in the low temperature CDW phase is fit with the previously reported P$\bar{3}$c1 model and with a P$\bar{3}$m1 model. Both fit long range correlations well but only the P$\bar{3}$m1 model can reproduce splitting of the first peak. (b) The high temperature phase local structure is fit with the hexagonal average structure and with a monoclinic model. Only the monoclinic model can reproduce correlations above 9 Å[131].

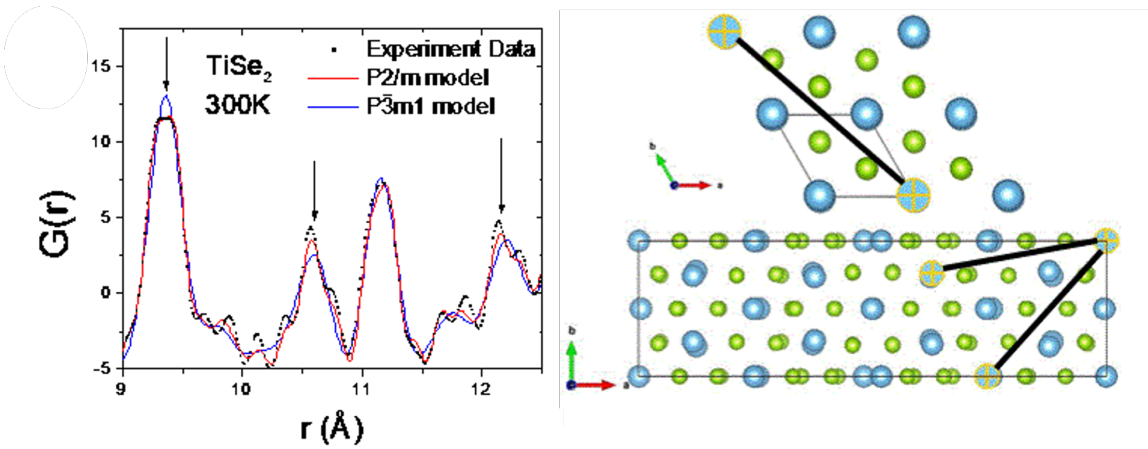


**Figure 6-12:** Above the CDW transition, the hexagonal unit cell does not fit peaks above 9 Å. The peak at 9.3 Å is highlighted in the hexagonal and monoclinic cell on the right. The peaks symmetry equivalent peaks are all the same length in the hexagonal cell but split in the monoclinic cell.

of $TiSe_2$ and $TiTe_2$ because the separation between peaks at high d-spacing are at shifted significantly between the two phases but are at an intermediate location in TiSeTe. The diffraction patterns for x = 1 can be fit using the symmetry P2/m with $\chi^2 = 4.881$. Refinement of occupancy of Se and Te suggests that the stoichiometry is closer to x = .6, although the unit cell volume agrees with the literature[124]. The result that Te doping suppresses the phase transistion is not particularly surprising, however the phase diagram and interactions can give insight into the mechanism of the transition. The CDW is suppressed monotonically as Te enters the lattice. Also introduced by Te are additional transfer to the d band, inhomogeneity, and a monotonic expansion of the cell volume. From average structure alone it is difficult to say which is the most important for the transition. See how the local structure changes through the transistion is important for the CDW mechanism.

## 6.6 Local Structure of $TiSe_{2-x}Te_x$

The local effects of doping as the CDW is suppresed were investigated using PDF analysis. As Te is doped into the system, the splitting of the first peak remains unchanged s seen in Fig. 6-15. For x $\leq$ 0.1 the shoulder at 2.41 has the same

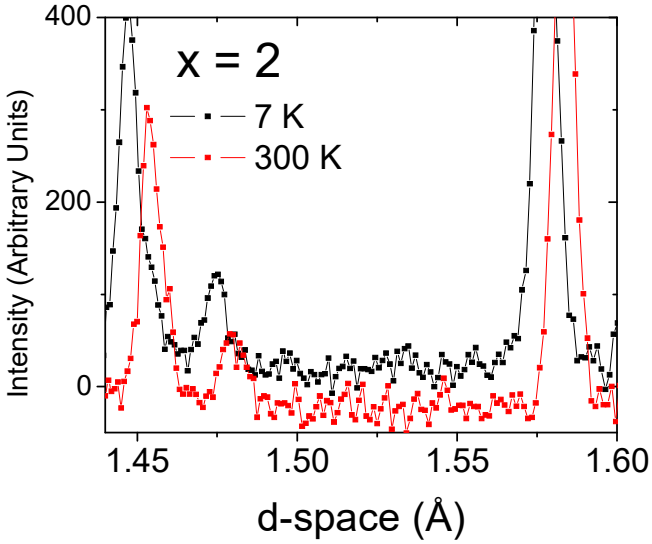


**Figure 6-13:** Temperature dependent neutron scattering on $TiTe_2$ shows that no superlattice transition occurs.

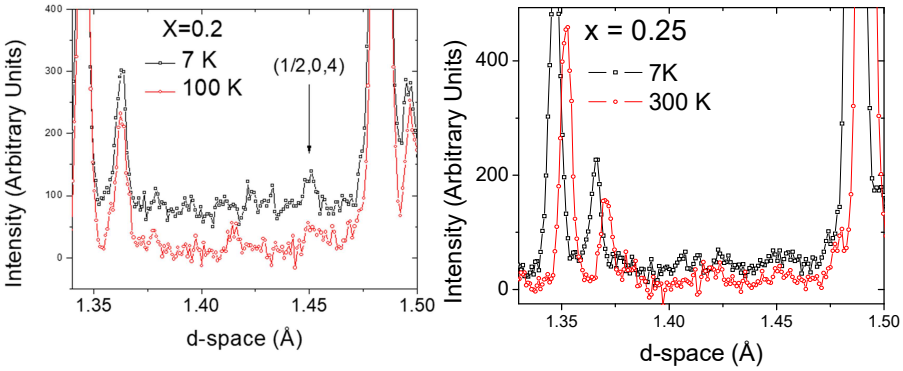


**Figure 6-14:** The CDW peak disappears between 7 and 100 K for x = 0.2 and does not appear at any temperature in x = 0.25.

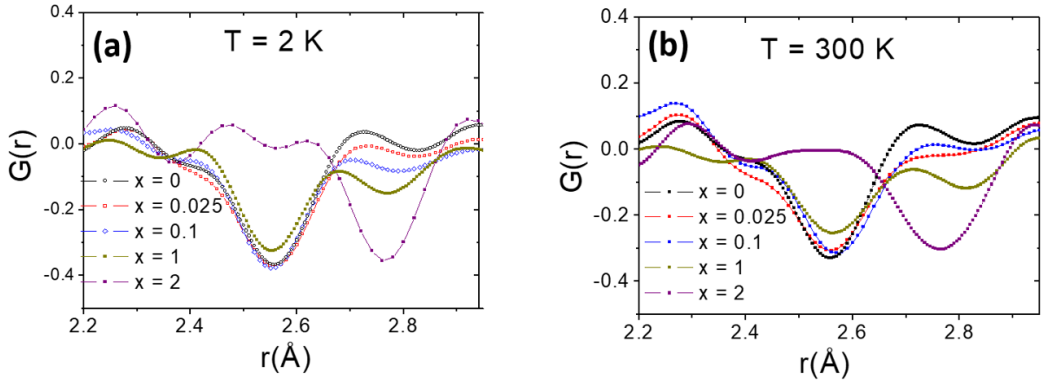


**Figure 6-15:** (a) The Ti-Se peak at 2 K is split for all doping levels with a CDW transition. As Te is doped into the system a separate Ti-Te peak appears and the splitting of the Ti-Se peaks vanishes when no CDW occurs[131].

magnitude as in $TiSe_2$. For x = 0.1 a second peak begins to appear at x = 2.79 Å and the intensity of the x = 2.55 peak decreases slightly. The peak at 2.79 Å occurs in the same place as the first nearest neighbor Ti-Te peak in $TiTe_2$. For the peaks, for x $\leq$ 0.1 the splitting persists above the CDW transition, just as in $TiSe_2$. The temperature of the monoclinic distortion decreases with Te doping. In these samples that exhibit the CDW, the Ti-Se bond shortening occurs in all compositions. While the total intensity of the Ti-Se peak decreases as the ratio of Se:Te decreases, the ration of the short to long peaks stays the same. For all of these samples, $\frac{1}{8}$ of the Ti-Se bonds are shortened, just as in the $TiSe_2$. Above the transition temperature, the ratio of short to long bonds stays the same, but the thermal broadening of the peaks makes the short peak more pronounced in the pattern.

For x = 1 and x = 2 the Ti-Se and Ti-Te peaks are symmetric and there is no evidence of shortened bonds. It is important to note that even the Ti-Se bond of the TiSeTe structure is not split. For x = 1 the intensity of the Ti-Te peak has increased and the integrated intensity of the peaks suggests that x is closer to 0.65. The G(r) of the x = 1 sample fits the monoclinic phase with a = 25.004 $\pm$ 0.011 Å b = 11.0072 $\pm$ 0.0041 Å c = 12.6097 $\pm$ 0.0071 Å $\beta$ = 88.752 $\pm$ 0.057 observed in the average structure. The low r portion of the G(r) is shown with the P2/m and TiSeTe structure of Arnaud[124]. With x = 2, the local structure is monoclinic at all temperatures, as seen in Fig. 6-17.

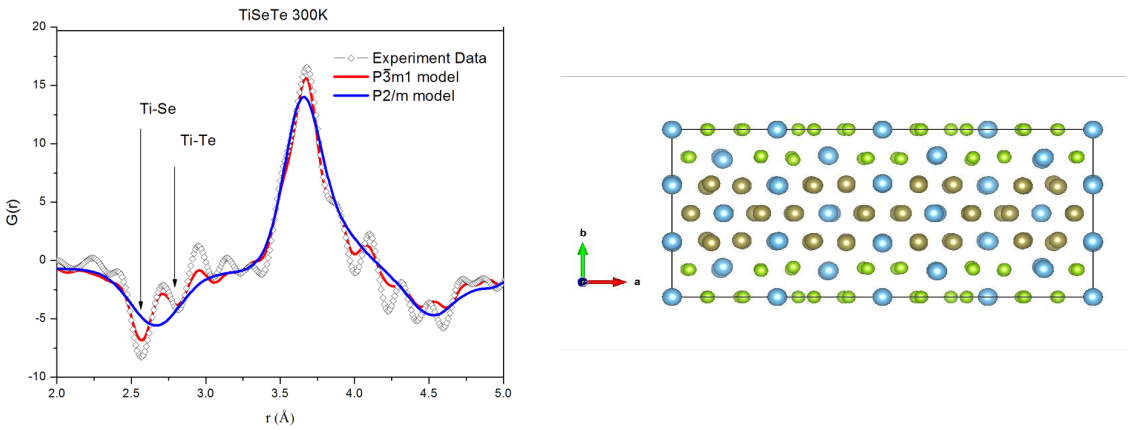


**Figure 6-16:** The local structure of TiSeTe shows that there are distinct Ti-Se and Ti-Te peaks and is fit by a monoclinic unit cell, shown on the right. The structure is best fit when Te and Se are separated and not randomly distributed.

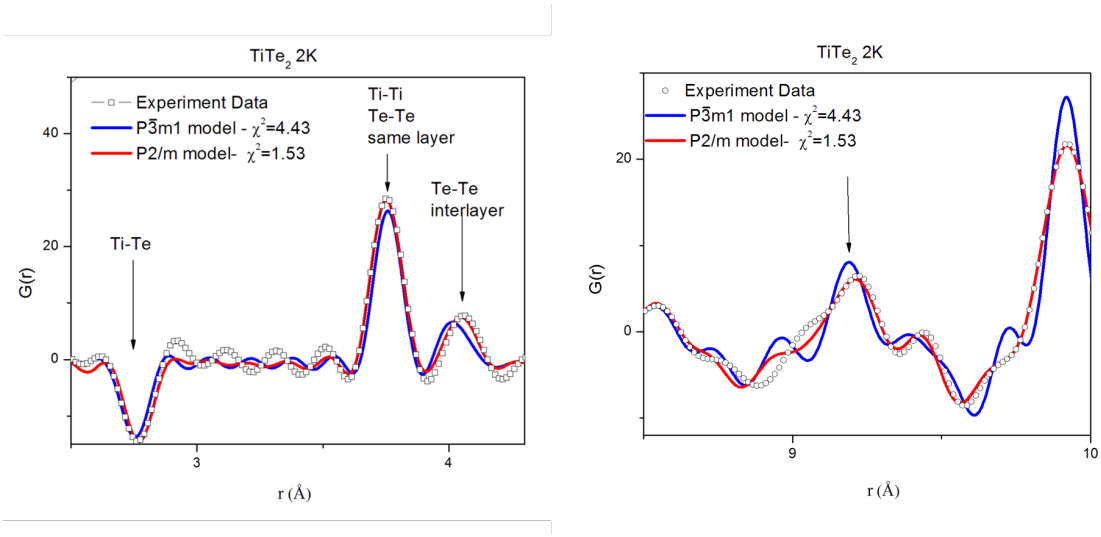


**Figure 6-17:** The local structure of $TiTe_2$ is plotted with a hexagonal and monoclinic symmetry. The monoclinic unit cell fits the local structure better.

The results indicate that the JT distortion exists above $T_{CDW}$ and becomes cooperative when the CDW forms. This model retains the breathing mode distortions with the same bond lengths as the CDW phase while breaking the overall local trigonal symmetry.

## 6.7 Discussion

Based on the presence of superlattice peaks in the constant wavelength diffraction data, the hexagonal to monoclinic distortions in the PDF, and the presence of the peak splitting, a phase diagram for $TiSe_{2-x}Te_x$ is created. The composition dependence of the CDW order is shown in the phase diagram of Fig. 6-18. It is clear that as Te is doped into the system, the CDW transition is suppressed. For x = 0.025, $T_{CDW}$ is between 150 and 190 K. For x = 0.1 transition occurs between 100 and 150 K. From the presence of superlattice peaks, the highest doping level to undergo the CDW transtion is x = 0.2 while the absence of superlattice reflections in x = 0.25 and x = 0.3 correspond to the absence of the CDW order.

Splitting of the first Ti-Se peak is observed in the local structure for samples with a CDW phase. This splitting does not occur when the concentration of Te is high enough that the CDW is suppressed. As this splitting occurs even at high temperatures, well above the $T_{CDW}$, there is a clear connection between the distortions and CDW formation. The magnitude of the Ti-Se distortion and the percentage of bonds distorted remains constant for small x despite a decrease in $T_{CDW}$. It is likely that competition between disorder introduced by Te and tendency toward a long range cooperative JT order with Se leads to a lowering of the transition temperature.

As discussed at the beginning of this chapter, multiple models that consider a JT mechansim have been proposed for the $TiSe_2$ system. The model proposed by Hughes[128], for instance, suggests that the energy of a partially occupied $d_{z^2}$ band is lower in a trigonal prismatic 2-H crystal field than in an octahedral 1-T field. In this model, the rotational modes of B-site Se about Ti leads to a configuration intermediate between the 2-H and 1-T polytypes.

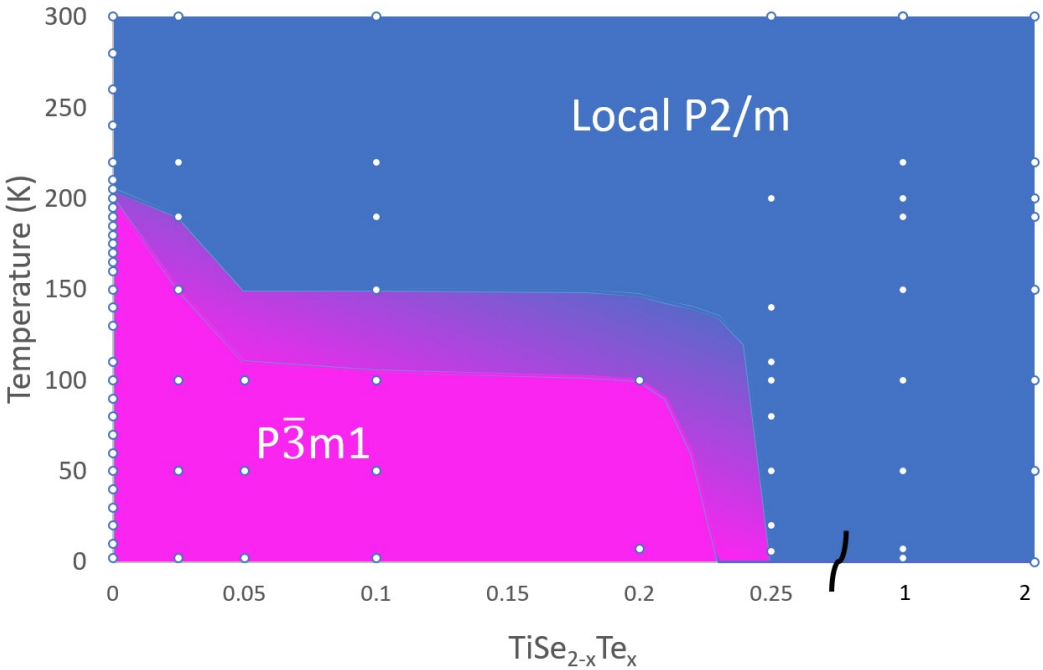


**Figure 6-18:** Phase diagram for the $TiSe_{2-x}Te_x$ system. The CDW transition is suppressed with Te doping and does not appear above a Te concentration of 12.5%.[131]

The d electron occupancy of $TiSe_2$ is quite small and close to $d^0$ while the count in $TiTe_2$ is closer to $d^{\frac{1}{3}}$ as the size of Te atoms leads to greater chalcogen to transition metal charge transfer[129]. The Hughes model suggests an increase in charge transfer with Te doping initially leading to a more robust CDW. The suppression of the CDW with doping combined with no observation of the rotational modes in the local structure makes the Hughes mechanism unlikely.

The Whangbo[129] model, on the other hand, requires a JT driven CDW transition to shorten the Ti-Se bond length. This reduces the energy by delocalizing electrons and allows for hybridization between the Ti 3d and Se 4p orbitals. In this model, the p band is lowered and the transition does not rely on chalcogen to Ti charge transfer.

The Whangbo model can account for the dependence of the transition on Te doping. Consistent with our measurements, the CDW phase is suppressed when Te is

substituted into the lattice. Te disrupts the electronic homogeneity of the crystal and inhibits the cooperative JT observed in pure $TiSe_2$. A possible explanation for this is that Te orbitals are more diffuse[129] and Te atoms are heavier than Se, the energy gained through orbital overlap is diminished on the Ti-Te sites. As the Te electrons are more mobile, this may increase charge transfer to Ti d bands as the reduced p occupancy of the chalcogen sites leads to a weaker interaction.

Further evidence that would support that charge transfer suppresses the CDW comes from the monoclinic distortion above $T_{CDW}$. It is unusual for a high temperature phase to have lower symmetry than the low temperature phase. Despite this, the local structure analysis suggests that there is a monoclinic distortion of the local structure. $CrSe_2$ is a material that undergoes a similar phase transition[132]. $CrSe_2$ has a low temperature trigonal symmetry ($P\bar{3}m1$) with a monoclinic intermediate phase (I2/m) that is caused by charge transfer to Cr leading to a degeneracy in the $t_{2g}$ band that breaks the threefold rotation symmetry. In $TiSe_{2\text{-}x}Te_x$ this monoclinic distortion breaks up the long range order associated with the CDW. At low temperatures a cooperative JT effect drives orbital ordering that leads to a CDW phase. As the temperature increases above $T_{CDW}$, thermal fluctuations could lead to charge transfer to the d electrons of Ti. A degeneracy in the $t_{2g}$ band of Ti can break the local $C_3$ symmetry while preserving the short range distortions, as observed in the local structure.

# Chapter 7

# Extreme Magnetoresistance in NaMnBi

## 7.1 I-Mn-V Antiferromagnets

As discussed in Chapter 4, AFM materials are a promising class of materials for spintronics devices, but there are challenges to replacing FMs in devices. The realization that AFM dynamics can be useful for spintronic device applications motivates the present direction of the field and leads to an effort to find useful properties of AFM semiconductors.

One class of AFMs is the I-Mn-V semiconductors. The materials are made up of an alkali metal (Li, Na, K, Rb, Cs), Mn, and a pnictogen element (P, Sb, As, Bi). Cu is also included with the alkali metals, as it has a tendency to ionize with a 1+ oxidation state and can be stabilized into the same structure as the other materials in the group. They are layered materials that can be easily cleaved, with weak bonds between the alkali layers. The lattice symmetry of this class of materials is P4/nmm. The Mn atoms are tetrahedrally coordinated by the pnictogen, with alkaline ions between the Mn-pnictogen layers.

In this system, the Mn carries the magnetic moment and the magnetic ordering is AFM. There are two different AFM configurations in the system. For all Na containing compounds and KMnBi and KMnSb, the AFM is C-type, while for KMnP,

KMnAs, and all Rb and Cs containing compounds the AFM order is G-type[133, 134]. The magnetic ordering depends on the ratio of the c and a lattice parameters. For $\frac{c}{a} \leq 1.76$ the magnetic unit cell is C-type, but if $\frac{c}{a} > 1.76$ it is G-type, as shown in Fig. 7-1. There is also a dependence of the magnetic moment on the pnictogen atom. For all alkali atoms, the moment of the Mn atom increases when moving down group V. For example, NaMnBi has a moment of $4.5\mu_B$ while NaMnP only has a moment of $3.63\mu_B$. Moving down the periodic table also increases the cell volume because the lattice is made up of larger atoms.

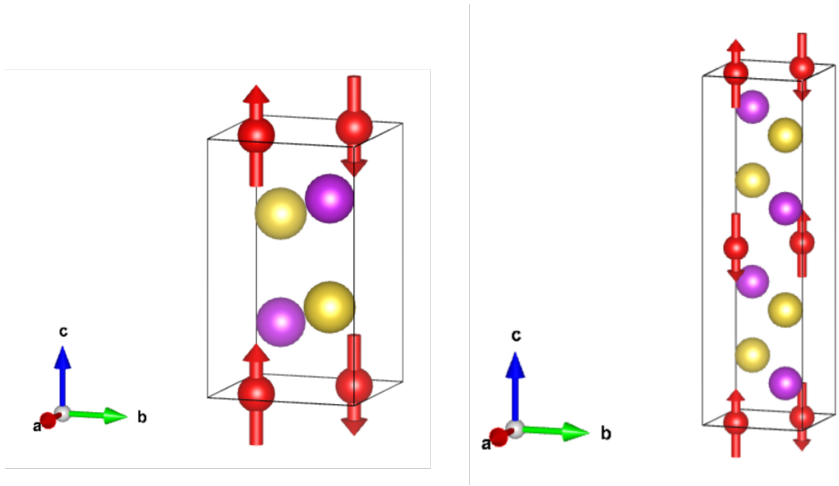


**Figure 7-1:** The magnetic structure of I-Mn-V compounds with a small c:a ration (left) and with a larger c/a ratio (right).

To date, these systems have had few studies performed on them. The most commonly studied members of this class are CuMnAs and LiMnAs, which will be discussed in this section. I-Mn-V semiconductors are challenging to grow and work with, as the crystals are air sensitive. The I-Mn-V AFM compounds are good candidates for spintronic applications because they have a high Néel temperature above room temperature and can be easily cleaved, and that can be made compatible with tetragonal substrates[135].

### LiMnAs

Among the most studied I-Mn-V materials is LiMnAs. LiMnAs has a Néel temperature at 373 K and a structural phase transition from hexagonal to cubic at 768

K. It is a semiconductor[136]. LiMnAs has a notable resistivity as the resistivity decreases by five orders of magnitude between 100 K and 300 K[137]. LiMnAs is also notable as the first material in the I-Mn-V class to be lattice matched and deposited onto an InAs substrate with epitaxy. This is an important feature as it means that the I-Mn-V materials are likely to be compatible with existing technology and makes device fabrication feasible. First principles calculations have shown that LiMnAs has high anisotropy effects, making it interesting for spintronic applications[138].

#### CuMnAs

Although the ground state of CuMnAs is orthorhombic, CuMnAs can be stabilized in a tetragonal phase by growing on GaAs substrate[139]. The tetragonal phase has the same P4/nmm space group as the other I-Mn-V compounds, but the Mn is switched with Cu in the layered structure. The AFM transition occurs above room temperature with the spins oriented in the a-b plane rather than along the c-axis. Calculations for CuMnAs tunnel junctions demonstrate that the material is a good candidate for spintronic devices, as the devices have strong spin-transfer torque due to the broken inversion symmetry of the system[140]. CuMnAs has been used to demonstrate switching caused by a pulsed current with writing pulses that can be used to rewrite the bit over a hundred times without degradation[141].

## 7.2 Electronic Characterization of NaMnBi

NaMnBi is an interesting material to study because it is an AFM semiconductor and similar materials have been demonstrated to exhibit spin orbit torque. New room temperature AFM materials are needed to replace FM electrodes in devices such as read heads and MRAM[142, 98]. AFMs are resilient to external perturbations and do not create stray fields. This makes them promising for ultrafast, high density storage devices[143]. FM devices exhibiting GMR are limited by low Curie temperatures, with recent discoveries finding a maximum Curie temperature of 230 K[144, 145, 146, 147]. GMR also relies on layered heterostrucutres and AFM materials could replace them

with a single material[148, 149]. Tunneling devices using IrMn heterostructures give large magnetoresistive signals but do not exist in a single phase.

An advantage of NaMnBi is that large bulk single crystals can be synthesized. AFM NaMnBi has a tetragonal crystal structure, consisting of layers of Mn tetrahedrally coordinated with Bi, and with Na intercalated between the layers. NaMnBi does not grow completely stoichiometrically, as Na is volatile and cannot completely enter the lattice. Na and Bi defects can be introduced into the lattice by quenching in liquid nitrogen after growth. The stoichiometry of the crystals can be measured using energy-dispersive X-ray spectroscopy (EDX). EDX can be accomplished using a scanning electron microscope (SEM), with a beam of electrons exciting the atoms near the surface and causing them to emit characteristic x-rays. EDX was performed on a single crystal of as-grown and quenched NaMnBi using a FEI Quanta LV200 SEM. The chemical ratio of the as-grown sample is estimated to be $\mathrm{Na}_{0.92}MnBi$ and the quenched sample is estimated to be $\mathrm{Na}_{0.82}\mathrm{MnBi}_{0.86}$. Images from the SEM are shown in Fig. 7-2 at two different magnifications. They crystal surfaces appear to be homogeneous without metallic inclusions.

Magnetoresistance and susceptibility measurements were carried out using a Quantum Design Physical Property Measurement System (PPMS). The resistivity was measured using the four-probe method. The single crystal is attached to a resistivity puck and four wires are attached to the crystal with silver epoxy. The two outside wires provide a constant current source, and the inside wires are attached to a high impedance voltmeter. The resistivity of the as-grown and quenched samples are shown in Fig. 7-3. The quenched samples is metallic at 0 field with a hysteresis in the resistivity around 250 K. The resistivity of the as-grown sample is much higher and the as-grown NaMnBi is a semiconductor.

The resistivity was also measured for each sample as a function of magnetic field. The resistivity was measured from 2 to 300 K at fields from 0 to 9 T. When the magnetic field is turned on, the electrical response of the as-grown and quenched crystals are significantly different. The magnetotransport results are summarized in Fig. 7-4. Between 0 and 9 T, the resistivity of the as-grown crystal shows a modest

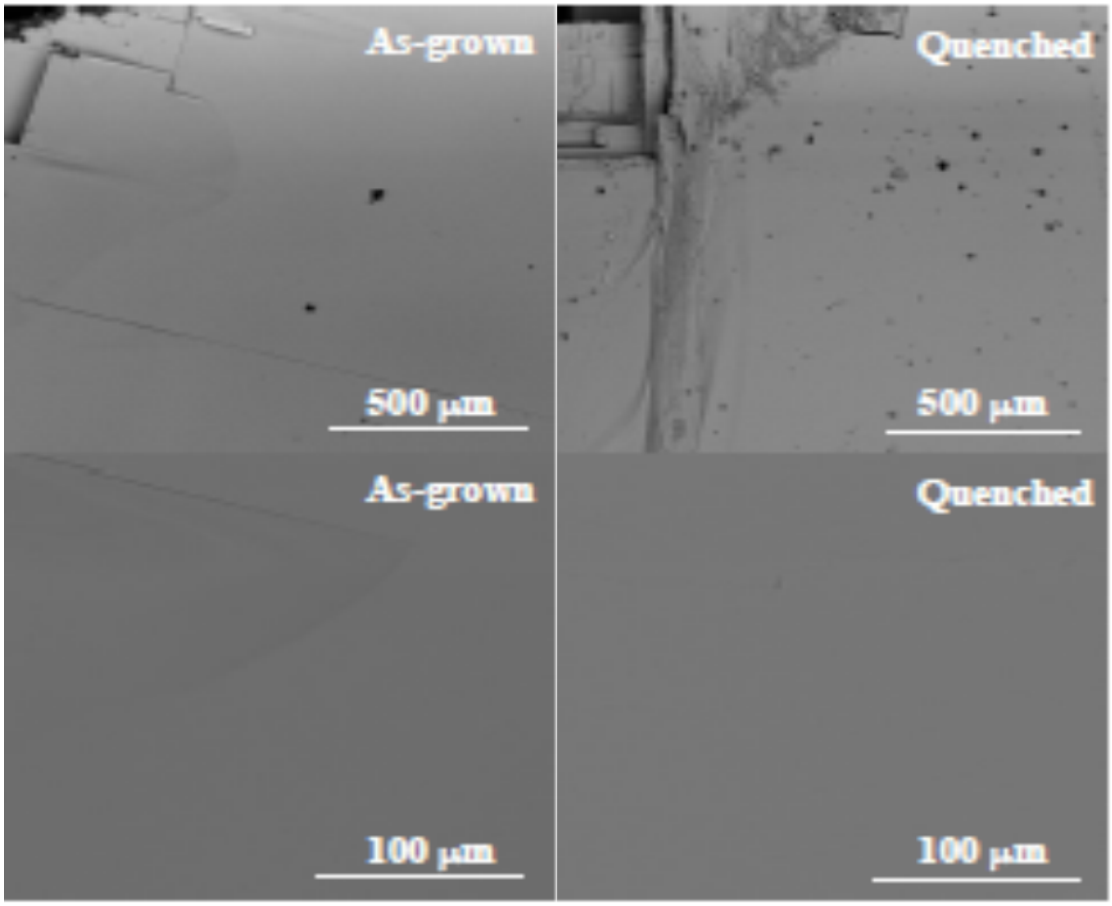


**Figure 7-2:** SEM images of as-grown and quenched NaMnBi at two different magnifications show crystals that appear smooth without inclusions.[150]

increase upon cooling (20%) Fig. 7-4(A). However, the resistivity of the quenched crystal increases significantly between 0 and 9 T as seen in Fig. 7-4(B). This gives rise to an anomalously large positive MR that increases substantially upon cooling. Classical MR is a weak effect that commonly appears in non-magnetic systems under a magnetic field, H. Defined as the ratio of the change of resistivity with field to the resistivity without field, $\frac{\Delta\rho(H)}{\rho(0)} = \frac{[\rho(H)-\rho(0)]}{\rho(0)}$, and is usually positive.[151]

The anomalously large positive MR, as shown here, is uncommon. Plotted at two temperatures as a function of field, the MR increases by more than 10,000 % by 2 K and 9 T while at room temperature, it reaches 600 %, an appreciable value (Fig. 7-4D). On the other hand, the MR observed in the as-grown crystal is significantly smaller (Fig. 7-4(C). To date, the observed MR reported here is the largest MR

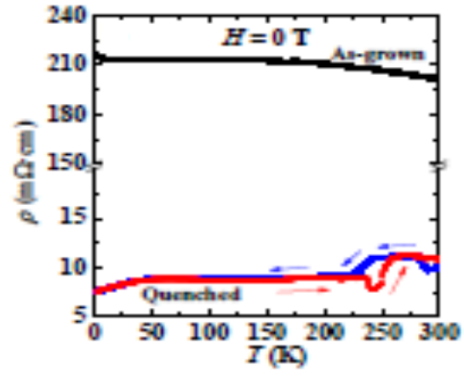


**Figure 7-3:** The zero field resistivity of as-grown (black) and quenched (red and blue) shows that quenching reduces the resistivity significantly and that there is a hysteresis in the quenched crystal.[150]

observed in a I-Mn-V semiconductor.

The magnetization of NaMnBi can be found by measuring the susceptibility using the PPMS. The energy of a magnetic moment in a magnetic field is $E = -m \cdot B$. The magnetization is measured by applying a small gradient to the magnetic field at the location of the sample. A force acts on the sample because of the gradient, $F = -\nabla E = m\frac{dB}{dz}$ and is measured. The magnetization measured at 0.1 T also show a kink near 250 K, the same temperature as the hysteresis in the resistivity. The as-grown sample follows expected AFM behavior, as seen in Fig. 7-5.

## 7.3 Neutron Diffraction Measurements of NaMnBi

### 7.3.1 Average Structure of NaMnBi

In order to determine the mechanism behind the different magnetotransport behavior, neutron diffraction experiments were carried out. Constant wavelength measurements with $\lambda = 2.411$ were carried out at BT-1 and HB2-a. At HB2-a, as-grown, quenched, and samples doped with potassium were measured as a function of temperature. For all samples, the high temperature phase above the Néel temperature is P4/nmm and there is little difference between the structures. As the magnetic ordering occurs, the magnitude of the magnetic moment is the same in all samples. Upon cooling, superlattice peaks appear that are not associated with the magnetic

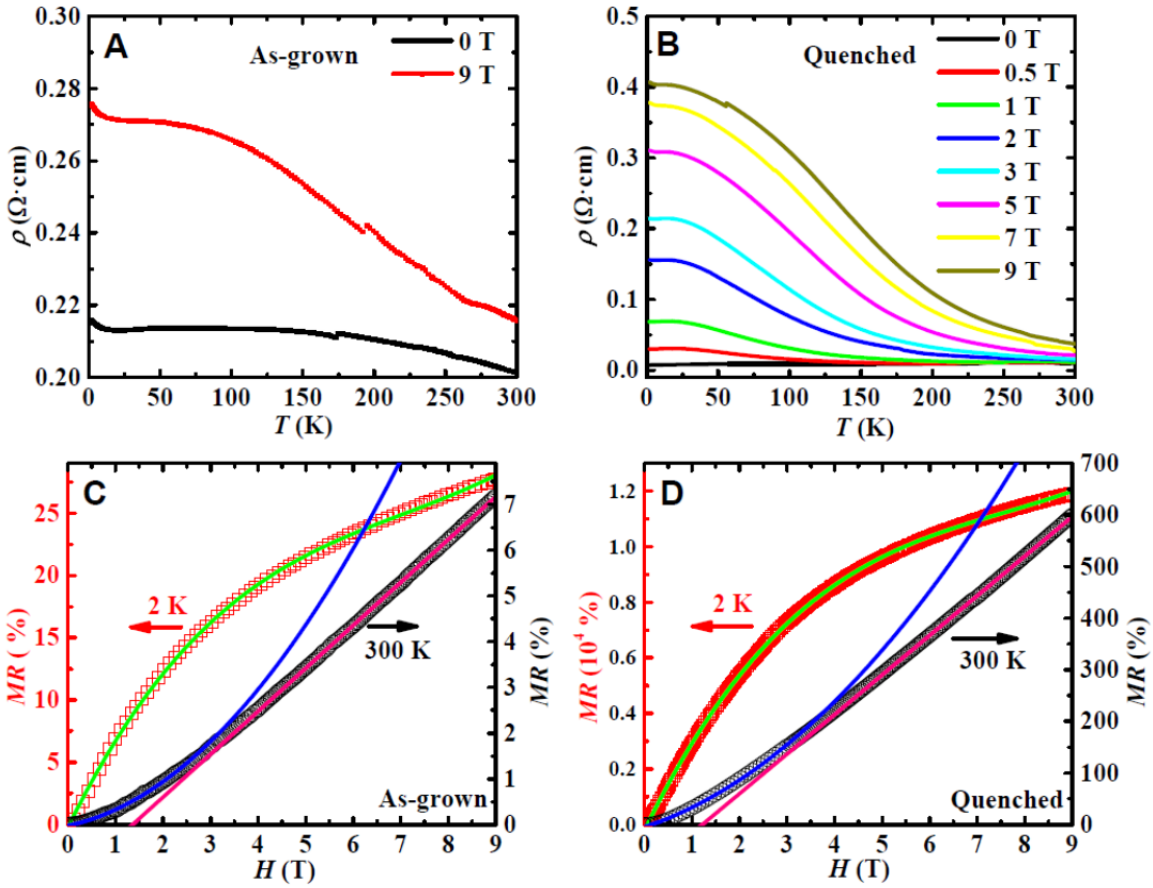


**Figure 7-4:** (A) The resistivity of as-grown NaMnBi at 0 and 9 T shows a modest increase in resistance. (B) The resistivity of quenched NaMnBi increases significantly with magnetic field. (C) The MR of as-grown NaMnBi increases by 25% at 2 K and 7% at 300 K at 9 T. (D) The MR of quenched NaMnBi increases by 10000% at 2 K and 600% at 300 K at 9 T[150]

phase. Fig. 7-6 shows the diffraction pattern of as-grown NaMnBi at 4 K (black), 150 K (red), and 350 K (blue). The hkl indices of the peaks are labeled. Tick marks are shown below the data corresponding to indices for the low temperature phase, high temperature phase, magnetic phase, and pure Bi left over from the reaction. The (100), (101), and (102) peaks are either entirely or partly from the magnetic peaks. The magnetic peaks do not appear at the highest temperature and the moment vanishes sharply. There is a small superlattice peak, indexed as ($\frac{2}{3}$, 0, 1). The superlattice peak, shown in the inset, is barely larger than the background at 4 K and has vanished between 100 and 150 K.

Fig. 7-7 shows the diffraction pattern of quenched NaMnBi at 4 K (black), 150 K

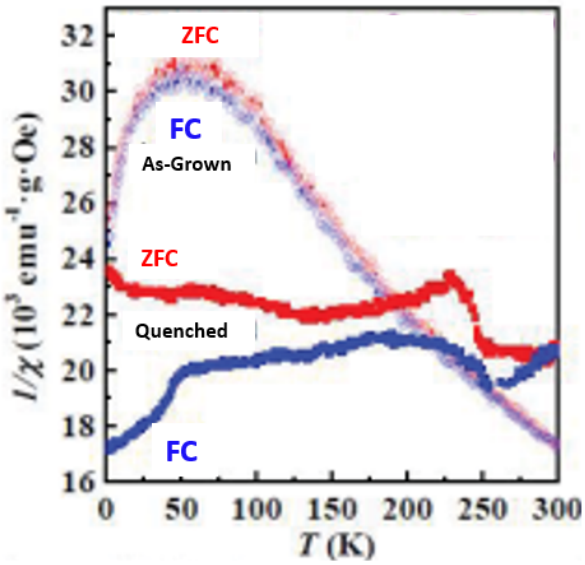


**Figure 7-5:** The inverse susceptibility of the as-grown and quenched samples. The quenched sample has a kink in the magnetization at the same temperature as the resistivity hysteresis[150]

(red), and 350 K (blue). In the quenched sample, there is still a small magnetic (100) peak at 350 K. The superlattice peak is much stronger and appears at a higher temperature in the quenched sample compared to the as-grown sample. The structural phase transition occurs between 250 and 300 K and is consistent with the hysteresis in the resistivity measured in the quenched NaMnBi.

The order parameters can be measured by calculating the integrated intensity of the peaks as a function of temperature. For the magnetic order parameter, the (100) peak is chosen because there is no contribution from the structural peaks. For the structural phase transition, the ($\frac{2}{3}$, 0, 1) peak is measured. For both peaks, the order parameter is normalized by dividing by the intensity of the (110) peak. The normalization is necessary because the overall intensity of the measurements of the samples was different. The order parameter is shown in Fig. 7-8. For the charge ordering structural transition, the order parameter for the quenched samples is 10 times as high as the as-grown sample.

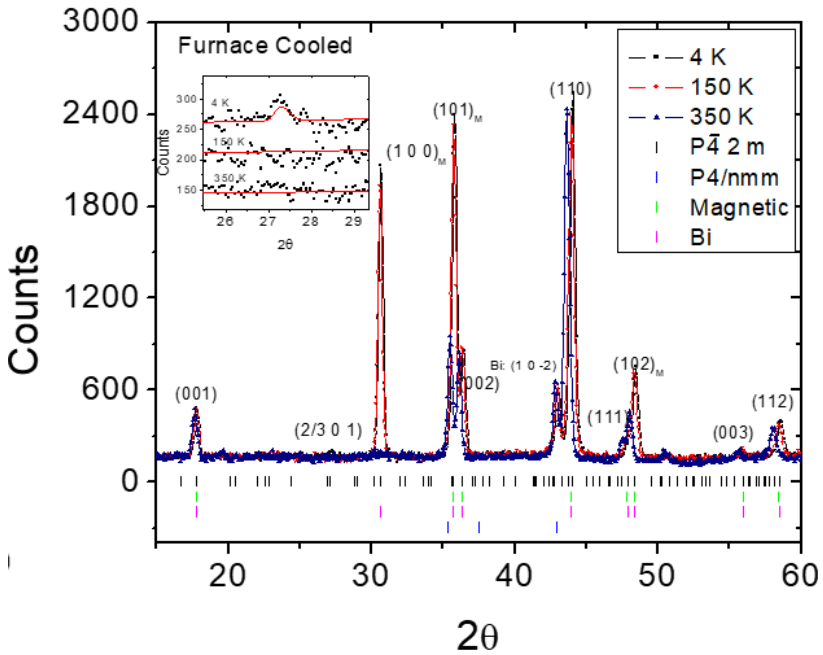


**Figure 7-6:** The constant wavelength neutron scattering is shown for furnace cooled NaMnBi.

### 7.3.2 The Average Structure of NaMnBi

Rietveld refinement is used to find a model for the average structure and see how the lattice changes with temperature. At 4 K, the $a$- and $c$- lattice constants are 4.514 and 7.647 Å in the quenched sample and 4.517 and 7.653 Å in the as grown sample, respectively. At 300 K, the $a$- and $c$- lattice constants have increased to 4.550 and 7.709 Å in the quenched sample and 4.564 and 7.735 Å in the as grown sample. The thermal expansion of the lattice with temperature is expected, as most materials expand when heated. The lattice expands more quickly above the Néel transition. A plot of the temperature dependence of the lattice constants is shown in Fig. 7-9.

In order to fit the $(\frac{2}{3}, 0, 1)$ peak, the symmetry is lowered. As the magnetic peaks do not change with the structural phase transition, the positions of the Mn atoms are fixed. In the as-grown sample, a $P\overline{4}m2$ space group with a 3 x 3 x 1 lattice expansion is used to fit the low temperature structure. The Bi distortions in the a-b plane have a magnitude of around 0.05 Å as seen in Fig. 7-10. The Na atoms move in the a-b plane in the opposite direction of the Bi atoms. This distortion forms a polaron.

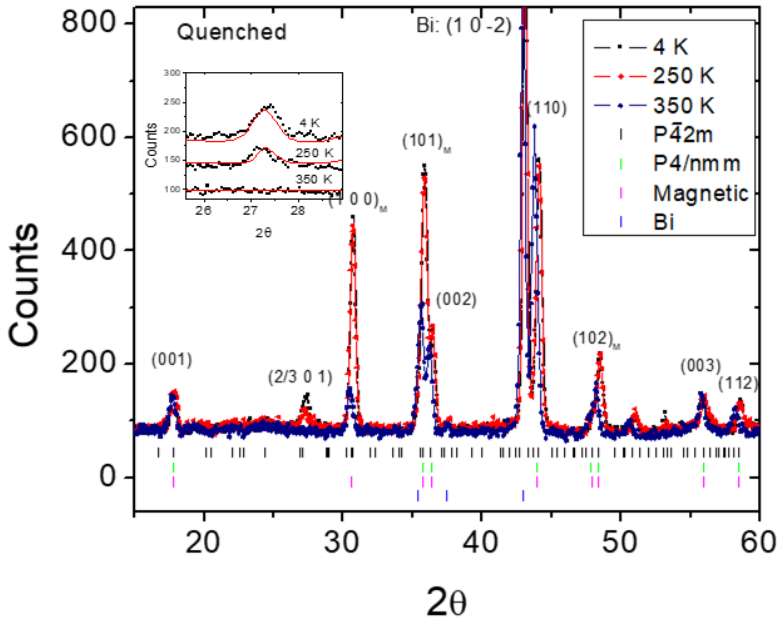


**Figure 7-7:** The constant wavelength neutron diffraction pattern is shown for NaMnBi that was quenched in liquid nitrogen.

The structural transition in the quenched sample can be attributed to vacancy ordering in addition to a periodic lattice distortion. The unit cell for the quenched CDW phase is a 3 x 3 x 2 superlattice of the high temperature phase. The space group $P\bar{4}m2$ is the same as in the as-grown sample. In the quenched sample, the refined occupancy of the Bi leads to a Bi occupancy of 0.57 at the (0, $\frac{1}{2}$, z) sites. When a Bi is missing from the tetrahedron, the Bi adjacent to the vacancy along the axis switch to the opposite layer. The result is that the Mn with only three neighbors are in a trigonal pyramidal configuration and the some of the Mn with four neighbors have a rectangular prismatic coordination. The different coordination geometries and the pattern they from in the unit cell is shown in Fig. 7-11 and the lattice distortion in the quenched sample is shown in Fig. 7-12. The new coordination geometries lead to a Bi-Bi bonds that are shorter than the tetrahedral bonds.

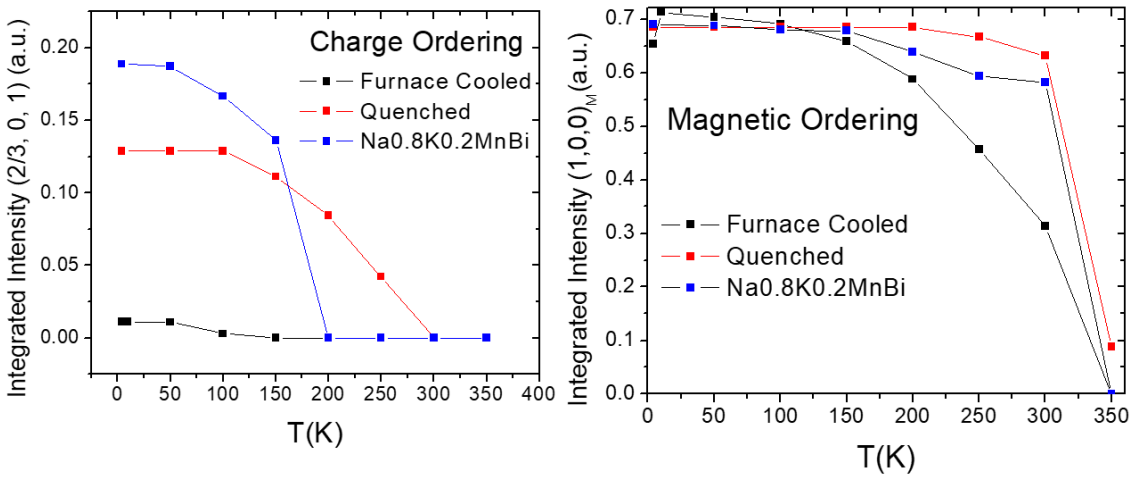


**Figure 7-8:** The order parameter for the structural (left) and magnetic (right) phase transitions in NaMnBi.

### 7.3.3 Local Structure of NaMnBi

In order to investigate the local structure, NaMnBi samples that were furnace cooled and quenched in liquid nitrogen were scanned at NOMAD as a function of temperature. For scans above room temperature, the samples were loaded into quartz capillaries and heated with a stream of gas in a sample changer. For low temperature measurements, the samples were loaded into V cans and placed in a cryostat. The samples were measured from 4 K to 370 K in steps of approximately 50 K, with smaller steps near the phase transitions. Reitveld refinement shows that both samples have a phase of pure Bi from the excess flux, with about 43 % Bi in the quenched sample and 18% Bi in the as-grown sample.

Fig. 7-13 shows the PDF of NaMnBi for the quenched and as grown samples fit with the vacancy ordered model and the undistorted high temperature average structure model at 5 K. The PDF is Fourier transformed with a $Q_{max} = 37$ Å. As both samples have Bi impurities, the contributions to the PDF from Bi are plotted below the data in blue. Fig. 7-13 shows the PDF of the (a) furnace cooled and (b) quenched samples with the high temperature model. With this model, all Mn are tetrahedrally coordinated by Bi. The first Mn-Bi peak occurs at 2.8Å, which fits the data well, however the Bi-Bi peaks do not fit the data. Using this model, the shortest

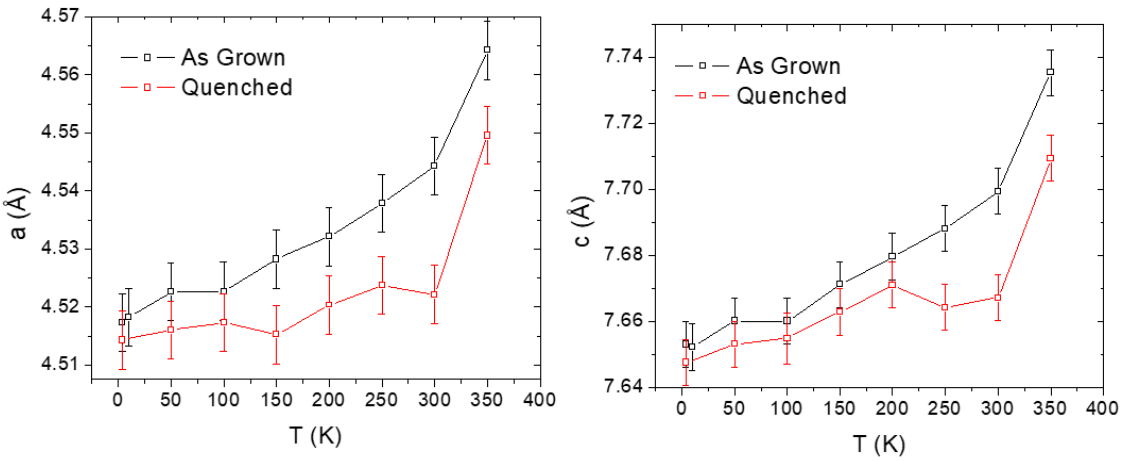


**Figure 7-9:** The lattice constant of as-grown and quenched NaMnBi as a function of temperature. There is a sharp increase above the Néel transition.

Bi-Bi nearest neighbors are expected to be 4.2 Å apart. The PDF of both samples shows peaks at 3.03Å and 3.49 Å that are not fit by the model. The vacancy ordered phase is used to fit the data in Fig. 7-13 (c-d). Due to the Bi that switches layers, there are Bi-Bi bonds of 3.03 Å in this model. Na-Bi bonds fit the peak at 3.49Åwell. The short Bi bonds occur even in the furnace cooled sample, although there are fewer short Bi-Bi bonds than in the quenched sample. This is due to a smaller number of vacancies, so that although on average all Mn have a tetrahedral coordination in the furnace cooled sample, the few vacancies that do exist affect their neighbors in the same way as the vacancies in the quenched sample. Fig. 7-14 shows the PDF at 290 K, above the structural transition. The shortened Bi peaks at 3.03 Å still occur at high temperature, although the peaks are much broader. This indicates that the local effect on the lattice caused by vacancies occurs even when the vacancies are not ordered.

Although the furnace cooled sample does not have the strong vacancy ordering transition of the quenched sample, the PDF indicates that there is still a change in the local environment of some Mn atoms and that there is local disorder. Above the transition temperature the local structure does not match the average structure for either sample as the shorter Bi-Bi peaks persist. This indicates that Bi vacancies have

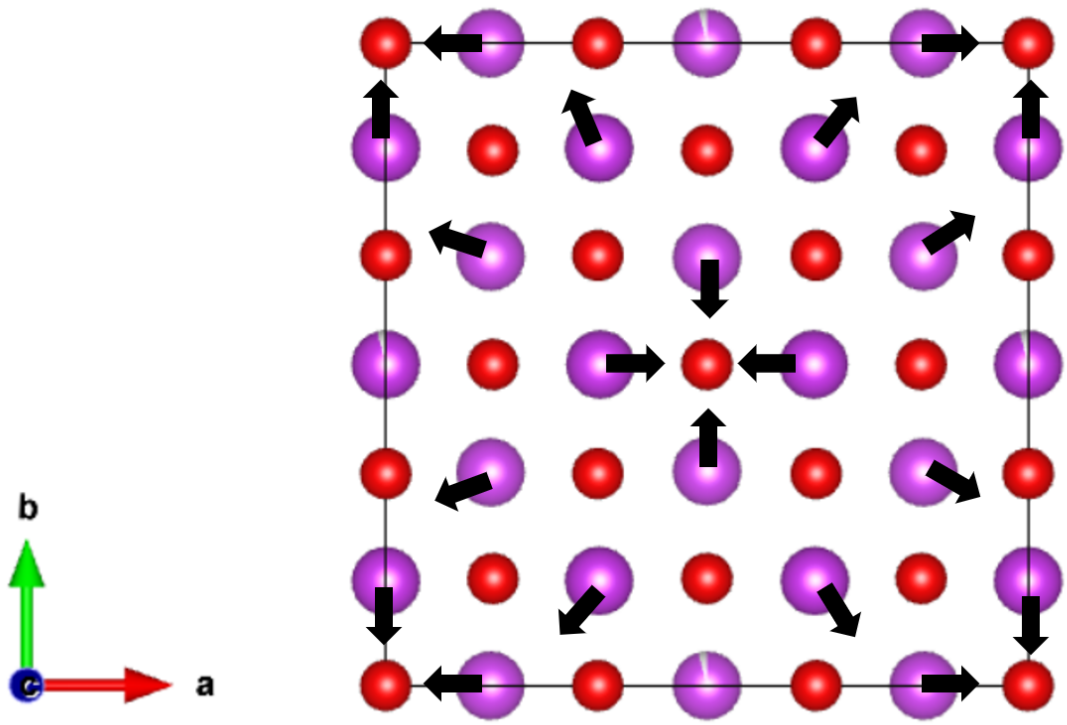


**Figure 7-10:** The direction of the Bi distortions is shown with Bi atoms in purple and Mn atoms in red. The Na atoms are not shown to reduce clutter, but they move in the opposite direction of Bi. This is indicative of a polaron formation.

an effect on the location of neighboring Bi, but when the vacancies are disordered the position is on average the same as the P4/nmm with disorder that does not affect the Bragg peaks. The result in the diffraction patterns is an increase in diffuse scattering leading to a higher background.

## 7.4 Discussion

The MR of NaMnBi is found to change from around 25% at 2 K and 9 T and 7% at 300 K and 9T for stoichiometric NaMnBi to 10000% and 600% when 15% Bi vacancies are introduced to the lattice. There is a vacancy ordering transition observed with neutron scattering in the quenched sample that is accompanied by a hysteresis in the resistivity. The as grown sample has no hysteresis and the periodic

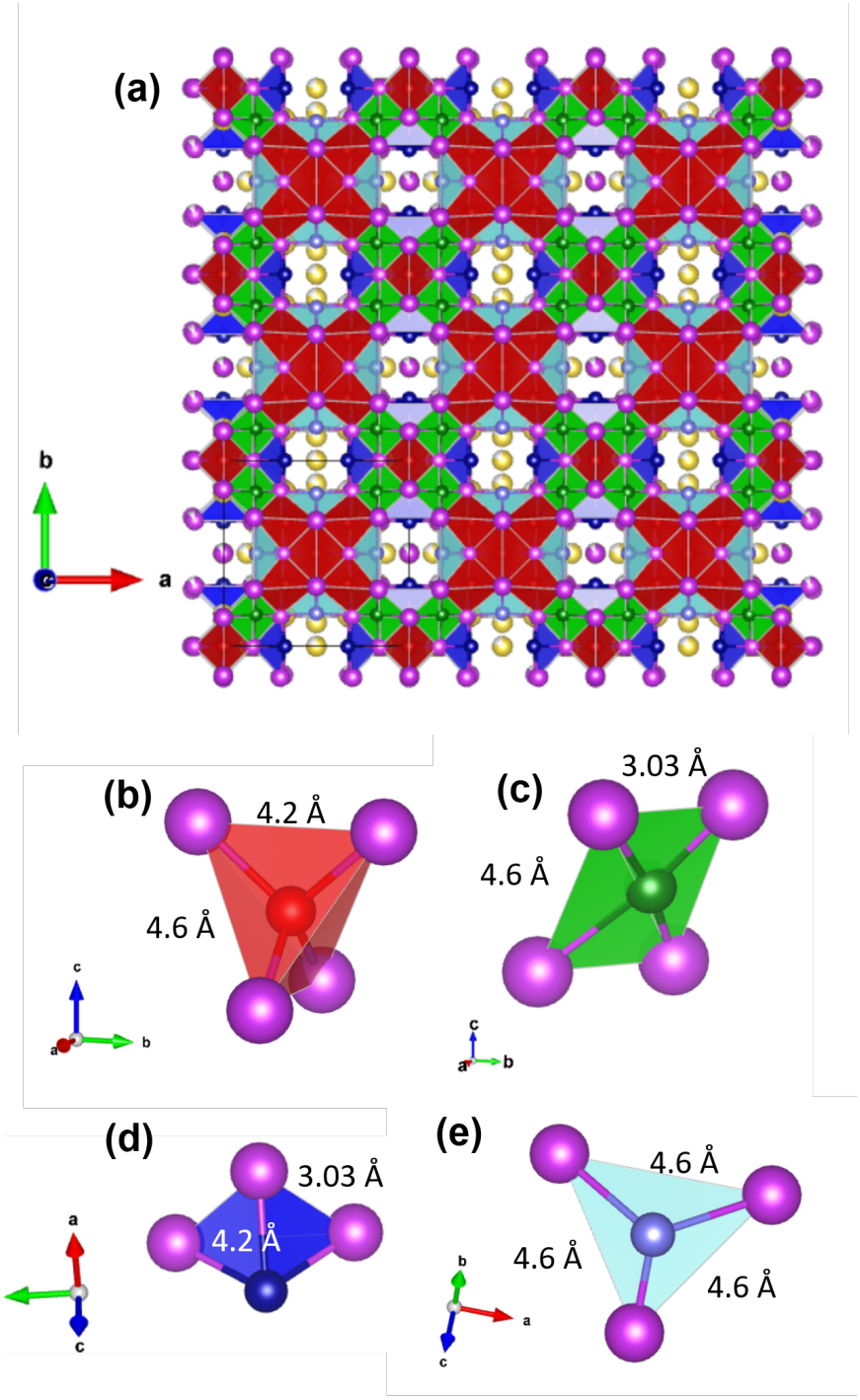


**Figure 7-11:** (a) The pattern of the Bi coordination geometries about Mn is shown, color-coded to the (b) tetrahedral coordination, (c) rectangular planar, (d-e) and two distinct triangular prismatic geometries.

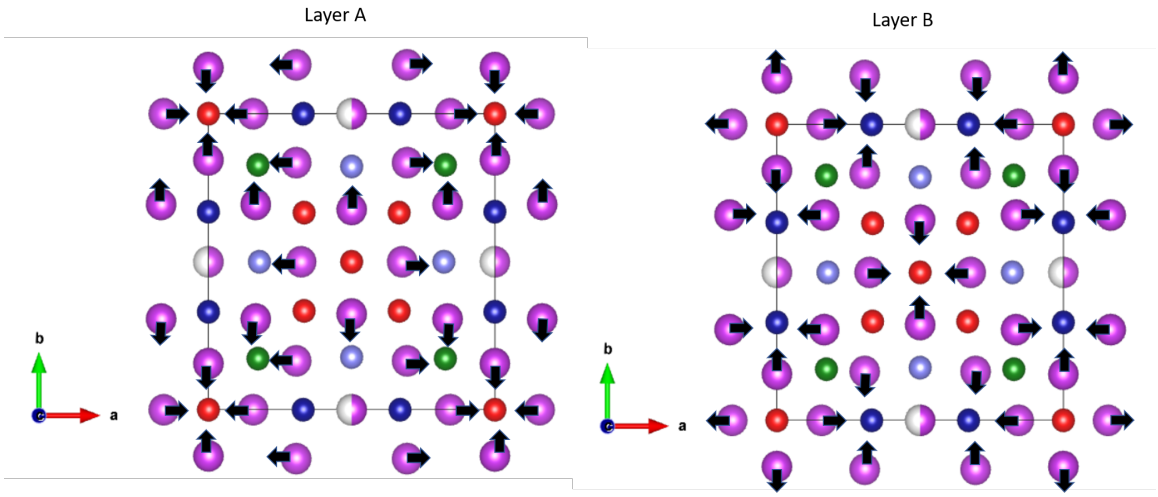


**Figure 7-12:** The directions of the periodic lattice distortion of the Bi atoms in the quenched sample is shown. The distortion is 3 x 3 x 2 and the directions of the distortion are different in every other layer of the unit cell.

lattice distortion transition is subtle. Neutron diffraction studies show that inversion symmetry is broken locally at high temperature and globally at low temperature. The coordination of Mn by Bi changes significantly with the introduction of vacancies.

While it is difficult to specify the exact microscopic explanation for the MR behavior, it is clear that vacancies and the local structure are key to tuning the behavior. It is known that enhanced spin fluctuation in antiferromagnets under a magnetic field can raise MR, which could play a role in the transition.[152, 153] The Bi and Mn bands are located near the Fermi surface and are involved with the electrical properties of the system, while the Na acts as an electron donor. This would suggest that hybridization between Bi and Mn bands leads to the changes in the MR properties. The results of the local structure analysis supports the idea that Bi-Mn hybridization is driving the XMR, as the Bi-Mn coordination changes significantly between quenched and as-grown samples.

Despite the differences in stoichiometry, both samples have a magnetic ordering with a large magnetic moment of over 4 $\mu_b$. The periodic lattice distortion pattern in the as-grown pattern is polaronic, while the quenched structure is dominated by the vacancy ordering transition. Polaron melting has a significant effect on the properties of CMR manganites and may play a role in the MR in this material[154]. Bi

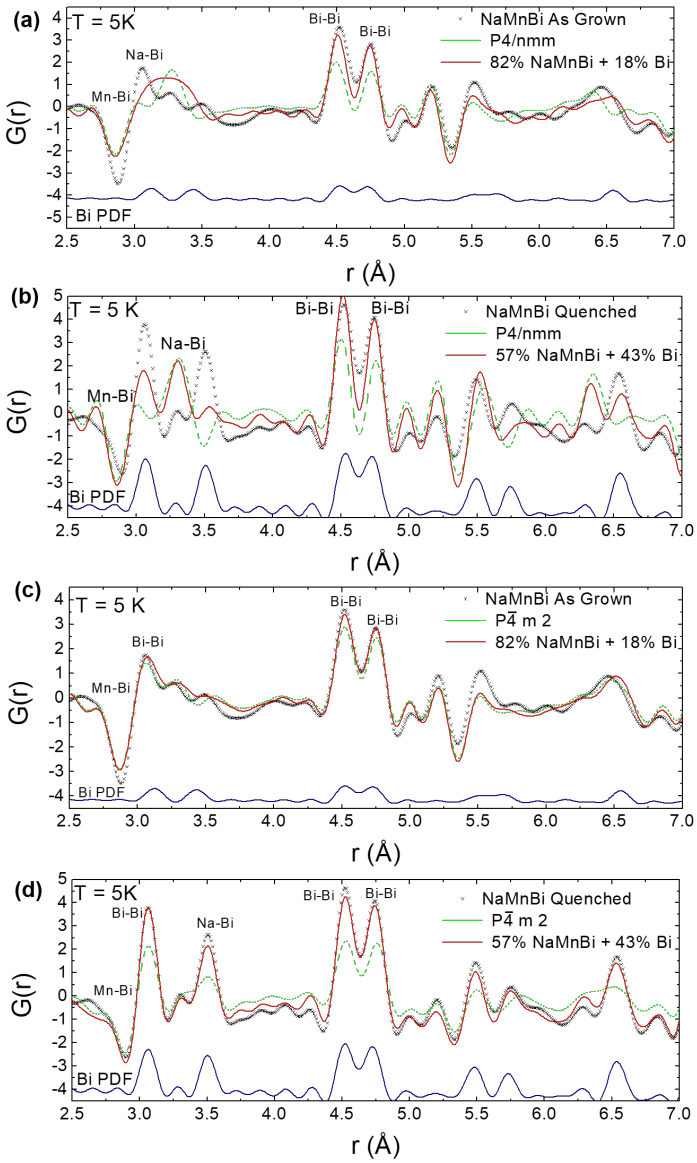


**Figure 7-13:** The PDF for the (a) furnace cooled and (b) quenched samples are fit with the P4/nmm model at 5 K. The PDF for the (c) furnace cooled and (d) quenched samples are fit with the vacancy ordered model at 5 K.

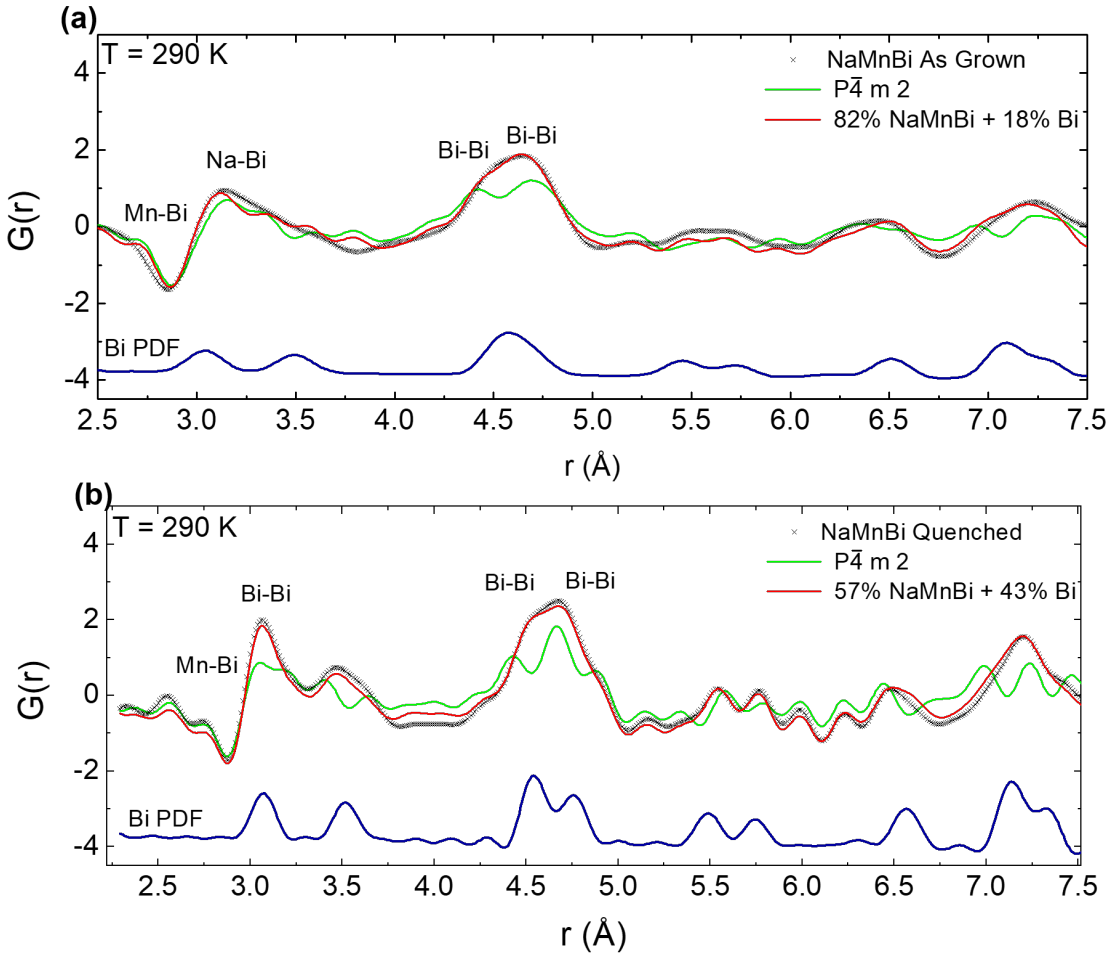


**Figure 7-14:** The PDF of (a) furnace cooled and (b) quenched NaMnBi at 290 K is fit with the model. The local distortions are still present despite the average structure.

is well known for easily forming compounds with different valence structures, and it is possible that charge dispropportionation is present in this system and stabilizes the vacancy ordering structure and plays a role in the XMR. Additionally, the model used to fit the vacancy ordered phase and local structure features a broken inversion symmetry. Broken inversion symmetry is crucial to controlling spin-polarized electrons with spin orbit torque, which is a very important property in AFM spintronics applications[141], and the observation of the broken inversion symmetry suggests that further study of this material for spin-orbit effects would be fruitful.

# Chapter 8

# Conclusions

Semiconductors with novel electronic and magnetic properties are promising candidates for the next generation of materials as they can be used to make lightweight or flexible devices and may be less volatile than available electronic devices. In order to optimize devices, the properties of materials must be understood so that they may be tuned. CDW formation in TMDs has been studied for decades. The failure of Fermi surface nesting and exciton condensation to completely explain the transition necessitates further investigation of the electron-lattice interactions which manifest in a Jahn-Teller distortion. $TiSe_{2-x}Te_x$ was investigated using neutron diffraction to reveal how the local structure of the system changes through the CDW transition.

In $TiSe_2$, two explanations possible have been given why a JT-like mechanism could lead to a CDW. The different mechanisms depend on the occupancy of the d-band and the local interactions in the Ti-Se octahedra. In the CDW phase there are two separate Ti sites. In the band-Jahn Teller (BJT) effect, the distortions of the Se about the first Ti site lower the energy of the d-band of Ti. This mechanism depends on the direction of the distortion and requires a partially occupied Ti d band. With the pseudo-Jahn Teller (PJT) effect, shortening of the Ti-Se bonds at the second Ti site causes a lowering of the energy of the Se p band.

The two proposed JT mechanisms cannot be distinguished from the average structure analysis. Although the CDW has been earlier observed by neutron diffraction, the published model does not uniquely define the superlattice structure. From the

PDF analysis, it can be inferred that $\frac{1}{8}^{th}$ of the Ti-Se nearest neighbor bonds are shortened by 0.16 Å. The splitting persists above the CDW transition temperature. This bond splitting is greater than can be achieved with the $P\overline{3}c1$ symmetry that is necessary for the BJT mechanism. The bond shortening, which is crucial to the PJT model, can be reproduced by a model in which the Ti atoms move towards Se atoms in a breathing mode distortion.

Further evidence that the PJT mechanism drives the CDW instability is found by doping with Te. $TiTe_2$ has more charge transfer to the Ti d orbitals and no CDW transition[129]. When Te is doped substitutionally for Se, the CDW is suppressed between 10% and 12.5% of Te. In $TiSe_{2-x}Te_x$ samples up to x = 0.1, the CDW is observed, coupled with the Ti-Se bond splitting. For samples with a Te concentration above the critical concentration, there is no evidence for the CDW. This indicates that the Ti-Se/Te peak splitting is indeed necessary for the long range CDW order at low temperatures. In the high temperature non-CDW phase, $TiTe_2$ is found to have a monoclinic structure locally. This can be attributed to occupation of the Ti d orbitals that leads to a degeneracy that breaks the trigonal symmetry. This transfer to the d band is caused by Te doping and thermal fluctuations and gives further evidence that it is the PJT and not the BJT driving the CDW instability. However, the CDW exists in competition with superconductivity. Superconductivity occurs either when pressure is applied, when Cu is intercalated between the Se layers, or when Pd is doped substitutionally for Ti. To understand how superconductivity relates to the CDW, it would be interesting to study how the structure changes as the system becomes superconducting and how the changes effect the PJT distortions.

NaMnBi is the first reported I-Mn-V material to show high MR. In the stoichiometric phase, the MR reaches 25% at 2 K and 9 T and 7% at 300 K and 9 T. When Bi defects are introduced, the MR increases to 10,000% at 2 K and 600% at 300 K. A thermal hysteresis was observed in the zero field resistivity of the quenched sample around 250 K. The quenched sample has a hysteresis in the susceptibility and an anomaly at 50 K and 250 K. Neutron scattering was used to see the structural dependence of the samples. For the two types of samples investigated, the quenched and

as grown, the magnetic ordering appears at 340 K and has a magnitude of between 4 and 4.5 $\mu_B$. There is a periodic lattice distortion that is observed in both samples but is much stronger in the quenched sample. In the quenched sample, this can be attributed to a vacancy ordering transition with a 3 x 3 x 2 superlattice formation. In the as-grown sample the periodic lattice distortion has a 3 x 3 x 1 superstructure because only one of the superlattice peaks is observed. For both samples, the high temperature phase is fit with a P4/nmm symmetry, while the inversion symmetry is broken at low temperatures. The low temperature phase is fit with $P\overline{4}m2$ symmetry. The low temperature symmetry changes the coordination of some of the Bi, leading to short Bi-Bi bonds that are observed in the local structure.

It is likely that Mn-Bi hybridization causes the high MR, although the exact mechanism is still not well understood. As the high MR makes NaMnBi a good candidate for spintronic applications, it would be useful to measure anisotropy and exchange bias to see how it can be incorporated into device designs. The discoveries in this material open up new avenues for research in antiferromagnetic semimetals. The observation of broken inversion symmetry also implies that high spin-orbit torque is possible, and measurements of the spin-orbit effects could lead to a better understanding of the how this material can be used in future technologies.

# Bibliography


[1] J. Hodeau, M. Marezio, C. Roucau, R. Ayroles, A. Meerschaut, J. Rouxel, and P. Monceau. Charge-density waves in $NbSe_3$ at 145K: crystal structures, X-ray and electron diffraction studies. *Journal of Physics C: Solid State Physics*, 11(20):4117, 1978.

[2] A. Gabovich, A. Voitenko, T. Ekino, M. Li, H. Szymczak, and M. Pękała. Competition of superconductivity and charge density waves in cuprates: Recent evidence and interpretation. *Advances in Condensed Matter Physics*, 2010, 2010.

[3] J. Li, C. Wu, and D. Lee. Checkerboard charge density wave and pseudogap of high-$T_c$ cuprate. *Physical Review B*, 74(18):184515, 2006.

[4] X. Wan, H. Ding, S. Savrasov, and C. Duan. Electron-phonon superconductivity near charge-density-wave instability in $LaO_{0.5}F_{0.5}BiS_2$: Density-functional calculations. *Physical Review B*, 87(11):115124, 2013.

[5] X. Zhu, Y. Cao, J. Zhang, E. Plummer, and J. Guo. Classification of charge density waves based on their nature. *Proceedings of the National Academy of Sciences*, 112(8):2367–2371, 2015.

[6] P. Brace. Bearing lubricant for vacuum service, April 28 1942. US Patent 2,280,886.

[7] A. Conan, G. Goureaux, and M. Zoaeter. Transport properties of $MoTe_{2\text{-}x}$ and $MoSe_{2\text{-}x}$ compounds between 130 and 300 K. *Journal of Physics and Chemistry of Solids*, 36(4):315–320, 1975.

[8] S. Tongay, J. Zhou, C. Ataca, K. Lo, T. Matthews, J. Li, , and J. Wu. Thermally driven crossover from indirect toward direct bandgap in 2D semiconductors: $MoSe_2$ versus $MoS_2$. *Nano Letters*, 12(11):5576–5580, 2012.

[9] T. Finteis, M. Hengsberger, T. Straub, K. Fauth, R. Claessen, P. Auer, P. Steiner, S. Hüfner, P. Blaha, M. Vögt, et al. Occupied and unoccupied electronic band structure of $WSe_2$. *Physical Review B*, 55(16):10400, 1997.

[10] V. Gupta, P. Agarwal, A. Gupta, and V. Srivastava. Electronic properties of tin dichalcogenides $SnS_2$ and $SnSe_2$. *Journal of Physics and Chemistry of Solids*, 43(3):291–295, 1982.

[11] L Conroy and K. Park. Electrical properties of the group iv disulfides, titanium disulfide, zirconium disulfide, hafnium disulfide and tin disulfide. *Inorganic Chemistry*, 7(3):459–463, 1968.

[12] H. Isomäki, J. Von Boehm, and P. Krusius. The electronic ground state of the layer compounds ZrS, $TiS_2$ and $TiSe_2$. *Il Nuovo Cimento B (1971-1996)*, 38(2):168–175, 1977.

[13] S. Sharma, T. Nautiyal, G. Singh, S. Auluck, P. Blaha, and C. Ambrosch-Draxl. Electronic structure of 1 t- tis 2. *Physical Review B*, 59(23):14833, 1999.

[14] T. Shimada, F. Ohuchi, and A. Koma. Polytypes and charge density waves of ultrathin $TaS_2$ films grown by van der waals epitaxy. *Surface Science*, 291(1-2):57–66, 1993.

[15] T. Shishidou, A. Freeman, and R. Asahi. Effect of GGA on the half-metallicity of the itinerant ferromagnet $CoS_2$. *Physical Review B*, 64(18):180401, 2001.

[16] J. Ye, Y. Zhang, R. Akashi, M. Bahramy, R. Arita, and Y. Iwasa. Superconducting dome in a gate-tuned band insulator. *Science*, 338(6111):1193–1196, 2012.

[17] K. Novoselov, D. Jiang, F. Schedin, T. Booth, V. Khotkevich, S. Morozov, and A. Geim. Two-dimensional atomic crystals. *Proceedings of the National Academy of Sciences*, 102(30):10451–10453, 2005.

[18] Large, non-saturating magnetoresistance in $WTe_2$, author=Ali, M. and Xiong, J. and Flynn, S. and Tao, J. and Gibson, Q. and Schoop, L. and Liang, T. and Haldolaarachchige, N. and Hirschberger, M. and Ong, N. and others, journal=Nature, volume=514, number=7521, pages=205, year=2014, publisher=Nature Publishing Group.

[19] H. Tributsch. Layer-type transition metal dichalcogenidesâĂŤa new class of electrodes for electrochemical solar cells. *Berichte der Bunsengesellschaft für Physikalische Chemie*, 81(4):361–369, 1977.

[20] F. Withers, O. Del Pozo-Zamudio, S. Schwarz, S. Dufferwiel, P. Walker, T. Godde, A. Rooney, A. Gholinia, C. Woods, P. Blake, et al. Wse2 light-emitting tunneling transistors with enhanced brightness at room temperature. *Nano Letters*, 15(12):8223–8228, 2015.

[21] H Wang, H Feng, and J Li. Graphene and graphene-like layered transition metal dichalcogenides in energy conversion and storage. *Small*, 10(11):2165–2181, 2014.

[22] Q. Lu, Y. Yu, Q. Ma, B. Chen, and H. Zhang. 2d transition-metal-dichalcogenide-nanosheet-based composites for photocatalytic and electrocatalytic hydrogen evolution reactions. *Advanced Materials*, 28(10):1917–1933, 2016.

[23] M. Pumera and A. Loo. Layered transition-metal dichalcogenides $MoS_2$ and $WS_2$ for sensing and biosensing. *TrAC Trends in Analytical Chemistry*, 61:49–53, 2014.

[24] E. Morosan, H. Zandbergen, B. Dennis, J. Bos, Y. Onose, T. Klimczuk, A. Ramirez, N. Ong, and R. Cava. Superconductivity in $Cu_xTiSe_2$. *Nature Physics*, 2(8):544, 2006.

[25] A. Kusmartseva, B. Sipos, H. Berger, L. Forro, and E. Tutiš. Pressure induced superconductivity in pristine 1T-$TiSe_2$. *Physical Review Letters*, 103(23):236401, 2009.

[26] M. Baibich, J. Broto, A. Fert, F. Van Dau, F. Petroff, P. Etienne, G. Creuzet, A. Friederich, and J. Chazelas. Giant magnetoresistance of (001) Fe/(001) Cr magnetic superlattices. *Physical Review Letters*, 61(21):2472, 1988.

[27] S. Pearton. Magnetic semiconductors: Silicon-based spintronics. *Nature Materials*, 3(4):203, 2004.

[28] J. Walowski and M. Münzenberg. Perspective: Ultrafast magnetism and THz spintronics. *Journal of Applied Physics*, 120(14):140901, 2016.

[29] P. Ravindran. Spin ordering in perovskite oxides. https://folk.uio.no/ravi/activity/ordering/spinfig.html, note = Accessed: 2019-08-27.

[30] R. Peierls and R. Peierls. *Surprises in theoretical physics*. Princeton University Press, 1979.

[31] R. Kronig and W. Penney. Quantum mechanics of electrons in crystal lattices. *Proceedings of the Royal Society of London. Series A, Containing Papers of a Mathematical and Physical Character*, 130(814):499–513, 1931.

[32] Y. Ono and T. Hamano. Peierls distortion in two-dimensional tight-binding model. *Journal of the Physical Society of Japan*, 69(6):1769–1776, 2000.

[33] P. Grünberg, R. Schreiber, Y. Pang, M. Brodsky, and H. Sowers. Layered magnetic structures: Evidence for antiferromagnetic coupling of Fe layers across Cr interlayers. *Physical Review Letters*, 57(19):2442, 1986.

[34] M. Julliere. Tunneling between ferromagnetic films. *Physics Letters A*, 54(3):225–226, 1975.

[35] S. Yuasa, T. Nagahama, A. Fukushima, Y. Suzuki, and K. Ando. Giant room-temperature magnetoresistance in single-crystal Fe/MgO/Fe magnetic tunnel junctions. *Nature Materials*, 3(12):868, 2004.

[36] S. Ikeda, J. Hayakawa, Y. Ashizawa, Y. Lee, K. Miura, H. Hasegawa, M. Tsunoda, F. Matsukura, and H. Ohno. Tunnel magnetoresistance of 604% at 300 K by suppression of Ta diffusion in CoFeB/MgO/CoFeB pseudo-spin-valves annealed at high temperature. *Applied Physics Letters*, 93(8):082508, 2008.

[37] R. Mahendiran, S. Tiwary, A. Raychaudhuri, T. Ramakrishnan, R. Mahesh, N. Rangavittal, and C. Rao. Structure, electron-transport properties, and giant magnetoresistance of hole-doped $LaMnO_3$ systems. *Physical Review B*, 53(6):3348, 1996.

[38] G Matsumoto. Study of $(La_{1\text{-}x}Ca_x)MnO_3$. i. magnetic structure of $LaMnO_3$. *Journal of the Physical Society of Japan*, 29(3):606–615, 1970.

[39] D. Feinberg, P. Germain, M. Grilli, and G. Seibold. Joint superexchange–Jahn-Teller mechanism for layered antiferromagnetism in $LaMnO_3$. *Physical Review B*, 57(10):R5583, 1998.

[40] M. Ueno, H. Nagai, T. Sawasaki, and F. Hikami. Spin-valve magnetoresistance sensor and thin film magnetic head, January 22 2002. US Patent 6,340,533.

[41] S. Datta and B. Das. Electronic analog of the electro-optic modulator. *Applied Physics Letters*, 56(7):665–667, 1990.

[42] E. Rashba and V. Sheka. Symmetry of energy bands in wurzite-type crystals. ii. band symmetry with allowance for spin interactions. *Sov. Phys. Solid State*, 1:143, 1959.

[43] G. Dresselhaus. Spin-orbit coupling effects in zinc blende structures. *Physical Review*, 100(2):580, 1955.

[44] G. Wang, Z. Wang, J. Klein, and W. Zhao. Modeling for spin-fet and design of spin-fet-based logic gates. *IEEE Transactions on Magnetics*, 53(11):1–6, 2017.

[45] K. Hardee, D. Chapman, and J. Pineda. Dynamic random access memory, December 31 1991. US Patent 5,077,693.

[46] B. Wong. Static random access memory architecture, December 8 2009. US Patent 7,630,230.

[47] S. Bhatti, R. Sbiaa, A. Hirohata, H. Ohno, S. Fukami, and S. Piramanayagam. Spintronics based random access memory: a review. *Materials Today*, 20(9):530–548, 2017.

[48] X. Xu, C. Liu, Z. Sun, T. Cao, Z. Zhang, E. Wang, Z. Liu, and K. Liu. Interfacial engineering in graphene bandgap. *Chemical Society Reviews*, 47(9):3059–3099, 2018.

[49] J. Li, G. Gui, and J. Zhong. Tunable bandgap structures of two-dimensional boron nitride. *Journal of Applied Physics*, 104(9):094311, 2008.

[50] W. Choi, N. Choudhary, G. Han, J. Park, D. Akinwande, and Y. Lee. Recent development of two-dimensional transition metal dichalcogenides and their applications. *Materials Today*, 20(3):116–130, 2017.

[51] A. Kuc. Low-dimensional transition-metal dichalcogenides. *Chem. Modell*, 11(1), 2014.

[52] K. Tate. Periodic table of elements. https://www.livescience.com/25300-periodic-table.html, note = Accessed: 2019-07-11, 2017.

[53] G. Eda, H. Yamaguchi, D. Voiry, T. Fujita, M. Chen, and M. Chhowalla. Photoluminescence from chemically exfoliated $MoS_2$. *Nano Letters*, 11(12):5111–5116, 2011.

[54] T. Weirich. The crystal structure of $Zr_2Se$ reinvestigated by electron crystallography and X-ray powder diffraction. *Crystallography Reports*, 49(3):379–389, 2004.

[55] A. Ibarz, E. Ruiz, and S. Alvarez. Electronic structure of host lattices for intercalation compounds: $SnS_2$, $SnSe_2$, $ZrS_2$, and $TaS_2$. *Chemistry of Materials*, 10(11):3422–3428, 1998.

[56] M. Yoder. Wide bandgap semiconductor materials and devices. *IEEE Transactions on Electron Devices*, 43(10):1633–1636, 1996.

[57] H. Komsa and A. Krasheninnikov. Effects of confinement and environment on the electronic structure and exciton binding energy of $MoS_2$ from first principles. *Physical Review B*, 86(24):241201, 2012.

[58] K. Mak, K. He, C. Lee, G. Lee, J. Hone, T. Heinz, and J. Shan. Tightly bound trions in monolayer $MoS_2$. *Nature Materials*, 12(3):207, 2013.

[59] Identification of excitons, trions and biexcitons in single-layer $WS_2$, author=Plechinger, G. and Nagler, P. and Kraus, J. and Paradiso, N. and Strunk, C. and Schüller, C. and Korn, T., journal=Physica Status Solidi (RRL)–Rapid Research Letters, volume=9, number=8, pages=457–461, year=2015, publisher=Wiley Online Library.

[60] A. Beal and W. Liang. Excitons in 2H-$WSe_2$ and 3R-$WS_2$. *Journal of Physics C: Solid State Physics*, 9(12):2459, 1976.

[61] H. Shi, R. Yan, S. Bertolazzi, J. Brivio, B. Gao, A. Kis, D. Jena, H. Xing, and L. Huang. Exciton dynamics in suspended monolayer and few-layer $MoS_2$ 2D crystals. *ACS Nano*, 7(2):1072–1080, 2013.

[62] J. Ross, S. Wu, H. Yu, N. Ghimire, A. Jones, G. Aivazian, J. Yan, D. Mandrus, D. Xiao, W. Yao, et al. Electrical control of neutral and charged excitons in a monolayer semiconductor. *Nature Communications*, 4:1474, 2013.

[63] Strain-induced direct–indirect bandgap transition and phonon modulation in monolayer $WS_2$, author=Wang, Y. and Cong, C. and Yang, W. and Shang, J. and Peimyoo, N. and Chen, Y. and Kang, J. and Wang, J. and Huang, W. and Yu, T., journal=Nano Research, volume=8, number=8, pages=2562–2572, year=2015, publisher=Springer.

[64] I. Niehues, R. Schmidt, DruÌĹppel M., P. Marauhn, D. Christiansen, M. Selig, G. BerghaÌĹuser, D. Wigger, R. Schneider, L. Braasch, et al. Strain control of exciton–phonon coupling in atomically thin semiconductors. *Nano Letters*, 18(3):1751–1757, 2018.

[65] Y. Hui, X. Liu, W. Jie, N. Chan, J. Hao, Y. Hsu, L. Li, W. Guo, and S. Lau. Exceptional tunability of band energy in a compressively strained trilayer $MoS_2$ sheet. *ACS Nano*, 7(8):7126–7131, 2013.

[66] M. Park, Y. Park, X. Chen, Y. Park, M. Kim, and J. Ahn. $MoS_2$-based tactile sensor for electronic skin applications. *Advanced Materials*, 28(13):2556–2562, 2016.

[67] V. Mihailetchi, L. Koster, J. Hummelen, and P. Blom. Photocurrent generation in polymer-fullerene bulk heterojunctions. *Physical review letters*, 93(21):216601, 2004.

[68] J. Sambur, T. Novet, and B. Parkinson. Multiple exciton collection in a sensitized photovoltaic system. *Science*, 330(6000):63–66, 2010.

[69] R. Cheng, D. Li, H. Zhou, C. Wang, A. Yin, S. Jiang, Y. Liu, Y. Chen, Y. Huang, and X. Duan. Electroluminescence and photocurrent generation from atomically sharp $WSe_2/MoS_2$ heterojunction p–n diodes. *Nano letters*, 14(10):5590–5597, 2014.

[70] C. Lee, H. Yan, L. Brus, T. Heinz, J. Hone, and S. Ryu. Anomalous lattice vibrations of single-and few-layer $MoS_2$. *ACS Nano*, 4(5):2695–2700, 2010.

[71] H. Li, Q. Zhang, C. Yap, B. Tay, T. Edwin, A. Olivier, and D. Baillargeat. From bulk to monolayer $MoS_2$: evolution of raman scattering. *Advanced Functional Materials*, 22(7):1385–1390, 2012.

[72] B. Chakraborty, A. Bera, D. Muthu, S. Bhowmick, U. Waghmare, and A. Sood. Symmetry-dependent phonon renormalization in monolayer $MoS_2$ transistor. *Physical Review B*, 85(16):161403, 2012.

[73] P. Tonndorf, R. Schmidt, P. Böttger, X. Zhang, J. Börner, A. Liebig, M. Albrecht, C. Kloc, O. Gordan, D. Zahn, et al. Photoluminescence emission and raman response of monolayer $MoS_2$, $MoSe_2$, and $WSe_2$. *Optics Express*, 21(4):4908–4916, 2013.

[74] A. Soluyanov, D. Gresch, Z. Wang, Q. Wu, M. Troyer, X. Dai, and B. Bernevig. Type-II Weyl semimetals. *Nature*, 527(7579):495, 2015.

[75] Z. Wang, D. Gresch, A. Soluyanov, W. Xie, S. Kushwaha, X. Dai, M. Troyer, R. Cava, and B. Bernevig. $MoTe_2$: a type-II Weyl topological metal. *Physical Review Letters*, 117(5):056805, 2016.

[76] K. Deng, G. Wan, P. Deng, K. Zhang, S. Ding, E. Wang, M. Yan, H. Huang, H. Zhang, Z. Xu, et al. Experimental observation of topological fermi arcs in type-II Weyl semimetal $MoTe_2$. *Nature Physics*, 12(12):1105, 2016.

[77] B Brown. The crystal structures of $NbT_2$ and $TaTe_2$. *Acta Crystallographica*, 20(2):264–267, 1966.

[78] C. Battaglia, H. Cercellier, F. Clerc, L. Despont, M. Garnier, C. Koitzsch, P. Aebi, H. Berger, L. Forró, and C. Ambrosch-Draxl. Fermi-surface-induced lattice distortion in $NbTe_2$. *Physical Review B*, 72(19):195114, 2005.

[79] J. Wilson, F. Di Salvo, and S. Mahajan. Charge-density waves and superlattices in the metallic layered transition metal dichalcogenides. *Advances in Physics*, 24(2):117–201, 1975.

[80] X. Xi, L. Zhao, Z. Wang, H. Berger, L. Forró, J. Shan, and K. Mak. Strongly enhanced charge-density-wave order in monolayer $NbSe_2$. *Nature Nanotechnology*, 10(9):765, 2015.

[81] M. Johannes and I. Mazin. Fermi surface nesting and the origin of charge density waves in metals. *Physical Review B*, 77(16):165135, 2008.

[82] M. Leroux, M. Le Tacon, M. Calandra, L. Cario, M. Measson, P. Diener, E. Borrissenko, A. Bosak, and P. Rodiere. Anharmonic suppression of charge density waves in 2H-$NbS_2$. *Physical Review B*, 86(15):155125, 2012.

[83] Origin of superconductivity and latent charge density wave in $NbS_2$, author=Heil, C. and Poncé, S. and Lambert, H. and Schlipf, M. and Margine, E. and Giustino, F., journal=Physical Review Letters, volume=119, number=8, pages=087003, year=2017, publisher=APS.

[84] B. Radisavljevic and A. Kis. Mobility engineering and a metal–insulator transition in monolayer $MoS_2$. *Nature Materials*, 12(9):815, 2013.

[85] S. Zhao, K. Wang, X. Zou, L. Gan, H. Du, C. Xu, F. Kang, W. Duan, and J. Li. Group VB transition metal dichalcogenides for oxygen reduction reaction and strain-enhanced activity governed by p-orbital electrons of chalcogen. *Nano Research*, 12(4):925–930, 2019.

[86] P. Curie and C. Chéneveau. Sur un appareil pour la détermination des constantes magnétiques. *J. Phys. Theor. Appl.*, 2(1):796–802, 1903.

[87] P. Curie. *Propriétés magnétiques des corps a diverses températures*. Number 4. Gauthier-Villars et fils, 1895.

[88] P. Weiss and G. Foex. *Le magnétisme*. Number 71. A. Colin, 1926.

[89] P. Anderson. Antiferromagnetism. theory of superexchange interaction. *Physical Review*, 79(2):350, 1950.

[90] J. Goodenough. Goodenough-Kanamori rule. *Scholarpedia*, 3(10):7382, 2008.

[91] J. Nogués and I. Schuller. Exchange bias. *Journal of Magnetism and Magnetic Materials*, 192(2):203–232, 1999.

[92] S. Kennedy and T. Hicks. The magnetic structure of $\gamma$-iron-manganese. *Journal of Physics F: Metal Physics*, 17(7):1599, 1987.

[93] A. Kohn, A. Kovács, R. Fan, G. McIntyre, R. Ward, and J. Goff. The antiferromagnetic structures of $IrMn_3$ and their influence on exchange-bias. *Scientific Reports*, 3:2412, 2013.

[94] W. Zhang, W. Han, S. Yang, Y. Sun, Y. Zhang, B. Yan, and S. Parkin. Giant facet-dependent spin-orbit torque and spin hall conductivity in the triangular antiferromagnet $IrMn_3$. *Science Advances*, 2(9):e1600759, 2016.

[95] R. Acharyya, H. Nguyen, W. Pratt, and J. Bass. Spin-flipping associated with the antiferromagnet IrMn. *IEEE Transactions on Magnetics*, 46(6):1454–1456, 2010.

[96] Z. Wei, A. Sharma, A. Nunez, P. Haney, R. Duine, J. Bass, A. MacDonald, and M. Tsoi. Changing exchange bias in spin valves with an electric current. *Physical Review Letters*, 98(11):116603, 2007.

[97] L. Frangou, S. Oyarzun, S. Auffret, L. Vila, S. Gambarelli, and V. Baltz. Enhanced spin pumping efficiency in antiferromagnetic IrMn thin films around the magnetic phase transition. *Physical Review Letters*, 116(7):077203, 2016.

[98] X. Marti, I. Fina, C. Frontera, J. Liu, P. Wadley, Q. He, R. Paull, J. Clarkson, J. Kudrnovskỳ, I. Turek, et al. Room-temperature antiferromagnetic memory resistor. *Nature Materials*, 13(4):367, 2014.

[99] D. Kriegner, K. Vỳbornỳ, K. Olejník, H. Reichlová, V. Novák, X. Marti, J. Gazquez, V. Saidl, P. Němec, V. Volobuev, et al. Multiple-stable anisotropic magnetoresistance memory in antiferromagnetic MnTe. *Nature Communications*, 7:11623, 2016.

[100] D. Kriegner, H. Reichlova, J. Grenzer, W. Schmidt, E. Ressouche, J. Godinho, T. Wagner, S. Martin, A. Shick, V. Volobuev, et al. Magnetic anisotropy in antiferromagnetic hexagonal MnTe. *Physical Review B*, 96(21):214418, 2017.

[101] J. Daughton. Magnetoresistive memory technology. *Thin Solid Films*, 216(1):162–168, 1992.

[102] A. Shick, S. Khmelevskyi, O. Mryasov, J. Wunderlich, and T. Jungwirth. Spin-orbit coupling induced anisotropy effects in bimetallic antiferromagnets: A route towards antiferromagnetic spintronics. *Physical Review B*, 81(21):212409, 2010.

[103] Y. Wang, C. Song, B. Cui, G. Wang, F. Zeng, and F. Pan. Room-temperature perpendicular exchange coupling and tunneling anisotropic magnetoresistance in an antiferromagnet-based tunnel junction. *Physical Review Letters*, 109(13):137201, 2012.

[104] D. Petti, E. Albisetti, H. Reichlová, J. Gazquez, M. Varela, M. Molina-Ruiz, A. Lopeandía, K. Olejník, V. Novák, I. Fina, et al. Storing magnetic information in IrMn/MgO/Ta tunnel junctions via field-cooling. *Applied Physics Letters*, 102(19):192404, 2013.

[105] T. Moriyama, N. Matsuzaki, K. Kim, I. Suzuki, T. Taniyama, and T. Ono. Sequential write-read operations in FeRh antiferromagnetic memory. *Applied Physics Letters*, 107(12):122403, 2015.

[106] K. Olejník, V. Schuler, X. Martí, V. Novák, Z. Kašpar, P. Wadley, R. Campion, K. Edmonds, B. Gallagher, J. Garcés, et al. Antiferromagnetic CuMnAs multilevel memory cell with microelectronic compatibility. *Nature Communications*, 8:15434, 2017.

[107] K. Garello, C. Avci, I. Miron, M. Baumgartner, A. Ghosh, S. Auffret, O. Boulle, G. Gaudin, and P. Gambardella. Ultrafast magnetization switching by spin-orbit torques. *Applied Physics Letters*, 105(21):212402, 2014.

[108] J. Chadwick. The existence of a neutron. *Proceedings of the Royal Society of London. Series A, Containing Papers of a Mathematical and Physical Character*, 136(830):692–708, 1932.

[109] J Trusler. Maxwell-boltzmann distribution. http://www.thermopedia.com/content/942/. Accessed: 2019-08-31.

[110] J. Cockcroft. Properties of the neutron. http://pd.chem.ucl.ac.uk/pdnn/inst3/neutrons.htm note = Accessed: 2019-08-31.

[111] J. Copley. Dynamics and neutron scattering. https://www.ncnr.nist.gov/summerschool/ss07/SS07Intro_talk.pdf. Accessed: 2019-08-31.

[112] R. Nave. Uranium-235 fission. http://hyperphysics.phy-astr.gsu.edu/hbase/NucEne/U235chn.html. Accessed: 2019-07-19.

[113] J. Rush and R. Cappeletti. The NIST Center for Neutron Research: Over 40 years serving NIST/NBS and the nation. *NIST Special Publication*.

[114] History of the high flux isotope reactor. https://neutrons.ornl.gov/hfir/history. Accessed: 2019-07-19.

[115] C. Brown. Bt-1 high resolution powder diffractometer instrument response function. https://ncnr.nist.gov/instruments/bt1/bt1_for_xtal.html. Accessed: 2019-08-31.

[116] C. Farrow, P. Juhás, J. Liu, D. Bryndin, E. Bozin, J. Bloch, T. Proffen, and S. Billinge. Pdfgui user guide, 2009.

[117] T. Egami and S. Billinge. *Underneath the Bragg peaks: structural analysis of complex materials*. Elsevier, 2003.

[118] B. Warren. Diffraction by imperfect crystals. *X-ray Diffraction*, 251, 1969.

[119] P. Canfield. Solution growth of intermetallic single crystals: A beginner's guide. In *Properties and Applications of Complex Intermetallics*, pages 93–111. World Scientific, 2010.

[120] J. Cui, J. Choi, G. Li, E. Polikarpov, J. Darsell, N. Overman, M. Olszta, D. Schreiber, M. Bowden, T. Droubay, et al. Thermal stability of MnBi magnetic materials. *Journal of Physics: Condensed Matter*, 26(6):064212, 2014.

[121] F. Di Salvo Jr, D. Moncton, and J. Waszczak. Electronic properties and superlattice formation in the semimetal $TiSe_2$. *Physical Review B*, 14(10):4321, 1976.

[122] H. Cercellier, C. Monney, F. Clerc, C. Battaglia, L. Despont, M. Garnier, H. Beck, P. Aebi, L. Patthey, H. Berger, et al. Evidence for an excitonic insulator phase in 1T-$TiSe_2$. *Physical Review Letters*, 99(14):146403, 2007.

[123] D. De Boer, C. Van Bruggen, G. Bus, R. Coehoorn, C. Haas, G. Sawatzky, H. Myron, D. Norman, and H. Padmore. Titanium ditelluride: Band structure, photoemission, and electrical and magnetic properties. *Physical Review B*, 29(12):6797, 1984.

[124] Y. Arnaud and M. Chevreton. Etude comparative des composés $TiX_2$ (X= S, Se, Te). structures de $TiTe_2$ et TiSeTe. *Journal of Solid State Chemistry*, 39(2):230–239, 1981.

[125] K. Rossnagel, L. Kipp, and M. Skibowski. Charge-density-wave phase transition in 1T-$TiSe_2$: Excitonic insulator versus band-type Jahn-Teller mechanism. *Physical Review B*, 65(23):235101, 2002.

[126] D. Jérome, T. Rice, and W. Kohn. Excitonic insulator. *Physical Review*, 158(2):462, 1967.

[127] M. Porer, U. Leierseder, J. Ménard, H. Dachraoui, L. Mouchliadis, I. Perakis, U. Heinzmann, J. Demsar, K. Rossnagel, and R. Huber. Non-thermal separation of electronic and structural orders in a persisting charge density wave. *Nature Materials*, 13(9):857, 2014.

[128] H. Hughes. Structural distortion in $TiSe_2$ and related materials-a possible Jahn-Teller effect? *Journal of Physics C: Solid State Physics*, 10(11):L319, 1977.

[129] M. Whangbo and E. Canadell. Analogies between the concepts of molecular chemistry and solid-state physics concerning structural instabilities. electronic origin of the structural modulations in layered transition metal dichalcogenides. *Journal of the American Chemical Society*, 114(24):9587–9600, 1992.

[130] D. Greenaway and R. Nitsche. Preparation and optical properties of group IV–VI2 chalcogenides having the $CdI_2$ structure. *Journal of Physics and Chemistry of Solids*, 26(9):1445–1458, 1965.

[131] A. Wegner, D. Louca, and J. Yang. Local trigonal modes and the suppression of the charge density wave in $TiSe_{2-x}Te_2$. *Physical Review B*, 99(20):205110, 2019.

[132] S. Kobayashi, H. Ueda, D. Nishio-Hamane, C. Michioka, and K. Yoshimura. Successive phase transitions driven by orbital ordering and electron transfer in quasi-two-dimensional $CrSe_2$ with a triangular lattice. *Physical Review B*, 89:054413, Feb 2014.

[133] F. Schucht, A. Dascoulidou, R. Müller, W. Jung, H. Schuster, W. Bronger, and P. Müller. Die magnetischen eigenschaften der alkalimetall-manganpnictide KMnP, RbMnP, CsMnP, RbMnAs, KMnSb, KMnBi, RbMnBi und CsMnBi–neutronenbeugungsuntersuchungen und suszeptibilitätsmessungen. *Zeitschrift für Anorganische und Allgemeine Chemie*, 625(1):31–36, 1999.

[134] W. Bronger, P. Müller, R. Höppner, and H. Schuster. Zur charakterisierung der magnetischen eigenschaften von NaMnP, NaMnAs, NaMnSb, NaMnBi, LiMnAs und KMnAs über neutronenbeugungsexperimente. *Zeitschrift für Anorganische und Allgemeine Chemie*, 539(8):175–182, 1986.

[135] V. Novák, M. Cukr, Z. Šobáň, T. Jungwirth, X. Martí, V. Holỳ, P. Horodyská, and P. Němec. Molecular beam epitaxy of LiMnAs. *Journal of Crystal Growth*, 323(1):348–350, 2011.

[136] A. Wijnheijmer, X. Martí, V. Holỳ, M. Cukr, V. Novák, T. Jungwirth, and P. Koenraad. Scanning tunneling microscopy reveals LiMnAs is a room temperature anti-ferromagnetic semiconductor. *Applied Physics Letters*, 100(11):112107, 2012.

[137] A. Beleanu, J. Kiss, G. Kreiner, C. Köhler, L. Müchler, W. Schnelle, U. Burkhardt, S. Chadov, S. Medvediev, D. Ebke, et al. Large resistivity change and phase transition in the antiferromagnetic semiconductors LiMnAs and LaOMnAs. *Physical Review B*, 88(18):184429, 2013.

[138] T. Jungwirth, V. Novak, X. Marti, M. Cukr, F. Maca, A. Shick, J. Masek, P. Horodyska, P. Nemec, V. Holy, et al. Antiferromagnetic I-Mn-V semiconductors. *arXiv preprint arXiv:1007.0177*, 2010.

[139] P. Wadley, V. Novák, R. Campion, C. Rinaldi, X. Martí, H. Reichlová, J. Železnỳ, J. Gazquez, M. Roldan, M. Varela, et al. Tetragonal phase of epitaxial room-temperature antiferromagnet CuMnAs. *Nature communications*, 4:2322, 2013.

[140] M. Stamenova, R. Mohebbi, J. Seyed-Yazdi, I. Rungger, and S. Sanvito. First-principles spin-transfer torque in CuMnAs| GaP| CuMnAs junctions. *Physical Review B*, 95(6):060403, 2017.

[141] T. Jungwirth, X. Marti, P. Wadley, and J. Wunderlich. Antiferromagnetic spintronics. *Nature Nanotechnology*, 11(3):231, 2016.

[142] F. Máca, J. Mašek, O. Stelmakhovych, X. Martí, H. Reichlová, K. Uhlířová, P. Beran, P. Wadley, V. Novák, and T. Jungwirth. Room-temperature antiferromagnetism in CuMnAs. *Journal of Magnetism and Magnetic Materials*, 324(8):1606–1612, 2012.

[143] C. Chappert, A. Fert, and F. Van Dau. The emergence of spin electronics in data storage. In *Nanoscience And Technology: A Collection of Reviews from Nature Journals*, pages 147–157. World Scientific, 2010.

[144] Z. Deng, C. Jin, Q. Liu, X. Wang, J. Zhu, S. Feng, L. Chen, R. Yu, C. Arguello, T. Goko, et al. Li(zn, mn)as as a new generation ferromagnet based on a I-II-V semiconductor. *Nature Communications*, 2:422, 2011.

[145] K. Zhao, B. Chen, G. Zhao, Z. Yuan, Q. Liu, Z. Deng, J. Zhu, and C. Jin. Ferromagnetism at 230 K in $(Ba_{0.7}K_{0.3})(Zn_{0.85}Mn_{0.15})_2As_2$ diluted magnetic semiconductor. *Chinese Science Bulletin*, 59(21):2524–2527, 2014.

[146] K. Zhao, Z. Deng, X. Wang, W. Han, J. Zhu, X. Li, Q. Liu, R. Yu, T. Goko, B. Frandsen, et al. New diluted ferromagnetic semiconductor with Curie temperature up to 180 K and isostructural to the âĂŸ122âĂŹiron-based superconductors. *Nature Communications*, 4:1442, 2013.

[147] Single crystal growth and spin polarization measurements of diluted magnetic semiconductor $(BaK)(ZnMn)_2As_2$, author=Zhao, G. and Lin, C. and Deng, Z. and Gu, G. and Yu, S. and Wang, X. and Gong, Z. and Uemera, Y. and Li, Y. and Jin, C., journal=Scientific Reports, volume=7, number=1, pages=14473, year=2017, publisher=Nature Publishing Group.

[148] T. Jungwirth, V. Novák, X. Martí, M. Cukr, F. Máca, A. Shick, J. Mašek, P. Horodyská, P. Němec, V. Holỳ, et al. Demonstration of molecular beam epitaxy and a semiconducting band structure for I-Mn-V compounds. *Physical Review B*, 83(3):035321, 2011.

[149] R. Cava. A useful pyramid scheme. *Physics*, 4:7, 2011.

[150] J. Yang, A. Wegner, C. Brown, and D. Louca. Defect-driven extreme magnetoresistance in an I-Mn-V semiconductor. *Applied Physics Letters*, 113(12):122105, 2018.

[151] J. Ziman. *Principles of the Theory of Solids*. Cambridge university press, 1979.

[152] H. Yamada and S. Takada. Magnetoresistance of antiferromagnetic metals due to s-d interaction. *Journal of the Physical Society of Japan*, 34(1):51–57, 1973.

[153] S. Alexander, J. Helman, and I. Balberg. Critical behavior of the electrical resistivity in magnetic systems. *Physical Review B*, 13(1):304, 1976.

[154] C. Jooss, L. Wu, T. Beetz, R. Klie, M. Beleggia, M. Schofield, S. Schramm, J. Hoffmann, and Y. Zhu. Polaron melting and ordering as key mechanisms for colossal resistance effects in manganites. *Proceedings of the National Academy of Sciences*, 104(34):13597–13602, 2007.